Higgs Spin Determination and Unitarity of Vector-boson Scattering at the LHC

Zur Erlangung des akademischen Grades eines

DOKTORS DER NATURWISSENSCHAFTEN

von der Fakultät für Physik des

Karlsruher Institutes für Technologie (KIT)

genehmigte

DISSERTATION

von

Dipl.-Phys. Jessica Frank

aus Stuttgart

Tag der mündlichen Prüfung: 24.01.2014

Referent:	Prof. Dr. Dieter Zeppenfeld
Korreferentin:	Prof. Dr. Margarete Mühlleitner

Abstract

After the discovery of a new particle at the Large Hadron Collider (LHC), it is crucial to definitely verify or disprove whether this new $125 - 126$ GeV resonance is the Higgs boson of the Standard Model (SM). Thus, its features, including its spin, have to be determined. In order to distinguish the two most likely spin hypotheses, spin-0 or spin-2, the phenomenology of light spin-2 resonances produced in different gluon-fusion and vector-boson-fusion processes at the LHC is studied. Starting from an effective model for the interaction of a spin-2 particle with SM gauge bosons, cross sections and differential distributions are calculated within the Monte Carlo program VBFNLO. Whereas with specific model parameters, such a spin-2 resonance can mimic rates and transverse-momentum distributions of a SM Higgs boson in the main decay channels $\gamma\gamma$, WW and ZZ, several distributions allow to separate spin-2 from spin-0, almost independently of model parameters. Since the SM Higgs boson ensures the unitarity of the S-matrix in vector-boson scattering, another topic of this thesis is to investigate if the capability of unitarizing vector-boson scattering is a unique feature of the spin-0 Higgs boson or if particles with a different spin, i.e. spin-1 or spin-2, are able to perform the same task. Furthermore, the characteristics of heavy spin-2 resonances in vector-boson-fusion processes are analyzed at NLO QCD accuracy in order to facilitate the spin determination of heavy particles that might be detected at the LHC.

Zusammenfassung

Nachdem am Large Hadron Collider (LHC) ein neues Teilchen mit einer Masse von $125-126$ GeV entdeckt wurde, ist es äußerst wichtig zu verifizieren oder widerlegen, dass es sich dabei um das Higgs Boson des Standardmodells (SM) handelt. Deshalb müssen seine Eigenschaften, einschließlich seines Spins, bestimmt werden. Um die beiden wahrscheinlichsten Hypothesen Spin-0 und Spin-2 zu unterscheiden, wird die Phänomenologie leichter Spin-2 Resonanzen erforscht, die in verschiedenen Gluon-Fusions- und Vektorboson-Fusionsprozessen erzeugt werden. Ausgehend von einem effektiven Modell für die Wechselwirkung eines Spin-2 Teilchens mit Eichbosonen des Standardmodells werden mithilfe des Monte Carlo Programms VBFNLO Wirkungsquerschnitte und differentielle Verteilungen berechnet. Während Spin-2 Resonanzen mit bestimmten Modellparametern Raten und Transversalimpulsverteilungen des SM Higgs Bosons in den wichtigsten Zerfallskanälen $\gamma\gamma$, WW und ZZ nachahmen können, erlauben verschiedene Verteilungen eine nahezu parameterunabhängige Unterscheidung zwischen Spin-2 und Spin-0. Da das SM Higgs Boson außerdem die Unitarität der S-Matrix in Vektorboson-Streuung sicherstellt, ist es ein weiteres Thema dieser Arbeit, herauszufinden, ob dies eine einzigartige Eigenschaft des Spin-0 Higgs Bosons ist, oder ob Teilchen mit Spin-1 oder Spin-2 dieselbe Aufgabe übernehmen können. Des Weiteren werden die Eigenschaften schwerer Spin-2 Resonanzen in Vektorboson-Fusionsprozessen in nächst-führender Ordnung QCD untersucht, um die Spinbestimmung möglicher neuer Teilchen am LHC zu erleichtern.

Contents

1 Introduction

Discovering the fundamental components of the universe and exploring their interactions is one of the major scientific impulses of mankind. Over centuries, innumerable people have contributed to our constantly increasing understanding of this topic. Initially reserved to philosophers, it was taken over first by chemists and eventually by physicists. Nowadays, our knowledge about the constituents of matter and the electromagnetic, weak and strong interaction between them is summarized in the Standard Model of Elementary Particle Physics (SM), which provides a uniform theoretical description in terms of relativistic quantum field theories. A plethora of its predictions have been confirmed experimentally, some of them with incredible precision. Remarkably, the anomalous magnetic moment of the electron, which is experimentally known up to more than ten digits [1], is the most accurately verified theoretical prediction in the history of physics. Crucial contributions to such precision measurements and to the discoveries of the various particles predicted by the Standard Model stem from particle accelerators, such as the Large Electron Positron collider (LEP) at CERN and the proton-antiproton collider Tevatron at Fermilab. At present, the most powerful accelerator is the CERN Large Hadron Collider (LHC), whose first proton-proton collisions took place in 2009.

Before the era of the LHC, the only constituent of the Standard Model that had not been discovered was the Higgs boson. This scalar particle originates from the Higgs mechanism, which was postulated in order to account for the masses of elementary particles. On July 4, 2012, the collaborations of the LHC experiments ATLAS and CMS both announced the observation of a new particle [2] at a mass of $125 - 126$ GeV, which was conjectured to be a Higgs boson. Since then, many experimental studies confirmed that the data obtained for this new resonance are compatible with being the Higgs boson of the Standard Model [3–12]. On these grounds, Peter Higgs and François Englert were awarded the 2013 Nobel prize in physics for their theoretical development of the Higgs mechanism [13].

The Higgs mechanism of the Standard Model provides a simple and elegant explanation for the generation of particle masses, while respecting fundamental properties of the theory, i.e. unitarity and renormalizability. However, there exist many alternative approaches. Most of them are motivated by insufficiencies of the SM, which neither incorporates gravity, nor accounts for the experimental evidence of dark matter and dark energy in the universe. Furthermore, the SM cannot explain why there is more matter than antimatter and does not predict the values of many of the couplings and the masses of the particles. In order to address at least some of these issues, theories beyond the Standard

Model (BSM) often exhibit a modified particle content, which can comprise several Higgs bosons, no Higgs boson or a Higgs boson with modified properties. Furthermore, different kinds of other new particles are postulated by various models. In some scenarios, BSM particles can closely resemble the Higgs boson of the Standard Model. Therefore, it is crucial to determine all the characteristic features of the newly discovered resonance in order to definitely verify or disprove whether it is the SM Higgs boson. These features, including its couplings to other SM particles [14], its self-couplings [15], its CP quantum number and its spin [16–27], are currently the subject of active research.

The Higgs resonance can be detected and identified in several channels at the LHC. It is mainly produced in gluon fusion or vector-boson fusion (VBF). The most important decay modes for its observation and analysis include $H \to \gamma\gamma$, $H \to W^+W^- \to 2l2\nu$ and $H \to ZZ \to 4l$. Observing these decays immediately excludes a particle with half-integer spin. Moreover, the detection of the resonance in the diphoton decay mode excludes a spin-1 particle due to the Landau–Yang theorem [28], leaving spin-2 as an alternative hypothesis to the spin-0 of the SM Higgs boson. Since the distinction of a spin-0 and a spin-2 resonance is an important element of the identification of the newly discovered particle, this distinction is a key task of this thesis. To this end, spin-2 resonances at the LHC are studied within the framework of an effective Lagrangian model describing interactions of a spin-2 electroweak singlet or triplet state with SM gauge bosons. Calculations of cross sections and differential distributions are performed by means of the Monte Carlo program VBFNLO [29], which is then used to search for characteristics distinguishing between the two spin choices spin-0 and spin-2 in the main detection modes. Furthermore, the dependence of these characteristics on model parameters and NLO QCD corrections is analyzed.

To ascertain the mechanism of generating particle masses, it is not only important to determine the features of the new $125 - 126$ GeV resonance, but also to search for other signs of physics beyond the Standard Model. The high energies accessible with the LHC allow for the search of new, heavy particles in the few TeV range, which might e.g. be produced in vector-boson fusion. For such resonances, a spin determination would also be needed. Whereas heavy spin-1 resonances have already been studied within VBFNLO [30], the phenomenology of heavy spin-2 resonances is investigated at NLO QCD accuracy within the present work, where different processes with two VBF jets and four leptons in the final state are considered. Resulting from spin-2 resonances that decay into two electroweak bosons or from SM electroweak continuum contributions, these are $e^+ e^- \mu^+\mu^- jj$,

$e^+ e^- \nu_\mu \overline{\nu}_\mu jj$, $e^+ \nu_e \mu^- \overline{\nu}_\mu jj$, $e^+ \nu_e \mu^+ \mu^- jj$ and $e^- \overline{\nu}_e \mu^+ \mu^- jj$ production. Of these, the first one will be studied in most detail, since a final state without neutrinos allows for a full reconstruction of a resonance.

The Higgs mechanism of the Standard Model does not only account for particle masses, but also ensures the unitarity of the S-matrix in vector-boson scattering via exchange of its scalar boson [31]. Since the S-matrix is related to physical cross sections, any BSM scenario must also imply this conservation of probability. Therefore, another topic of this thesis is to investigate if the capability of unitarizing vector-boson scattering is a unique feature of the spin-0 Higgs boson or if particles with a different spin, i.e. spin-1 or spin-2, are able to perform the same task. To this end, unitarity is analyzed by studying the high-energy behavior of partial waves in a combination of all uncharged channels of weak bosons in the initial and final state, including both longitudinal and transverse modes.

This thesis is organized as follows: After introducing relevant theoretical foundations in Section 2, results of the analyses are presented in Section 3 and Section 4, including descriptions of the corresponding models and elements of calculations and implementations. Section 3 is mainly devoted to the spin determination of the newly discovered resonance in different production and decay channels at the LHC, but also includes the investigation of heavy spin-2 resonances in vector-boson fusion. In Section 4, the unitarity properties of vector-boson scattering with resonances of different spin are analyzed. Finally, the most important results of the present work are summarized and discussed in Section 5.

2 Theoretical Foundations

This section provides an overview over selected topics of the foundations that are most important for the present work. As a starting point, the Standard Model, being the underlying basic theory of Elementary Particle Physics, is introduced. The central question of this thesis is whether the new resonance discovered at the LHC is the SM Higgs boson or another particle corresponding to a theory beyond the Standard Model. Therefore, the SM Higgs mechanism as well as alternative ideas of electroweak symmetry breaking (EWSB) are discussed. Afterwards, the properties and relevant production and decay channels of the Higgs boson are summarized in order to reveal its characteristics at the LHC. Since the present work provides theoretical predictions for the phenomenology of Higgs and other resonances at a hadron collider, the relevant techniques of such predictions are presented, including general features of hadron collisions, Monte Carlo generators and next-to-leading order calculations.

2.1 The Standard Model of Elementary Particle Physics

The Standard Model of Elementary Particle Physics provides a uniform description of the constituents of matter and their fundamental forces, which are the electromagnetic, weak and strong interaction. During the last decades, a huge variety of its predictions was verified experimentally up to an enormous precision. Its foundations are described in many text books as well as summarized in various reviews, e.g. Refs. [32], [33] and [34]. The SM is a relativistic quantum field theory based on the principle of local gauge invariance, with the gauge group $SU(3)_C \times SU(2)_L \times U(1)_Y$.

$SU(3)_C$ is the gauge group of quantum chromodynamics (QCD), which describes the strong interaction. Since a gauge group $SU(N)$ has $N^2 - 1$ generators, there are eight $SU(3)$ generators. They are connected to eight massless gluons, which are the gauge bosons mediating the strong interaction between colored particles. Color is the quantum number of QCD, carried by quarks (and antiquarks) and the gluons themselves. $SU(2)_L \times U(1)_Y$ combines the electromagnetic and weak interactions between quarks and leptons (and their antiparticles), into a uniform electroweak theory. The force carriers, again resulting from the generators of the gauge group, are the three $SU(2)_L$ gauge bosons W^1, W^2, W^3 and the $U(1)_Y$ gauge boson B.

The constituents of matter comprise three generations of left-handed and right-handed quarks and leptons, which are the projections $f_{L,R} = \frac{1}{2}(1 \mp \gamma_5)\, f$ of the fermion fields f. The left-handed fermions form doublets under $SU(2)$, whereas the right-handed ones are

$SU(2)$ singlets:

	Quarks (Q)			Leptons (L)		
Left-handed	$\begin{pmatrix} u \\ d \end{pmatrix}_L$	$\begin{pmatrix} c \\ s \end{pmatrix}_L$	$\begin{pmatrix} t \\ b \end{pmatrix}_L$	$\begin{pmatrix} \nu_e \\ e^- \end{pmatrix}_L$	$\begin{pmatrix} \nu_\mu \\ \mu^- \end{pmatrix}_L$	$\begin{pmatrix} \nu_\tau \\ \tau^- \end{pmatrix}_L$
Right-handed	u_R, d_R	c_R, s_R	t_R, b_R	e^-_R	μ^-_R	τ^-_R

Since the neutrinos ν_e, ν_μ and ν_τ are assumed to be massless, there are no right-handed neutrinos in the SM. However, they can be added rather straightforwardly to account for experimentally observed small non-zero neutrino masses.
Interactions between gauge bosons and fermions can be derived from the gauge-invariant SM Lagrangian, which is, except for the Higgs and Yukawa part discussed later, given by

$$\mathcal{L}_{\text{SM}} = -\frac{1}{4}G^a_{\mu\nu}G^{\mu\nu}_a - \frac{1}{4}W^a_{\mu\nu}W^{\mu\nu}_a - \frac{1}{4}B_{\mu\nu}B^{\mu\nu} + \sum_j (\bar{Q}_j\, iD_\mu\gamma^\mu Q_j + \bar{L}_j\, iD_\mu\gamma^\mu L_j). \quad (2.1)$$

The sum over j comprises the left- and right-handed quarks and leptons given above. Summations over upper and lower equal indices are implicitly assumed throughout this work, with Greek letters indicating Lorentz indices.
The first part of this Lagrangian describes the spin-1 gauge bosons. $G^a_{\mu\nu}$, $W^a_{\mu\nu}$ and $B_{\mu\nu}$ are the corresponding field strength tensors,

$$\begin{aligned} G^a_{\mu\nu} &= \partial_\mu G^a_\nu - \partial_\nu G^a_\mu + g_s f^{abc} G_{b,\mu} G_{c,\nu} \\ W^a_{\mu\nu} &= \partial_\mu W^a_\nu - \partial_\nu W^a_\mu + g\epsilon^{abc} W_{b,\mu} W_{c,\nu} \\ B_{\mu\nu} &= \partial_\mu B_\nu - \partial_\nu B_\mu, \end{aligned} \quad (2.2)$$

with g_s and g being the couplings of $SU(3)_C$ and $SU(2)_L$. The $U(1)_Y$ coupling is denoted as g'. The structure constants f^{abc} and ϵ^{abc} determine the commutation relations between the generators of the $SU(3)_C$ and $SU(2)_L$ group. This non-abelian structure gives rise to triple and quartic gauge-boson self-interactions.
The second part of the Lagrangian (2.1) describes the fermions and their couplings to gauge bosons, which are minimal couplings resulting from the covariant derivative

$$D_\mu = \partial_\mu - ig_s T^a G_{a,\mu} - ig\frac{\sigma^a}{2}W_{a,\mu} - ig' Y B_\mu, \quad (2.3)$$

with T^a, $\frac{\sigma^a}{2}$ and Y denoting the generators of the groups $SU(3)_C$, $SU(2)_L$ and $U(1)_Y$.

Within this framework, the SM fields carry the quantum numbers of the gauge groups, which are color, weak isospin I and hypercharge Y. Furthermore, electric charge emerges naturally as a combination of hypercharge and the third component of the isospin, I_3, according to the Gell–Mann–Nishijima relation $Q = I_3 + \frac{Y}{2}$. Accounting for masses, however, is more intricate. While the mass of macroscopic objects mainly originates from QCD binding energy within protons and neutrons, which consist of quarks exchanging gluons, the mass of elementary particles should be described by the SM Lagrangian. A naive extension of Eq. (2.1) by mass terms like $\frac{1}{2}m_w^2 W_\mu^a W_a^\mu$ explicitly violates $SU(2)_L \times U(1)_Y$ gauge invariance. Yet we know from experiments that the force carriers of the weak interactions as well as fermions are massive, while photons and gluons are massless. Thus, a method of breaking the electroweak $SU(2)_L \times U(1)_Y$ symmetry spontaneously must be incorporated in order to generate the masses of elementary particles. In the SM, the chosen method is the Higgs mechanism, which is outlined in the following section.

2.2 Electroweak symmetry breaking and the Higgs mechanism

2.2.1 The SM Higgs mechanism

In the Higgs mechanism of the SM, the electroweak $SU(2)_L \times U(1)_Y$ symmetry is spontaneously broken by introducing an additional scalar field with an appropriate potential. In order to obtain three massive and one massless electroweak gauge boson, the latter one being the photon, $SU(2)_L \times U(1)_Y$ must be broken to the electromagnetic group $U(1)_Q$. According to the Goldstone theorem, this leads to three massless scalar bosons, denoted as Goldstone bosons. The easiest way to obtain at least three scalar degrees of freedom is to introduce a complex scalar $SU(2)$ doublet field

$$\Phi = \begin{pmatrix} \phi^+ \\ \phi^0 \end{pmatrix} = \begin{pmatrix} \phi_1 + i\,\phi_2 \\ \phi_3 + i\,\phi_4 \end{pmatrix}, \tag{2.4}$$

which has four degrees of freedom and hypercharge $Y_\Phi = 1$. Its $SU(2)$-invariant Lagrangian, consisting of a kinetic and a potential term,

$$\mathcal{L}_{\text{Higgs}} = T - V = (D_\mu \Phi)^\dagger (D^\mu \Phi) + \mu^2 \Phi^\dagger \Phi - \lambda (\Phi^\dagger \Phi)^2 \qquad (\mu^2, \lambda > 0) \tag{2.5}$$

must be added to the Lagrangian of Eq. (2.1). For $\mu^2 < 0$, the potential V would only feature a trivial minimum at zero and the gauge bosons would remain massless. For $\mu^2 > 0$, however, the scalar field acquires a vacuum expectation value

$$\Phi_0 = \begin{pmatrix} 0 \\ \frac{v}{\sqrt{2}} \end{pmatrix}, \quad \text{with } v = \sqrt{\frac{\mu^2}{\lambda}}, \tag{2.6}$$

corresponding to a specific choice of the non-trivial minimum of the potential. v is related to the Fermi constant G_F, which is known from experiments, and can therefore be determined to be $v = (\sqrt{2}\, G_F)^{-1/2} \approx 246$ GeV. For a proper interpretation of the theory, Φ must be expanded around the vacuum state (2.6). This expansion can be written as

$$\Phi(x) = e^{\frac{i\sigma_a \theta^a(x)}{v}} \begin{pmatrix} 0 \\ \frac{1}{\sqrt{2}}\,(v + H(x)) \end{pmatrix}. \tag{2.7}$$

Thus, a new physical field H –the Higgs field– arises, whereas θ^a are the three Goldstone bosons mentioned before. By applying a gauge transformation leading to the unitarity gauge, the Goldstone bosons can be rotated away,

$$\Phi(x) \to e^{\frac{-i\sigma_a \theta^a(x)}{v}} \Phi(x) = \begin{pmatrix} 0 \\ \frac{1}{\sqrt{2}}(v + H(x)) \end{pmatrix}, \tag{2.8}$$

and become the longitudinal degrees of freedom of three gauge bosons, which thus obtain masses. When the expansion (2.8) is again inserted into the scalar Lagrangian (2.5), the original $SU(2)_L \times U(1)_Y$ symmetry is not apparent anymore and is said to be spontaneously broken. However, a $U(1)_Q$ symmetry remains, ensured by a vacuum expectation value in the neutral component of the scalar doublet and not in the charged one. Therefore, the photon as unbroken $U(1)$ generator remains massless. In contrast, the weak gauge bosons acquire masses from the kinetic term of Eq. (2.5):

$$(D_\mu \Phi)^\dagger (D^\mu \Phi) = \frac{1}{2}(\partial_\mu H)(\partial^\mu H) + \left(1 + \frac{H}{v}\right)^2 \left[\left(\frac{gv}{2}\right)^2 W_\mu^+ W^{\mu -} + \frac{1}{2}\,\frac{(g^2 + g'^2)v^2}{4} Z_\mu Z^\mu\right]. \tag{2.9}$$

Here, new linear combinations of the gauge bosons W^1, W^2, W^3 and B are introduced,

$$\begin{aligned} W_\mu^\pm &= \frac{1}{\sqrt{2}}(W_\mu^1 \mp i W_\mu^2), \\ Z_\mu &= \frac{g\, W_\mu^3 - g' B_\mu}{\sqrt{g^2 + g'^2}} = W_\mu^3 \cos\theta_w - B_\mu \sin\theta_w, \\ A_\mu &= \frac{g'\, W_\mu^3 + g B_\mu}{\sqrt{g^2 + g'^2}} = W_\mu^3 \sin\theta_w + B_\mu \cos\theta_w, \end{aligned} \tag{2.10}$$

with θ_w being the weak mixing angle. From Eq. (2.9), the masses of the charged and neutral weak bosons $W^\pm$ and Z can be read off as $m_W = \frac{1}{2} g v$ and $m_Z = \frac{1}{2}\sqrt{g^2 + g'^2}\, v$, while there is no mass term for the photon field A. The term proportional to $\frac{2H}{v}$ in Eq. (2.9) leads to couplings of a Higgs boson and two W or Z bosons. Furthermore, couplings of two Higgs bosons and two weak bosons arise from the $\frac{H^2}{v^2}$ term. Remarkably, both kinds of couplings are proportional to the squared masses of the weak bosons.
When the expansion (2.8) is inserted into the Higgs potential V of Eq. (2.5), it follows that the Higgs boson itself acquires a mass, which is proportional to the free parameter μ and therefore not predicted by the theory. The potential also yields triple and quartic Higgs-boson self-interactions, which are determined by v and the Higgs mass.

The Higgs mechanism also generates fermion masses via a further term added to the Lagrangian,

$$\mathcal{L}_{\text{Yukawa}} = \sum_{\text{generations}\, j} -(\lambda_{l,j}\, \bar{L}_j\, \Phi\, l_{R,j} + \lambda_{d,j}\, \bar{Q}_j\, \Phi\, q_{d_R,\,j} + \lambda_{u,j}\, \bar{Q}_j\, \widetilde{\Phi}\, q_{u_R,\,j}) + h.c. \tag{2.11}$$

Here, L (Q) denote the left-handed leptons (quarks), l_R are the right-handed leptons, q_{d_R} (q_{u_R}) are the right-handed down-type (up-type) quarks and $h.c.$ means hermitian conjugate. $\widetilde{\Phi}$ is the charge conjugated field

$$\widetilde{\Phi} = i\sigma_2 \Phi^* = \begin{pmatrix} 0 & 1 \\ -1 & 0 \end{pmatrix} \begin{pmatrix} (\phi^+)^* \\ (\phi^0)^* \end{pmatrix} = \begin{pmatrix} (\phi^0)^* \\ -\phi^- \end{pmatrix}. \tag{2.12}$$

As before, inserting the expansion (2.8) into the Lagrangian (2.11) leads to masses, which in case of fermions are proportional to the Yukawa couplings λ, and to Higgs boson couplings to two fermions proportional to the fermion masses.
It should be noted that the mass eigenstates of the quarks do not coincide with their

eigenstates of the weak interaction. The transformation between them is given by the Cabibbo-Kobayashi-Maskawa matrix V_{CKM}, which is unitary and deviates from the identity matrix by terms of order $\sin\theta_c \approx 0.23$, where θ_c is the Cabibbo angle.

2.2.2 Alternative ideas of electroweak symmetry breaking

Although the SM Higgs mechanism provides a simple and elegant way to break the electroweak symmetry spontaneously and to provide masses both for gauge bosons and fermions, several aspects remain unclear. For instance, there is no dynamical explanation *why* electroweak symmetry breaking occurs or *why* the vacuum expectation value is of the order of the electroweak scale. Furthermore, the Higgs mechanism does not provide further insight into the existence and hierarchy of fermion generations. Instead, the Yukawa couplings of the Higgs boson to fermions are arbitrary free parameters. Another important aspect is related to the nature of the Higgs boson as an elementary scalar particle. Its mass is unstable against loop corrections, which comprise contributions from gauge bosons, heavy quarks and the Higgs boson itself. Enormously fine-tuned cancellations between these different contributions must occur accidentally in order to have a Higgs mass of the order of the electroweak scale.
Motivated by this, theorists have developed many alternative models of electroweak symmetry breaking, which evade some of these unwanted features and sometimes even address other open questions of particle physics and cosmology, such as the incorporation of gravity, dark matter, inflation or the matter–antimatter asymmetry of the universe.
This section provides a short sketch over some alternative ideas of electroweak symmetry breaking. Nice reviews highlighting different aspects can e.g. be found in Refs. [35], [36] and [37].

- **Supersymmetry** [38]
  One way to protect the Higgs mass against quadratic divergences in higher-order corrections is to introduce a symmetry between bosonic and fermionic degrees of freedom, denoted as supersymmetry. Apart from spin-0 and spin-$\frac{1}{2}$ super-partners of SM fermions and bosons, supersymmetric theories feature an extended Higgs sector (see e.g. Ref. [36] and references therein). There must be at least two Higgs doublet fields in order to preserve supersymmetry and gauge invariance. In the minimal supersymmetric extension of the SM (MSSM), there are exactly two complex Higgs doublets [39]. Thus, the Higgs sector of the MSSM is a special case of general two Higgs doublet models. One of these doublets is giving mass to the up-type- and the other one to the down-type particles. The eight degrees of freedom result in

three Goldstone bosons (corresponding to longitudinal modes of the massive gauge bosons) and five physical Higgs bosons, which form three neutral and two charged mass eigenstates. Among the neutral ones, there are two $\mathcal{CP}$-even and one $\mathcal{CP}$-odd Higgs boson. The couplings of MSSM Higgs bosons to SM particles are modified by two mixing angles of the Higgs sector, whereas the quartic Higgs coupling is related to the squared gauge couplings. Since the MSSM cannot explain why one of its parameters, μ, is of the order of the electroweak scale, another extension was introduced, known as NMSSM [40]. There, the μ-parameter is replaced by the vacuum expectation value of an additional complex singlet Higgs field. This gives rise to two further Higgs bosons, of which one is $\mathcal{CP}$-even and the other one $\mathcal{CP}$-odd. Another attractive feature of supersymmetric theories is that they often provide a weakly interacting massive particle (WIMP) as a candidate for dark matter. Furthermore, supersymmetry allows for the unification of the strong, weak and electromagnetic couplings at a high energy scale.

- **Higgsless models with extra dimensions** [41]
  By introducing additional space dimensions of finite size, it is possible to break the electroweak symmetry via boundary conditions (BCs), without the need of the Higgs mechanism. Special cases of these BCs can be chosen for each field separately, corresponding to different physical situations. In theories with extra dimensions, additional scalars arise as extra-dimensional components of gauge fields. In higgsless models, however, they can be eliminated by choosing appropriate boundary conditions. As an example, consider a simple toy model with one flat extra-dimensional interval [42], where $SU(2)$ gauge fields decompose into infinitely many modes (like standing waves on a rope). They are denoted as Kaluza-Klein (KK) modes. By choosing Neumann BCs on both ends of the interval (corresponding to loose ends in case of a rope) for the W^3_μ field, it decomposes into a tower of neutral states, including a massless zero mode describing the photon. The additional states acquire masses which are proportional to their mode number and inversely proportional to the size of the extra dimension. For the fields W^1_μ and W^2_μ, one can choose a Neumann BC on one end of the interval and a Dirichlet BC on the other end (corresponding to a loose and a fixed end of a rope). This leads to a KK tower of charged modes, which are all massive. By this procedure, gauge bosons acquire masses and the $SU(2)$ symmetry is broken to $U(1)$. However, the resulting mass ratio of the W and Z boson differs from the one of the SM. A more realistic model incorporates a custodial $SU(2)_L \times SU(2)_R$ symmetry, which protects the W/Z mass ratio, into

a warped finite extra dimension with an Anti-de-Sitter metric. Such a metric can also account for the hierarchy problem, since lengths and energies scale with the coordinate of the extra dimension.

- **Deconstructed Higgsless models** [43]
  Deconstructed models result from five-dimensional ones by discretization of the extra dimension. Thereby, gauge fields originally defined at each point of the extra dimension become independent fields of a gauge group $U(1) \times [SU(2)]^{n+1}$ in four dimensions. This results in n additional triplets of gauge bosons, instead of infinitely many. In the limit $n \to \infty$, the five-dimensional continuum theory is recovered. Scalar fields, which are the fifth components of gauge fields in the five-dimensional model, become Goldstone bosons of a non-linear sigma model, which triggers electroweak symmetry breaking at adjacent sites, again without physical Higgs bosons.

- **HEIDI** [44] **and Unparticle physics** [45]
  As an extension to the SM, HEIDI (for "hidi(ng) in high-D(imensions)") models introduce additional scalar singlet fields. These singlets do not interact with SM particles except for the SM Higgs boson, with which they mix. There can be infinitely many such Higgs bosons, e.g. by decomposing a field in a finite extra dimension into an infinite number of modes. This leads to a continuous mass spectrum with or without additional peaks [46]. Furthermore, additional singlets can lead to invisible Higgs decays, which can dominate over the visible decays into the SM particles. In this case, the Higgs resonance would be broad and difficult to detect. Besides obscuring Higgs signals, HEIDI models also provide possible candidates accounting for dark matter and cosmic inflation.
  Unparticle physics also introduces an additional singlet sector, which is assumed to be conformally invariant. This is a special case of HEIDI models [47].

- **Little Higgs** [48]
  In Little Higgs models, the Higgs boson is assumed to be a pseudo-Nambu–Goldstone boson, which has a small mass resulting from a weak violation of a global symmetry. Thus, the Higgs mass is protected from quadratic divergences, which are canceled due to additional particles with masses in the TeV range predicted by the theory.

- **Technicolor** [37]
  The realization of the Higgs mechanism was established first in the theory of superconductors. There, the Higgs boson is represented by a condensate of Cooper

pairs of electrons. Inspired by this, it seems natural to replace the SM Higgs boson by a condensate of fermions to avoid the problems of an elementary scalar particle. In technicolor models, such a bound state originates from a new interaction at a characteristic scale of the order of the vacuum expectation value of the Higgs field. In analogy to QCD, where hadronic bound states consist of elementary colored particles, this new interaction is called technicolor. The bound states, technihadrons, consist of new fundamental fermions, called techniquarks, which feel this interaction. A simple technicolor model provides a mechanism for EWSB and correctly reproduces the masses of gauge bosons. However, it cannot explain the origin of fermion masses without further complification and contradiction with precision measurements.

- **Composite Higgs** [49]
  Composite Higgs models somewhat generalize technicolor. There exist many different types of such models, where the Higgs field usually is a pseudo-Nambu–Goldstone boson of a spontaneously broken global symmetry. By having more freedom in their construction, composite Higgs models can avoid the tension with precision measurements. A composite Higgs boson might not just be a bound state of fermions, but could also contain strongly coupled gauge fields, requiring non-perturbative dynamics. In this situation, however, a duality between strongly coupled four-dimensional theories with conformal invariance and weakly coupled five-dimensional ones can be useful. This duality is based on the famous AdS/CFT correspondence [50]. In some composite Higgs models, the Higgs boson is considered as the holographic counterpart of the fifth component of a gauge field in five dimensions. It is even conjectured that composite Higgs and technicolor models are equivalent to extra-dimensional models, which were described above.

All these approaches show that the SM Higgs mechanism is not the only possible way to break the electroweak symmetry. Instead of one fundamental scalar Higgs boson, there might as well be several or even infinitely many Higgs bosons, none at all or a single one with modified properties. Additionally, new particles of different spin might exist, which are predicted by various models. Up to now, the newly discovered resonance is largely compatible with being the SM Higgs boson and no other new elementary particles have been found. Nevertheless, it is crucial to precisely determine all characteristics of this resonance and to continue the search for other signs of physics beyond the Standard Model in order to be absolutely sure about the origin of electroweak symmetry breaking.

2.3 Identification of the Higgs boson at the LHC

Investigating the origin of electroweak symmetry breaking is one of the main goals of the Large Hadron Collider (LHC) at CERN. The LHC [51] is the most powerful particle accelerator at present. Its first proton-proton collisions took place in 2009. Since then, it has delivered data of $\approx 30\,\mathrm{fb}^{-1}$ at center-of-mass energies of 7 and 8 TeV to the two main multi-purpose experiments ATLAS and CMS. On July 4, 2012, the collaborations of both ATLAS and CMS announced the observation of a new particle at a mass of $125-126$ GeV, which was conjectured to be a Higgs boson. In the following, many studies confirmed that the properties of this new resonance are consistent with being the SM Higgs boson. Since the determination of its features is also the main purpose of the present work, we will briefly discuss in this section how the SM Higgs boson can be produced, observed and identified at the LHC.

2.3.1 Higgs boson Properties

In order to verify or disprove whether the newly discovered resonance is the SM Higgs boson, all its properties have to be investigated experimentally and compared to theoretical predictions. So the starting point is to assemble all the characteristics of the SM Higgs boson given by theory (see Sec. 2.2.1). As mentioned before, its mass is a free parameter (apart from theoretical constraints from unitarity, triviality and vacuum stability). However, as soon as a resonance is discovered experimentally in channels with full mass resolution, the mass is known within some uncertainty range. Therefore, we will assume a mass of 126 GeV here. The characteristics of the SM Higgs boson can then be summarized in the following profile:

- The SM Higgs boson is a neutral, non-colored particle.
- It is a scalar, i.e. its spin is zero.
- It is $\mathcal{CP}$-even.
- Its couplings to gauge bosons and fermions depend on their masses in a specific way.
- It features triple and quartic self-couplings proportional to its mass squared, which can be treated perturbatively due to the light Higgs mass.
- Its width can be calculated to be ≈ 4 MeV for a mass of 126 GeV.
- It unitarizes weak-boson scattering.

The determination of the spin, $\mathcal{CP}$ and couplings to gauge bosons and fermions is a challenging ongoing task, which requires detailed theoretical and experimental investigation of various channels. Higgs boson self-couplings are hardly accessible at the LHC, since they have to be measured from double- or triple Higgs production. A rough estimate on the triple Higgs coupling might be extracted from a future high-luminosity LHC. For a precise determination, however, a future linear collider would be needed. Probing the quartic Higgs coupling is presumably not possible in the near future, since the cross section of triple Higgs production is too tiny [52]. The width of the resonance peak is dominated by the experimental resolution, which is about one GeV for CMS and ATLAS. Therefore, only upper limits can be determined, excluding hypotheses which predict a strong enhancement of the width, e.g. from invisible decays. The unitarization of weak-boson scattering by the SM Higgs or alternative particles will be studied in Sec. 4. Finally, hypotheses postulating a charged or colored 126 GeV resonance could be ruled out easily, since they would lead to predictions for production and decay channels which are different from those of the SM Higgs boson. These production and decay channels and their features will be discussed in the following (for comprehensive reviews, see e.g. Refs. [32], [33] and [53]).

2.3.2 Production and Decay Channels of the SM Higgs boson

At a proton-proton collider, Higgs boson production results from gluons or (light) quarks in the initial state. On the other hand, the SM Higgs boson couples preferentially to heavy particles. Hence, relevant production channels must involve heavy intermediate fields. That is why the four main Higgs production modes at the LHC are gluon fusion, vector-boson fusion, associated production with a weak boson and production in association with a top-antitop pair. Representative Feynman diagrams are shown in Fig. 1 and the corresponding cross sections are given on the left hand side of Fig. 2 for a center-of-mass energy of 8 TeV in the same colors. Some aspects of the calculation of cross sections at hadron colliders will be discussed in Sec. 2.4.

Gluon fusion is the by far dominating Higgs production process at the LHC. Since gluons are massless, the Higgs boson is produced indirectly via a loop of massive quarks, especially the top quark. As there are no further particles in the final state, this channel is rather easy to analyze. From the theory side, however, this process is challenging, since it features large higher-order corrections (see Sec. 3.2.3).

The second-most important production mode is vector-boson fusion (VBF). In contrast to gluon fusion, the NLO QCD corrections, which will be studied in Sec. 3, are rather

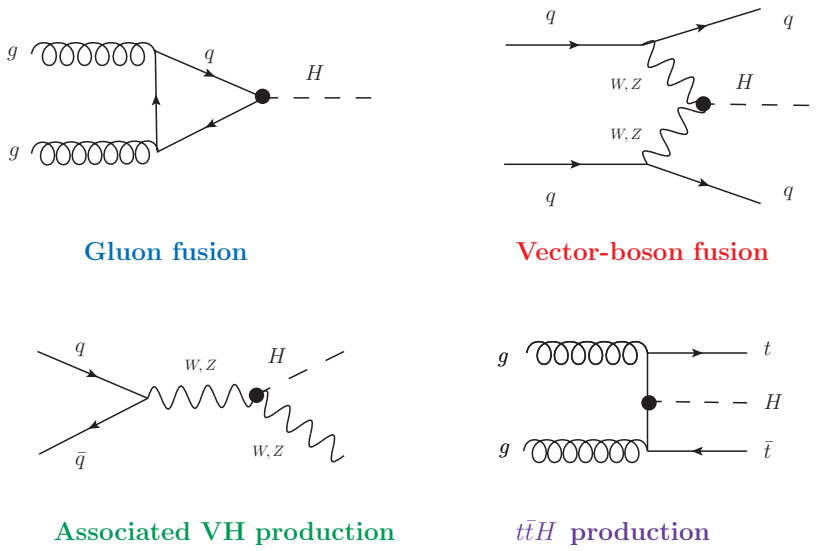

Figure 1: Representative leading order Feynman graphs of the main SM Higgs production channels at the LHC.

small. The two jets in the final state exhibit characteristic features, which can be used to separate the signal from backgrounds: They lie in opposite detector hemispheres, with a large rapidity separation between them, while the decay products of the vector bosons are located at central rapidities.

Due to the high center-of-mass energy of the LHC, where the t-channel weak-boson exchange of VBF dominates over the s-channel VH production, the cross section of associated VH production is smaller than the one of VBF. Furthermore, VH production requires a quark-antiquark initial state, which involves a sea anti-quark from a proton at the LHC. At proton-antiproton colliders, however, a $q\bar{q}$ initial state can be formed by valence quarks. Thus, associated VH production dominates over VBF at the Tevatron. The weak boson V can either be a W or a Z boson. The WH cross section, where the sum over W^+ and W^- is taken, is roughly twice as large as the one of ZH.

Among the main production channels, Higgs boson production in association with a top-antitop quark pair is the one with the smallest cross section, since its final state $t\bar{t}H$ consists of three heavy particles. Moreover, the two top quarks as well as the Higgs boson have different possibilities for further decays, leading to a variety of complicated final states, which have to be analyzed separately. Therefore, $t\bar{t}H$ production is not an actual Higgs discovery channel. Nevertheless, this process is interesting, since it provides access to the top Yukawa coupling.

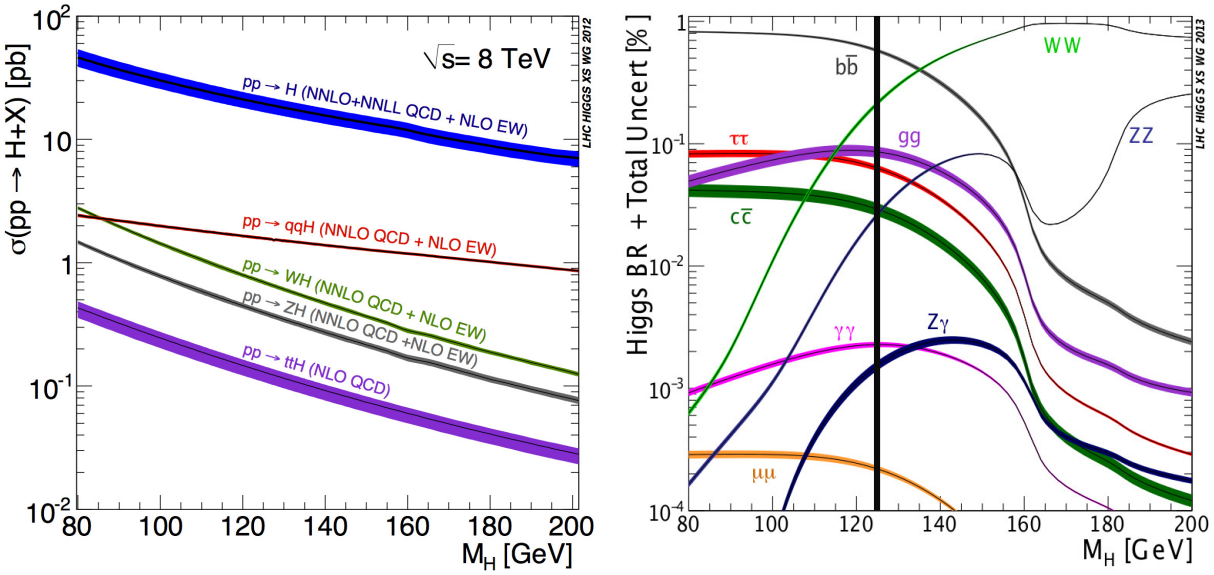

Figure 2: Higgs production cross sections (left hand side) and decay branching ratios (right hand side), taken from the LHC Higgs Cross Section Working Group [54], with an additional vertical line indicating the observed mass. The bands represent parametric and theoretical uncertainties. On the left hand side, labels on the bands specify the included higher-order corrections.

The Higgs boson cannot be detected directly, as it is unstable and decays into other SM particles. In case of a narrow Higgs resonance, production and decay can safely be factorized and treated separately. The relevance of different decay channels strongly depends on the mass of the Higgs boson, which mainly decays into a pair of the heaviest particles allowed by kinematics. This is demonstrated on the right hand side of Fig. 2, with a vertical line indicating the observed mass of 126 GeV. There, the relevance of the different decay modes is given in terms of a branching ratio (BR), which is the probability for a Higgs decay into the given final state. Whereas for a very light Higgs boson, decays into heavy fermions and gluons would completely dominate over decays into weak bosons, it is the other way around for a heavy Higgs. For Higgs masses above around 350 GeV, the decay into $t\bar{t}$ becomes kinematically accessible and yields a further relevant contribution. At a mass of 126 GeV, Higgs decays feature a rich phenomenology, with many different modes contributing.

The dominant channel is the decay into a b anti-b quark pair, with a branching ratio of $\approx 60\%$. Thus, one might think that $H \to b\bar{b}$ is an outstanding Higgs discovery mode. However, this is not the case, since distinguishing the purely hadronic Higgs decay to $b\bar{b}$ is very challenging at a hadron collider, where hadronic backgrounds exceed such Higgs processes by orders of magnitude. The same is true for the $c\bar{c}$ and digluon modes, whose

branching ratios are at the percent level.

With a branching ratio of $\approx 20\%$, the decay to two W bosons is the second largest decay channel for a 126 GeV Higgs. W bosons are also unstable and can decay into a quark-antiquark pair or into a charged lepton and a neutrino. The leptonic W decay modes are among the most important Higgs detection channels, since they feature a clear signature of electrons or muons and missing energy from the invisible neutrinos. However, these channels provide only a poor mass resolution, since the mass peak of the Higgs resonance cannot be fully reconstructed in channels involving neutrinos.

This is different in ZZ decay modes with both Z bosons decaying into pairs of charged leptons. These channels are essential for the discovery as well as the characterization of the Higgs boson and allow for an excellent Higgs mass resolution. However, their rate is quite low because of small branching ratios of the Higgs to two Z bosons and the Z bosons to charged leptons, which are both at the percent level.

The last remaining channel with a branching ratio at the percent level is $H \to \tau^+\tau^-$. Its analysis is challenging, since the τ leptons decay into different leptonic or hadronic final states involving neutrinos. Furthermore, the production via gluon fusion is difficult to access because the Higgs signal can hardly be distinguished from the dominating background of τ pairs from Drell–Yan production. Therefore, VBF and associated VH production with a hadronically decaying weak boson are important production modes for analyses of the $\tau\tau$ channel, since they feature additional jets, which can be used to discriminate the Higgs signal from the background. The $\tau\tau$ decay mode is complementary to other channels, since it provides access to a lepton Yukawa coupling. Other leptonic decay modes, even the dimuon channel, feature minor branching ratios, resulting from small lepton masses.

Although its branching ratio is only $\approx 0.2\%$, the $\gamma\gamma$ channel is one of the main Higgs detection modes. This is because two photons in the final state feature a clean signature with a good mass resolution, which also allows for a distinction of the signal from the irreducible background that can be interpolated from data. The SM Higgs decay into two massless photons (as well as into $Z\gamma$ and gg) is mediated by loops of heavy particles. This leads to a suppression compared to WW and ZZ decays, which would not be present in many BSM scenarios. Thus, measurements of the $\gamma\gamma$ and $Z\gamma$ rates are important elements of the identification of the SM Higgs boson.

2.4 Theoretical Predictions for Hadron Colliders

In order to compare experimental measurements of e.g. Higgs production processes with predictions from theory, precise theoretical calculations and simulations are needed. Some important elements of them will be outlined in this section, focusing on hadron colliders like the LHC. A detailed introduction into these topics can e.g. be found in Ref. [55].

2.4.1 Hadron Collisions

Physical processes at hadron colliders are dominated by the strong interaction, which is described by QCD (see Sec. 2.1). The strength of the interaction is given by the strong coupling $\alpha_s = \frac{g_s^2}{4\pi}$, with g_s defined in Eq. (2.2). This coupling, however, is not a constant, but depends on the energy of the given process. If α_s is known at some energy scale μ (e.g. the mass of the Z boson), this scale can be used as a starting point of the renormalization group evolution

$$\alpha_s(Q^2) = \frac{\alpha_s(\mu^2)}{1 + \alpha_s(\mu^2)\frac{33-2n_f}{12\pi}\ln(\frac{Q^2}{\mu^2}) + \mathcal{O}(\alpha_s^2)} \tag{2.13}$$

to the new energy scale Q. Here, n_f is the number of quark flavors available at the corresponding energy. Since α_s decreases with increasing energy, it becomes small at high energies or small distances, respectively. This feature is known as *asymptotic freedom*. Thus, at high energies, quarks and gluons can be treated as approximately free particles and their interactions can be calculated via a perturbative series in the strong coupling constant. In the soft region, where α_s is large, quarks and gluons are confined to colorless hadrons and the perturbative treatment is not valid any more. Highly-energetic hadron collisions involve both the soft and the hard regime. Fortunately, they can be treated separately according to the factorization theorem [56]. Thus, the cross section of a general hadron-hadron interaction can be written as [57]

$$\begin{aligned}\sigma = \int dx_1\, dx_2 \sum_{\text{subprocesses}} & f_{a_1/h_1}(x_1, \mu_F^2)\, f_{a_2/h_2}(x_2, \mu_F^2) \\ & \frac{1}{2\hat{s}} \int d\Phi_n\, \Theta(\text{cuts}) \overline{\sum} |\mathcal{M}|^2(a_1 a_2 \to b_1 ... b_n).\end{aligned} \tag{2.14}$$

The elements of this equation will be explained in the following. $\overline{\sum}|\mathcal{M}|^2$ denotes the square of the matrix element of a particular hard partonic subprocess, which includes the sum over different colors and polarizations of the final state particles and their average in case of initial state partons. The matrix element $\mathcal{M}(a_1 a_2 \to b_1 ... b_n)$ has a graphic representation in terms of Feynman diagrams and is related to the S-matrix [58], which is

a unitary operator describing the scattering probability. After separating identical initial and final states, where no scattering occurs,

$$S = \mathbf{1} + iT, \tag{2.15}$$

$\mathcal{M}$ is obtained from the T-matrix by requiring four-momentum conservation:

$$\langle p_1 p_2 ... p_n | iT | p_{a_1} p_{a_2} \rangle = (2\pi)^4 \, \delta^4 \left(p_{a_1} + p_{a_2} - \sum_{i=1}^{n} p_i \right) i\mathcal{M}. \tag{2.16}$$

Θ(cuts) is a combination of Heaviside step functions which impose various constraints on the final-state configurations, e.g. to exclude regions which are not accessible to detectors or to separate the signal process from backgrounds. $\hat{s}$ denotes the square of the centre of mass energy for the particular partonic subprocess and $d\Phi_n$ is the Lorentz-invariant phase space element

$$d\Phi_n = \prod_{i=1}^{n} \left(\frac{d^3 \mathbf{p}_i}{(2\pi)^3 \, 2E_i} \right) (2\pi)^4 \, \delta^4 \left(p_{a_1} + p_{a_2} - \sum_{i=1}^{n} p_i \right). \tag{2.17}$$

The partonic substructure of the colliding hadrons is described by the parton distribution functions (PDFs) $f_{a_i/h_i}(x_i, \mu_F^2)$, where x_i is the fraction of the hadron momentum carried by the parton a_i. Inside the hadron, there are soft interactions between the partons, which lead to time-dependent fluctuations of parton momenta. However, the hard scattering occurs during a very short time interval, such that the fluctuations appear frozen. Thus, the process-independent PDFs can be determined once and for all. Since they cannot be calculated perturbatively, they have to be fitted from experimental data. This is done by different collaborations, like CTEQ, MSTW and NNPDF, which use slightly different approaches for the fits as well as for the selection and treatment of data. Such uncertainties of the PDF determination affect the total error of a theoretical prediction. The separation between the hard, perturbative and the soft, non-perturbative part of the cross section (2.14) takes place at the factorization scale μ_F. This unphysical scale is not a priori determined, but sensible choices can be found by exploring relevant scales of the particular process and from comparisons with higher-order corrections. PDF fits are usually performed at a low factorization scale, yet the evolution to any other scale is determined by a perturbative renormalization group equation called DGLAP [59].

Another characteristic of hadron collisions is that the initial momenta of the interact-

ing partons are not known a priori. Only the momentum components transverse to the beam axis (labeled p_T) are known to be zero initially. Together with momentum conservation, this can be used to determine transverse momenta of invisible final-state particles. Another useful observable at hadron colliders is the pseudorapidity η, which is related to the scattering angle θ by [57]

$$\eta = \frac{1}{2} \log \frac{1 + \cos\theta}{1 - \cos\theta} \tag{2.18}$$

and coincides with the rapidity

$$y = \frac{1}{2} \log \frac{E + p_z}{E - p_z} \tag{2.19}$$

in case of massless particles. The advantage of these quantities is that rapidity differences are invariant under boosts along the beam axis, which result from different fractions of the proton momenta carried by the initial-state partons.
The calculation of hadronic cross sections as well as differential distributions of observables like transverse momenta or pseudorapidities is a complex task. Therefore, this is usually performed by means of Monte Carlo generators, which will be described in the following.

2.4.2 Monte Carlo Generators

The cross section (2.14) typically involves matrix elements of high complexity, which have to be integrated over a high-dimensional phase space. In most cases, this integration cannot be performed analytically. Since ordinary methods of numerical integration are time consuming in high dimensions, Monte Carlo generators apply efficient numerical Monte Carlo integration methods for the simulation of hadron collisions. A basic Monte Carlo integration proceeds as follows [60]: In order to calculate the d-dimensional integral

$$I = \int_{V=[0,1]^d} f(\vec{x}) d^d x \tag{2.20}$$

over the unit hypercube $[0,1]^d$, the Monte Carlo algorithm selects N uniformly distributed points $\vec{x}_n$ randomly out of V and determines the estimate I_{MC}, which converges to the true value of the integral according to the law of large numbers,

$$\lim_{N\to\infty} I_{\mathrm{MC}} = \lim_{N\to\infty} \frac{1}{N} \sum_{n=1}^{N} f(\vec{x}_n) = I. \tag{2.21}$$

For finite values of N, the error of the Monte Carlo integration is proportional to $1/\sqrt{N}$. Since the convergence is rather slow in this basic setup, several improvements have been

developed. One of these techniques is importance sampling, which modifies the integration variables as follows:

$$\int f(\vec{x})d^dx = \int \frac{f(\vec{x})}{p(\vec{x})}p(\vec{x})d^dx = \int \frac{f(\vec{x})}{p(\vec{x})}d^dP(\vec{x}). \tag{2.22}$$

Here, $p(\vec{x})$ is a probability density function, which is positive-valued and normalized to unity. If the random numbers are generated according to $P(\vec{x})$, the function $f(\vec{x})$ is replaced by $\frac{f(\vec{x})}{p(\vec{x})}$ in the Monte Carlo estimate and the error given above. Thus, the function $p(\vec{x})$ should be chosen such that it approximates the shape of $f(\vec{x})$. This often requires some advanced knowledge about $f(\vec{x})$, which is not available. Therefore, adaptive algorithms are preferred in practice, which learn about the function during their execution. A common algorithm of this type is VEGAS [61], which adjusts the function $p(\vec{x})$ during several runs of the Monte Carlo integration. Starting from a grid which sub-divides the integration domain, VEGAS performs separate integrations for all the subspaces. Depending on the locations with dominant contributions to the integral, the grid is then modified for the next iteration. By repeating this procedure, the probability density function is approximated until the best grid is found. Then, the integral can be evaluated with high precision. A modified version of the VEGAS algorithm is used by the program VBFNLO, which was used for the purpose of the present work. VBFNLO is a flexible Monte Carlo generator written in FORTRAN, which specializes in the simulation of vector-boson fusion and double or triple vector-boson production at hadron colliders. Furthermore, various BSM scenarios are implemented. As a parton-level program, VBFNLO focuses on the hard process, omitting soft QCD aspects of hadron collisions, such as hadronization or the underlying event. In order to provide precise predictions, next-to-leading order (NLO) QCD corrections are implemented in VBFNLO for most of the processes.

2.4.3 Next-to-leading Order Calculations

At hadron colliders, the hard partonic part of scattering processes can be calculated perturbatively, as mentioned before. The leading order (LO) of the perturbative expansion in the strong coupling often yields only a rough estimate of the cross section because of the rather large value of $\alpha_s(m_Z)$, which is around 0.1. Furthermore, new production channels can arise at NLO, which can have a significant impact on the cross section and differential distributions. Therefore, the calculation of NLO QCD corrections and their implementation into Monte Carlo generators is very important for precise predictions of processes at hadron colliders. For an even higher precision, NLO electroweak corrections should

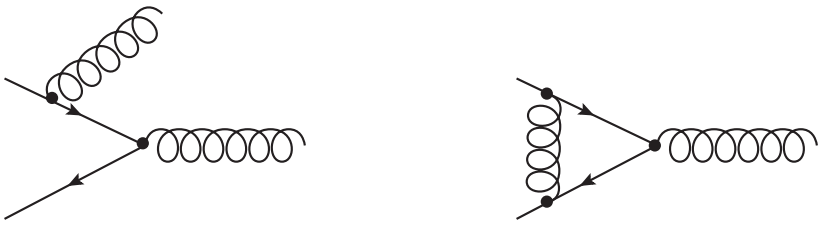

Figure 3: Representative NLO QCD Feynman diagrams. Left hand side: Real emission, right hand side: virtual correction.

also be taken into account. However, since the corresponding coupling α is more than an order of magnitude smaller than α_s, they are not considered within the scope of this work.

A generic cross section at NLO can be written as

$$\sigma_{\mathrm{NLO}} = \sigma_{\mathrm{LO}} + \delta\sigma_{\mathrm{NLO}} = \int_n d\sigma_{\mathrm{LO}} + \int_{n+1} d\sigma_{\mathrm{real}} + \int_n d\sigma_{\mathrm{virt}}, \tag{2.23}$$

where n is the number of final-state particles at LO. It comprises real and virtual corrections, which are exemplified in Fig. 3. The real contributions result from emitting an additional parton, which leads to $n+1$ final-state particles in the phase-space integration. The virtual corrections originate from diagrams with an additional loop, which feature two more vertices than the corresponding LO graphs. Thus, their squared matrix elements contain an additional factor of α_s^2, which gives rise to an NNLO correction. However, the loop diagrams contribute to order α_s via the interference term $2\,\mathrm{Re}(\mathcal{M}_{\text{1-loop}}\mathcal{M}^*_{\mathrm{LO}})$. Different types of loop diagrams are labeled according to their number of external particles attached to the loop: self-energy corrections (two external legs), vertex corrections (three legs, compare Fig. 3), boxes (four legs), pentagons (five legs) etc. A generic feature of one-loop diagrams is that they contain an undetermined four-momentum of a particle in the loop, which, in contrast to external momenta, is not constrained by four-momentum conservation. Thus, it has to be integrated over the whole momentum space, which leads to divergences when the integration variables approach infinity. These ultraviolet (UV) divergences first have to be made explicit, i.e. regularized. This can be done by lowering the dimension of the integral to D instead of four space-time dimensions. If the dimensional regularization scheme is applied, the entire loop is evaluated in D dimensions. Another, finally equivalent, method is dimensional reduction [62]. There, only loop momenta are D-dimensional, whereas polarization vectors or spinors of external particles as well as Dirac matrices remain four-dimensional. To compensate the change of dimension, a new

dimensionful parameter has to be introduced and multiplied to the loop integral with an exponent $4 - D$. This parameter has the dimension of an energy and is denoted as renormalization scale μ_R. Similar to the factorization scale discussed above, it is not a priori determined and has to be chosen appropriately by studying the particular process of interest. Thereby, the change of the cross section with a variation of the renormalization and factorization scale is related to the theoretical uncertainty. It usually decreases when higher-order corrections are included. After regularization, the UV divergences are absorbed in the relations of bare and renormalized quantities by means of an appropriate renormalization procedure.

Both virtual and real corrections exhibit another type of divergences: The infrared (IR) ones, which can either be soft, with a momentum of a massless boson approaching zero, or collinear, with two parallel momenta of massless particles. According to the KLN theorem [63], IR divergences from virtual and real corrections cancel each other when sufficiently inclusive observables are considered. However, this is difficult to realize within a Monte Carlo generator, since the cancellation should occur among different phase-space configurations (see Eq. (2.23)). A common procedure of arranging this cancellation in practice is subtraction. The basic idea behind this method is to add and subtract a local counterterm, which cancels divergences before the actual integration. This can be written as

$$\delta\sigma_{\mathrm{NLO}} = \int_{n+1} d\sigma_{\mathrm{real}} + \int_{n} d\sigma_{\mathrm{virt}} = \int_{n+1} (d\sigma_{\mathrm{real}} - d\sigma_{\mathrm{subtr}}) + \int_{n+1} d\sigma_{\mathrm{subtr}} + \int_{n} d\sigma_{\mathrm{virt}}. \quad (2.24)$$

The counterterm $d\sigma_{\mathrm{subtr}}$ is constructed such that it matches the divergence structure of the real correction. Then, the real minus the subtracted part is finite and can be integrated numerically in four dimensions. Furthermore, the counterterm must be simple enough to be integrated analytically over the one-particle phase space in D dimensions. After performing this integration with the added counterterm, the divergences are regularized and canceled against those from the virtual part. Finally, the result can be integrated numerically in four dimensions. Thus, we can formally write:

$$\delta\sigma_{\mathrm{NLO}} = \int_{n+1} \Big[d\sigma_{\mathrm{real}} - d\sigma_{\mathrm{subtr}} \Big]_{D=4} + \int_{n} \Big[d\sigma_{\mathrm{virt}} + \int_{1} d\sigma_{\mathrm{subtr}} \Big]_{D=4}. \quad (2.25)$$

Suitable counterterms can e.g. be constructed by means of the Catani-Seymour dipole-subtraction formalism [64] as

$$d\sigma_{\text{subtr}} = \sum_{\text{dipoles}} d\sigma_{\text{LO}} \otimes dV_{\text{dipoles}}. \tag{2.26}$$

Here, dV_{dipoles} denotes process-independent dipole factors, which match the divergence structure of the real emission contributions. They are convoluted with an appropriately spin- and color-projected LO cross section, with sums over spin and color indices implicitly assumed. Each dipole factor represents a different kinematical configuration of the $n+1$ particles, which is effectively obtained by first producing an n-particle final state and then splitting one of these particles into two.

3 Higgs Spin Determination: Spin-0 vs. Spin-2

In this section, the characteristics of spin-0 and spin-2 resonances at the LHC will be investigated in order to distinguish the two alternative hypotheses and thus determine the spin of the newly discovered $125 - 126$ GeV resonance. The spin-1 hypothesis can safely be discarded, since the observation of the resonance in the diphoton channel excludes a spin-1 particle due to the Landau–Yang theorem [1]. The present analysis of spin-2 resonances is based on an effective Lagrangian approach, which is introduced first, together with the relevant Feynman rules of the spin-2 particles. This model is implemented into the Monte Carlo program VBFNLO in order to calculate cross sections and differential distributions of spin-2 resonances. After sketching the main aspects of the calculations and implementations, results of the analysis are presented. We focus on resonances produced in gluon fusion and vector-boson fusion in the decay modes $\gamma\gamma$, $W^+W^- \to 2l2\nu$ and $ZZ \to 4l$, which are the most relevant channels for the identification of the SM Higgs boson (see Sec. 2.3.2). In all the different processes, the cross sections of SM Higgs and spin-2 resonances are stated and the spin discrimination power of various differential distributions is studied. Furthermore, their dependence on model parameters and NLO QCD corrections is analyzed. In Sec. 3.7, finally, the phenomenology of heavy spin-2 resonances in VBF is presented.

3.1 The Spin-2 Model

When constructing a theory with spin-2 particles, several different approaches can be adopted (see e.g. Ref. [53]). A naive minimal coupling of a massive spin-2 field with an electromagnetic field leads to the Velo-Zwanziger problem [65] (see also [66]) of superluminal propagation and other inconsistencies. Nevertheless, spin-2 mesons are known to exist from collider experiments. Further detailed investigation of these issues has shown [67] that such a spin-2 model must be interpreted as an effective theory, which features an intrinsic UV cutoff. Above this scale, the model is not valid any more and exhibits pathological features.

In theories with extra dimensions (see Sec. 2.2.2), spin-2 particles appear as Kaluza-Klein (KK) graviton modes, where the graviton couples to the energy-momentum tensor of SM

[1] This conclusion is only valid under certain assumptions: Firstly, that there is only one resonance in all detection channels, not several degenerate ones with different spins observed in different channels. Secondly, this resonance must have a small width, otherwise the theorem cannot be applied. Last but not least, the diphoton final state must be detected unambiguously, without misinterpretation of other final states as two photons.

fields in an effective framework. However, such theories also predict the existence of heavy KK towers of other particles, which haven't been observed yet. Moreover, the graviton couplings are constrained by the theory. Therefore, a KK graviton can easily be distinguished from the SM Higgs, since it cannot reproduce Higgs-like signal strengths [22].
To describe new physics beyond the Standard Model (BSM), such as generic spin-2 particles, in a model-independent way, an effective Lagrangian formalism [68] can be used (see also Ref. [69]). In such an approach, the actual new theory is not developed explicitly, since it is assumed to manifest itself above a high energy scale Λ, which is far from experimental reach. Instead, an effective Lagrangian model is a low-energy approximation of the actual unknown theory, with the effective Lagrangian being an expansion in inverse powers of Λ:

$$\mathcal{L}_{\text{eff}} = \mathcal{L}_0 + \frac{1}{\Lambda}\mathcal{L}_1 + \frac{1}{\Lambda^2}\mathcal{L}_2 + ... \tag{3.1}$$

Since terms of higher order are suppressed by powers of $\frac{E}{\Lambda}$, their impact is expected to be small. Typically, only the first non-vanishing order is kept. An effective Lagrangian can comprise either the SM fields only or additional particles, like the spin-2 particles in the present case. The underlying high-energy theory is assumed to introduce additional heavy particles, whose masses correspond to the energy scale Λ. Although they cannot be produced directly in low-energy reactions, they influence the low-energy interactions through their virtual effects.
Instead of starting from an effective Lagrangian, one can also directly parametrize the general amplitude, without any ordering with respect to energy scales. Then, requiring gauge and Lorentz invariance limits the number of possible terms. Such an approach is applied in Refs. [17,19,20] and will be used later in the present work in Sec. 3.5. Although this approach is somewhat more general, we will mainly focus on the effective Lagrangian method, which features a clear ordering of more or less relevant operators and is consistent beyond leading order in QCD.

For the analysis of spin-2 resonances in vector-boson fusion and gluon-fusion processes, we have constructed an effective Lagrangian model for spin-2 particles interacting with the gauge bosons of the Standard Model [25,26,69]. If not indicated otherwise, we restrict ourselves to the lowest order in the expansion, i.e. to operators of dimension five. Effects of higher-dimensional terms will be studied in Sec. 3.5. Two scenarios are considered: A spin-2 state which transforms as $SU(2)$ singlet and another spin-2 state which is a weak isospin triplet.

These states are described by the general spin-2 fields $T^{\mu\nu}$ (singlet) and $T^{\mu\nu}_j$ (triplet),

$$T^{\mu\nu}_{(j)}(x) = \int \frac{d^3k}{(2\pi)^3 2k^0} \sum_{\lambda=-2}^{2} \Big(\varepsilon^{\mu\nu}(k,\lambda) a_{\lambda(,j)}(k) e^{-ikx} + \varepsilon^{*\mu\nu}(k,\lambda) a^\dagger_{\lambda(,j)}(k) e^{ikx} \Big). \tag{3.2}$$

The free Lagrangian for a general spin-2 field with mass m is given by [70]

$$\mathcal{L}_{\text{free}} = -\left(\partial_\mu T^{\mu\nu}\right)^\dagger \left(\partial_\rho T^\rho{}_\nu\right) + \frac{1}{2}\left(\partial_\rho T^{\mu\nu}\right)^\dagger \left(\partial^\rho T_{\mu\nu}\right) + \frac{m^2}{2}\, T^{\mu\nu\dagger} T_{\mu\nu}\ . \tag{3.3}$$

For the triplet field, the partial derivatives have to be replaced by covariant ones in order to constitute its gauge couplings to electroweak bosons. However, such couplings lead to TTV or $TTVV$ vertices, which do not appear in the processes considered here. The spin-2 fields are symmetric in μ and ν, transverse and $T^\mu_\mu = T^{\mu,j}_\mu = 0$. $\varepsilon^{\mu\nu}$ is a symmetric polarization tensor built from the usual spin-1 polarization vectors [71]:

$$\begin{aligned}
\epsilon^{\mu\nu}(p,\pm 2) &= \epsilon^\mu(p,\pm)\epsilon^\nu(p,\pm) \\
\epsilon^{\mu\nu}(p,\pm 1) &= \frac{1}{\sqrt{2}}\left(\epsilon^\mu(p,\pm)\epsilon^\nu(p,0) + \epsilon^\mu(p,0)\epsilon^\nu(p,\pm)\right) \\
\epsilon^{\mu\nu}(p,0) &= \frac{1}{\sqrt{6}}\left(\epsilon^\mu(p,+)\epsilon^\nu(p,-) + \epsilon^\mu(p,-)\epsilon^\nu(p,+) + 2\epsilon^\mu(p,0)\epsilon^\nu(p,0)\right)\ .
\end{aligned} \tag{3.4}$$

While the spin-2 singlet involves only one uncharged particle T, the triplet consists of three spin-2 particles, T^1, T^2 and T^3. These are rotated into a charged pair and a neutral particle, similarly to the rotation used for the W boson (see Eq. (2.10)):

$$\begin{aligned}
T^\pm &= \frac{1}{\sqrt{2}}(T^1 \mp i\, T^2), \\
T^0 &= T^3.
\end{aligned} \tag{3.5}$$

In this analysis, we only study spin-2 resonances which are produced in gauge-boson fusion and decay into pairs of electroweak bosons. Hence, the present approach is restricted to a model for the interaction of a single spin-2 particle with the SM gauge bosons. Therefore, the building blocks of the corresponding singlet and triplet Lagrangian were chosen to be the spin-2 field(s), the vector fields of the gauge bosons and the scalar field Φ. [2]

[2]This scalar field is assumed to be the Higgs field responsible for electroweak symmetry breaking, though leading to a Higgs boson which is not the new $125-126$ GeV particle discovered at the LHC, but has escaped detection so far, e.g. because it is too heavy. Alternatively, it can correspond to a sigma model accounting for EWSB without a physical Higgs boson (which is the more interesting case in the context of Sec. 4).

Respecting gauge and Lorentz invariance and neglecting higher-dimensional operators, we end up with the following effective Lagrangian corresponding to the singlet case:

$$\mathcal{L}_{\text{singlet}} = \frac{1}{\Lambda} T_{\mu\nu} \left(f_1 B^{\alpha\nu} B^{\mu}_{\ \alpha} + f_2 W_i^{\alpha\nu} W^{i,\mu}_{\ \ \alpha} + 2 f_5 (D^\mu \Phi)^\dagger (D^\nu \Phi) + f_9 \, G_a^{\alpha\nu} G^{a,\mu}_{\ \ \alpha} \right), \tag{3.6}$$

while the Lagrangian for the triplet case reads

$$\mathcal{L}_{\text{triplet}} = \frac{1}{\Lambda} T_{\mu\nu,j} \left(f_6 (D^\mu \Phi)^\dagger \sigma^j (D^\nu \Phi) + f_7 W^{j,\mu}_{\ \ \alpha} B^{\alpha\nu} \right). \tag{3.7}$$

Here, Λ is the characteristic energy scale of the underlying new physics, f_i are variable coupling parameters, $B^{\alpha\nu}$, $W_i^{\alpha\nu}$ and $G_a^{\alpha\nu}$ are the field strength tensors of the SM gauge bosons (see Eq. (2.2)) and D^μ is the covariant derivative

$$D^\mu = \partial^\mu - i g W_i^\mu \frac{\sigma^i}{2} - i g' Y B^\mu. \tag{3.8}$$

The masses of the spin-2 particles are considered as free parameters.
In contrast to the graviton Lagrangian [71], couplings to fermions are not present in our model. However, they could be included straightforwardly by adding further terms, like $\frac{i}{\Lambda} T_{\mu\nu} \bar{\Psi} \gamma^\mu D^\nu \Psi$ or $\frac{i}{\Lambda} T_{\mu\nu} \bar{\Psi} \gamma^5 \gamma^\mu D^\nu \Psi$, with free coupling parameters. This would open up new production and decay modes, which should be studied separately without changing the basic results for the bosonic channels. In the latter, a change of the cross sections because of additional contributions to the decay width of the spin-2 particle could be compensated by an additional free branching ratio parameter (see Appendix A) or by rescaling the energy scale Λ. Another important difference to the graviton Lagrangian is the presence of variable factors f_i, which are not fixed by the underlying theory.
It is possible to write down additional terms including dual field strength tensors $\widetilde{V}^{\alpha\nu} = \frac{1}{2} \varepsilon^{\alpha\nu\rho\sigma} V_{\rho\sigma}$, like $\frac{f_3}{\Lambda} T_{\mu\nu} \widetilde{B}^{\alpha\nu} B^{\mu}_{\ \alpha}$ and $\frac{f_4}{\Lambda} T_{\mu\nu} \widetilde{W}_i^{\alpha\nu} W^{i\mu}_{\ \ \alpha}$. However, such terms yield TVV vertices which vanish for on-shell spin-2 particles, since they are proportional to T^μ_μ. Off-shell contributions do not lead to significant observable effects in the following analysis.
The spin-2 singlet Lagrangian (3.6) yields five relevant vertices which involve two gauge bosons and the spin-2 singlet particle T, namely TW^+W^-, TZZ, $T\gamma\gamma$, $T\gamma Z$ and Tgg. The corresponding Feynman rules are:

$$
\begin{aligned}
TW^+W^- :&\ \frac{2if_2}{\Lambda}K_1^{\alpha\beta\mu\nu} + \frac{if_5 g^2 v^2}{2\Lambda}K_2^{\alpha\beta\mu\nu},\\
TZZ :&\ \frac{2i}{\Lambda}(f_2 c_w^2 + f_1 s_w^2)K_1^{\alpha\beta\mu\nu} + \frac{if_5 v^2}{2\Lambda}(g^2+g'^2)K_2^{\alpha\beta\mu\nu},\\
T\gamma\gamma :&\ \frac{2i}{\Lambda}(f_1 c_w^2 + f_2 s_w^2)K_1^{\alpha\beta\mu\nu},\\
T\gamma Z :&\ \frac{2i}{\Lambda}c_w s_w (f_2 - f_1)K_1^{\alpha\beta\mu\nu},\\
Tgg :&\ \frac{2if_9}{\Lambda}\delta^{ab}K_1^{\alpha\beta\mu\nu}.
\end{aligned}
\tag{3.9}
$$

Here, c_w and s_w denote the cosine and sine of the weak mixing angle defined in Eq. (2.10), v corresponds to the vacuum expectation value of the Higgs field (Eq. (2.6)) and the two different tensor structures are given by

$$
K_1^{\alpha\beta\mu\nu} = p_1^\nu\, p_2^\mu\, g^{\alpha\beta} - p_1^\beta\, p_2^\nu\, g^{\alpha\mu} - p_2^\alpha\, p_1^\nu\, g^{\beta\mu} + p_1 \cdot p_2\, g^{\alpha\nu} g^{\beta\mu}, \tag{3.10}
$$

$$
K_2^{\alpha\beta\mu\nu} = g^{\alpha\nu} g^{\beta\mu}. \tag{3.11}
$$

The indices μ and ν correspond to the spin-2 field (which is symmetric in μ and ν, as mentioned before), α is the Lorentz-index of the first gauge boson, whose incoming four-momentum is denoted as p_1 and β is the Lorentz-index of the second one with four-momentum p_2. a and b are the color indices of the two gluons.
For the spin-2 triplet, it is not possible to describe a gluonic interaction by a term analogous to $\frac{f_9}{\Lambda}T_{\mu\nu}G_a^{\alpha\nu}G^{a,\mu}_{\ \ \alpha}$ in Eq. (3.6). Therefore, the triplet Lagrangian (3.7) yields only four relevant vertices for the uncharged spin-2 particle T^0, which are - apart from the missing T^0gg vertex - the same as in the singlet case. Furthermore, there are two relevant vertices for the charged particles T^+ and T^-. The structure of the Feynman rules is analogous to the singlet case:

$$
\begin{aligned}
T^0W^+W^- :&\ \frac{if_6}{4\Lambda}g^2 v^2 K_2^{\alpha\beta\mu\nu},\\
T^0ZZ :&\ -\frac{if_6}{4\Lambda}(g^2+g'^2)v^2 K_2^{\alpha\beta\mu\nu} - \frac{2if_7}{\Lambda}c_w s_w K_1^{\alpha\beta\mu\nu},\\
T^0\gamma\gamma :&\ \frac{2if_7}{\Lambda}c_w s_w K_1^{\alpha\beta\mu\nu},\\
T^0\gamma Z :&\ \frac{if_7}{\Lambda}(c_w^2 - s_w^2)K_1^{\alpha\beta\mu\nu},
\end{aligned}
$$

$$
\begin{aligned}
T^{\pm}W^{\mp}Z: \; & -\frac{if_6}{4\Lambda} g v^2 \sqrt{g^2+g'^2} K_2^{\alpha\beta\mu\nu} - \frac{if_7}{\Lambda} s_w K_1^{\alpha\beta\mu\nu}, \\
T^{\pm}W^{\mp}\gamma: \; & \frac{if_7}{\Lambda} c_w K_1^{\alpha\beta\mu\nu},
\end{aligned} \tag{3.12}
$$

with $K_1^{\alpha\beta\mu\nu}$ and $K_2^{\alpha\beta\mu\nu}$ defined as in the singlet case (Eq. (3.11)).
The propagator of the spin-2 field with momentum k, which is the Fourier transform of $\left\langle 0 \left| \mathcal{T}\left(T^{\mu\nu}(x) T^{\alpha\beta}(0)\right) \right| 0 \right\rangle$, is given by [71, 72]

$$
\frac{i B^{\mu\nu\alpha\beta}(k)}{k^2 - m_T^2 + i m_T \Gamma_T}, \tag{3.13}
$$

where m_T is the mass of the spin-2 particle, Γ_T is its width and $B^{\mu\nu\alpha\beta}(k)$ is given by

$$
\begin{aligned}
B^{\mu\nu\alpha\beta}(k) = & \frac{1}{2}\left(g^{\mu\alpha}g^{\nu\beta} + g^{\mu\beta}g^{\nu\alpha} - g^{\mu\nu}g^{\alpha\beta}\right) + \frac{1}{6}\left(g^{\mu\nu} + \frac{2}{m_T^2}k^\mu k^\nu\right)\left(g^{\alpha\beta} + \frac{2}{m_T^2}k^\alpha k^\beta\right) \\
& - \frac{1}{2m_T^2}\left(g^{\mu\alpha}k^\nu k^\beta + g^{\nu\beta}k^\mu k^\alpha + g^{\mu\beta}k^\nu k^\alpha + g^{\nu\alpha}k^\mu k^\beta\right).
\end{aligned} \tag{3.14}
$$

Explicit expressions for partial decay widths can be found in Appendix A.
Since the present spin-2 model is based on an effective Lagrangian approach, which is not valid up to arbitrary high energies, it violates unitarity above a certain energy scale. In order to parametrize high-energy contributions beyond this effective model, a formfactor, which is multiplied with the amplitudes, is used:

$$
F_{\text{Spin-2}} = \left(\frac{\Lambda_{ff}^2}{|p_1^2| + \Lambda_{ff}^2} \cdot \frac{\Lambda_{ff}^2}{|p_2^2| + \Lambda_{ff}^2} \cdot \frac{\Lambda_{ff}^2}{|k_{\text{sp2}}^2| + \Lambda_{ff}^2} \right)^{n_{ff}}. \tag{3.15}
$$

Here, p_1^2 and p_2^2 are the squared invariant masses of the initial gauge bosons and k_{sp2}^2 is the squared invariant mass of an s-channel spin-2 particle. The energy scale Λ_{ff} and the exponent n_{ff} are free parameters, describing the scale of the cutoff and the suppression power, respectively.

Another important example for an effective Lagrangian approach is the following parametrization of anomalous couplings of a Higgs boson to electroweak bosons [16, 29, 73], which will be used in Sec. 3.4 to compare different spin-0 and spin-2 scenarios:

$$\mathcal{L}_{\text{Spin-0}} = \frac{1}{\Lambda_5} H \left(g_{5e}^{HWW} W_{\mu\nu}^{+} W_{-}^{\mu\nu} + g_{5o}^{HWW} \widetilde{W}_{\mu\nu}^{+} W_{-}^{\mu\nu} + \frac{g_{5e}^{HZZ}}{2} Z_{\mu\nu} Z^{\mu\nu} + \frac{g_{5o}^{HZZ}}{2} \widetilde{Z}_{\mu\nu} Z^{\mu\nu} + \frac{g_{5e}^{H\gamma\gamma}}{2} A_{\mu\nu} A^{\mu\nu} + \frac{g_{5o}^{H\gamma\gamma}}{2} \widetilde{A}_{\mu\nu} A^{\mu\nu} + g_{5e}^{HZ\gamma} Z_{\mu\nu} A^{\mu\nu} + g_{5o}^{HZ\gamma} \widetilde{Z}_{\mu\nu} A^{\mu\nu} \right) . \quad (3.16)$$

$\widetilde{V}_{\mu\nu}$ are the dual field strength tensors $\widetilde{V}_{\mu\nu} = \frac{1}{2}\varepsilon_{\mu\nu\rho\sigma} V^{\rho\sigma}$, Λ_5 is the energy scale of the underlying new physics and $g_{5e(o)}^{HVV}$ denote the free coupling parameters corresponding to $\mathcal{CP}$-even (-odd) operators.
Analogous to the spin-2 case, a formfactor can be multiplied with the vertices to modify the high-energy behavior, e.g.

$$F_{\text{Spin-0}} = \frac{\Lambda_{ff_0}^2}{|p_1^2| + \Lambda_{ff_0}^2} \cdot \frac{\Lambda_{ff_0}^2}{|p_2^2| + \Lambda_{ff_0}^2} , \quad (3.17)$$

with Λ_{ff_0} describing the energy scale of the cutoff.

3.2 Elements of the Calculation

The present analysis is performed with the parton-level Monte Carlo program VBFNLO (see Sec. 2.4.2), which has been extended to simulate various processes involving spin-2 particles of the model described in Sec. 3.1. Three different classes of processes are studied:

- Vector-boson-fusion processes with different four-lepton final states, which comprise the SM electroweak continuum and additional contributions of spin-2 particles. There, the characteristics of heavy spin-2 resonances are studied in order to allow for a spin determination of hypothetical new, heavy resonances as manifestations of physics beyond the Standard Model, which might be detected at the LHC.

- Spin-2 (or Higgs) resonant vector-boson-fusion processes with the final states $\gamma\gamma$, $W^+W^- \to 2l2\nu$, $ZZ \to 4l$ and $ZZ \to 2l2\nu$. There, the features of a spin-2 resonance are compared to those of a Higgs boson in order to determine the spin of the new $125 - 126$ GeV resonance found at the LHC.

- Spin-2 (or Higgs) resonant gluon-fusion processes with the final states $\gamma\gamma$, $W^+W^- \to 2l2\nu$, $ZZ \to 4l$ and $Z\gamma \to l^+l^-\gamma$, for the same purpose.

Relevant elements of the calculation and the implementation in VBFNLO will be discussed in the following for the different classes of processes. Some of these aspects can also be

found in Refs. [25], [26] or [69]. More technical details and explicit expressions are given in the appendix.

3.2.1 Vector-boson-fusion processes with Spin-2 particles

Vector-boson-fusion processes with four leptons and two jets in the final state, namely $l_1^+ l_1^- l_2^+ l_2^- jj$, $l_1^+ l_1^- \nu_{l_2}\overline{\nu}_{l_2} jj$, $l_1^+ \nu_{l_1} l_2^- \overline{\nu}_{l_2} jj$, $l_1^+ \nu_{l_1} l_2^+ l_2^- jj$ and $l_1^- \overline{\nu}_{l_1} l_2^+ l_2^- jj$, have already been analyzed at NLO QCD accuracy within the SM in VBFNLO. The corresponding calculations, which are described in Refs. [74], [75] and [76], have been extended by the effects of the spin-2 model in order to study the characteristics of heavy spin-2 resonances. Results of this analysis will be presented in Sec. 3.7. The implementation at tree-level (i.e. LO) was already performed within the scope of Ref. [69] and was extended by the corresponding NLO QCD corrections in the present work.
In this class of processes, both resonant and non-resonant contributions in typical VBF phase-space regions are considered. Their Feynman graphs at tree-level can be classified into different topologies, where either one, two or three electroweak bosons are attached to the same quark line. Quark–anti-quark initiated t-channel processes obtained by crossing the respective quark-quark diagrams, and u-channel diagrams, which result from interchanging identical initial- or final-state quarks, are also fully taken into account. However, interference between t- and u-channel contributions can safely be neglected in VBF phase-space regions. s-channel exchange, which corresponds to triple vector-boson production, with one of the time-like bosons decaying into two jets, is considered as a separate process in VBFNLO. However, it is strongly suppressed in VBF phase-space regions and will not be considered here.

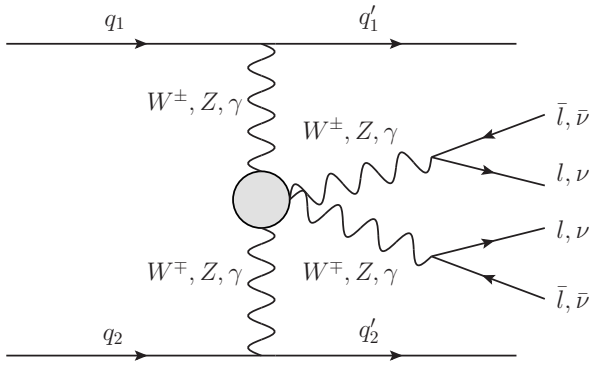

Figure 4: General vector-boson-fusion Feynman graph at tree-level, where spin-2 effects can appear.

The only tree-level topology in which the spin-2 particles of our model can arise is shown

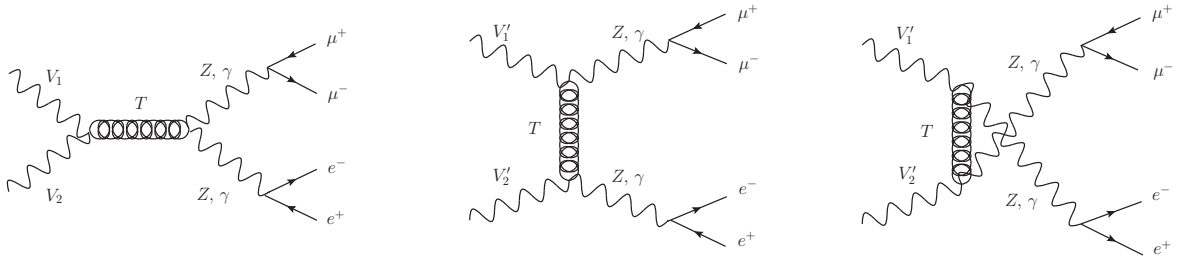

Figure 5: Feynman graphs of the sub-process $VV \to e^+ e^- \mu^+ \mu^-$ involving the spin-2 singlet particle T, with $V_1 V_2 \mathrel{\widehat{=}} W^+W^-, \gamma Z, Z\gamma, \gamma\gamma, ZZ$ and $V_1' V_2' \mathrel{\widehat{=}} \gamma Z, Z\gamma, \gamma\gamma, ZZ$.

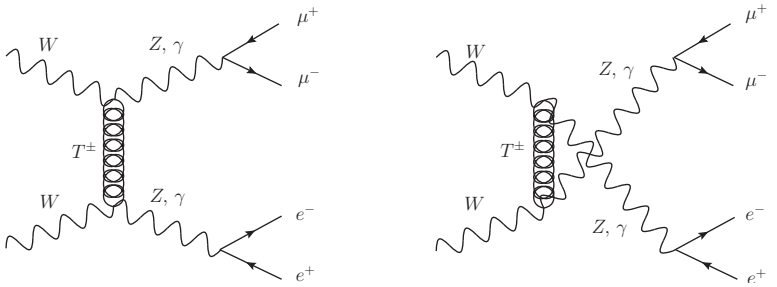

Figure 6: Feynman graphs of the sub-process $VV \to e^+ e^- \mu^+ \mu^-$ involving charged spin-2 triplet particles.

in Fig. 4. Such a topology can be written as

$$\mathcal{M} = \mathcal{J}^{\mu}_{q_1} \mathcal{J}^{\nu}_{q_2} \mathcal{L}_{\mu\nu} \tag{3.18}$$

where the leptonic tensor $\mathcal{L}_{\mu\nu}$ is the electroweak part of the amplitude which results from cutting the propagators which connect the circular area with the quarks. The leptonic tensor comprises various sub-diagrams involving spin-2 or SM particles, which are added coherently.

For $VV \to e^+ e^- \mu^+ \mu^-$, the electroweak sub-process of $pp \to e^+ e^- \mu^+ \mu^- jj$, the additional spin-2 diagrams are depicted in Figs. 5 and 6, respectively. Fig. 5 shows the graphs involving the spin-2 singlet particle T. The diagrams for the neutral spin-2 triplet are the same as for the singlet particle, with T replaced by T^0. The Feynman graphs for contributions of charged triplet particles are depicted in Fig. 6. For the other processes with four leptons and two jets in the final state, the additional Feynman diagrams are analogous and can be found in Ref. [69]. The leptonic tensors for a given process do not change when going from LO to NLO QCD, nor do they differ between quark and anti-quark initiated sub-processes. Therefore, they are calculated only once per phase-space point and then reused, which considerably improves the speed of the program. The

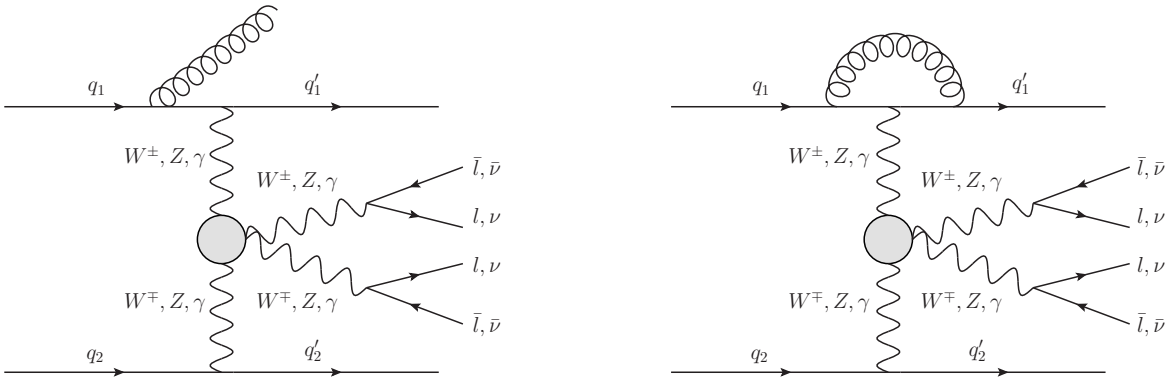

Figure 7: Representative vector-boson-fusion Feynman graphs at NLO QCD. Left hand side: real emission, right hand side: virtual correction.

Feynman diagrams contributing to the leptonic tensors are calculated via calls of HELAS routines [77]. For the calculation of the graphs involving spin-2 particles, new HELAS routines containing the Feynman rules of the spin-2 model had already been created and used in the leptonic tensors for the LO implementation in Ref. [69]. These leptonic tensors have been reused for the NLO implementation of the present work.

Since the spin-2 model only affects the electroweak part of the VBF processes, the NLO QCD corrections are similar to those of the SM and could be adapted from the respective calculations, which are described in detail in Refs. [74] and [78]. The real-emission contributions are obtained by attaching an external gluon to the two quarks lines of Fig. 4 in all possible ways, which also comprises quark-gluon initiated sub-processes. Because of the color-singlet structure of VBF processes, the virtual corrections only comprise graphs with a virtual gluon attached to a single quark line. In the processes considered here, pentagon contributions to the virtual corrections arise, since the electroweak SM continuum contains diagrams with three electroweak bosons attached to a quark line. The other graphs give rise to box, vertex and quark self-energy corrections. Representative Feynman diagrams for the real emission and the virtual corrections are depicted in Fig. 7. In the calculation of the NLO QCD corrections, infrared singularities arise both from virtual corrections and from soft and collinear phase-space regions in the real emission part. They are canceled against each other analytically using the Catani-Seymour dipole-subtraction formalism (see Sec. 2.4.3). The regularization is performed in the dimensional-reduction scheme in $D = 4 - 2\epsilon$ dimensions. For the evaluation of the finite parts of the virtual corrections, the Denner-Dittmaier scheme [79] is applied for five-point functions and the Passarino-Veltman reduction method [80] for loop functions up to four external legs.

Throughout the calculation, the Cabibbo-Kobayashi-Maskawa matrix V_{CKM} is approxi-

mated by the identity matrix. This gives the same results as the exact matrix V_{CKM} for the sum over all quark flavors (as long as no final-state flavor tagging is done and mixing with the massive top quark is neglected), since V_{CKM} is unitary.
Finite-width effects in massive vector-boson propagators are taken into account by using a modified version [81, 82] of the complex-mass scheme [83], where m_V^2 is replaced with $m_V^2 - im_V\Gamma_V$, while a real value for $\sin^2\theta_W$ is kept. This replacement includes the m_V^2 appearing in the spin part of the propagator in the unitary gauge. This approach is analogous to the one implemented in MadGraph [81] and, indeed, the VBFNLO SM amplitudes agree with the ones obtained with MadGraph. In the full complex-mass scheme, the SM amplitudes are gauge invariant. The BSM contributions appear as s-, t- and u-channel spin-2 exchange graphs with a single spin-2 propagator. Since they are derived from the gauge invariant Lagrangians (3.6) or (3.7), the resulting amplitudes are gauge invariant in the absence of finite-width effects. One might worry that using the finite-width propagator (3.13) for the spin-2 fields might break electroweak gauge invariance. We have checked, however, that changing to the overall-factor scheme (which respects gauge invariance), i.e. removing the width from all spin-2 propagators and multiplying the total BSM amplitude with a factor $\frac{p^2-m^2}{p^2-m^2+im\Gamma}$, leaves our results unchanged within the numerical accuracy. Here p, m and Γ denote the momentum, mass and width of the s-channel spin-2 particle. For processes which include diagrams with two or more spin-2 particles, the propagator of Eq. (3.13) would require further modification to insure gauge invariance. However, this complication does not arise in the context of the present work.

3.2.2 Spin-2 resonant Vector-boson-fusion processes

In this class of processes, we want to compare the features of a 126 GeV Higgs resonance and a spin-2 resonance of the same mass. To this end, we only consider resonant diagrams, which are illustrated in Fig. 8 for the WW channel at tree level. Here, T denotes either the spin-2 singlet or the neutral triplet particle. For the other channels, the diagrams are analogous. In spin-2-resonant processes with leptonic final states, we also include intermediate virtual photons instead of Z bosons. In case of Higgs-resonant diphoton production, an effective $H\gamma\gamma$ coupling is used [81]. Higgs and spin-2 production are implemented as two separate options in order to compare the characteristics of both types of resonances. The SM continuum contributions are omitted in both cases, as interference effects are small due to the narrowness of the Higgs or spin-2 resonance. We have analyzed the non-resonant spin-2 contributions as well, yet they were found to yield no significant modifications and therefore are omitted as well. All the Higgs-resonant

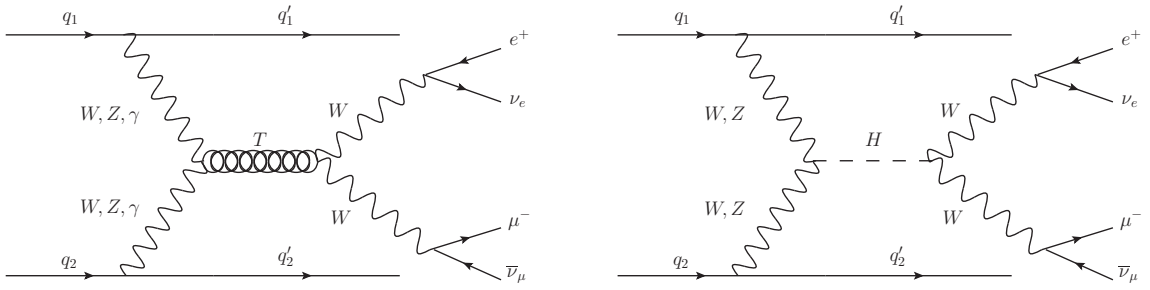

Figure 8: Tree-level Feynman graphs of the VBF process $pp \to W^+W^- jj \to e^+\nu_e \mu^- \overline{\nu}_\mu jj$. Left hand side: via a spin-2 resonance, right hand side: via a Higgs resonance.

processes we study here were already available in VBFNLO at NLO QCD accuracy within the narrow-width approximation [29, 78]. The implementation of the spin-2- (or Higgs-) resonant $\gamma\gamma$ channel at tree-level was already performed within the scope of Ref. [69] and was extended by the corresponding NLO QCD implementation in the present work. The channels $W^+W^- \to 2l2\nu$, $ZZ \to 4l$ and $ZZ \to 2l2\nu$ were implemented as new VBFNLO processes at NLO QCD accuracy and feature the option to switch between a Higgs and a spin-2 resonance. Again, the NLO QCD corrections could be adapted from existing SM calculations, as the resonance is part of the electroweak sub-process. Here, the virtual corrections are much simpler than those described in the previous section: They only comprise vertex and quark self-energy corrections (the latter vanishing for massless particles), since the resonant processes contain only diagrams with one electroweak bosons attached to a quark line.

The spin-2 resonant part of the processes has been calculated by means of the HELAS routines mentioned before as well as with a new second code which directly determines the spin-2 resonance contributions to the leptonic tensors (see Appendix B for more details). Firstly, this served as a check of the spin-2 implementation and secondly, the direct code considerably improves the speed of the program. The remaining parts of the processes were checked by comparing the new Higgs-resonant options with the corresponding existing VBFNLO processes in the narrow-width approximation.

3.2.3 Spin-2 resonant Gluon-fusion processes

Gluon-induced diboson-production processes [84] were already available in VBFNLO at leading order, that is at the one-loop level for Higgs-boson production, including anomalous Higgs couplings to electroweak bosons for the decays. For the present work, these implementations were extended by spin-2-resonant processes in the effective Lagrangian approach, again omitting non-resonant diagrams. Like in resonant VBF processes (Sec. 3.2.2),

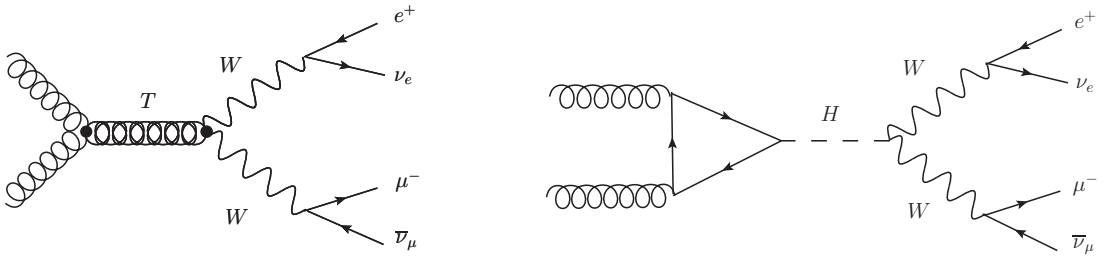

Figure 9: Feynman graphs of the process $gg \to W^+W^- \to e^+\,\nu_e\,\mu^-\,\overline{\nu}_\mu$.
Left hand side: via a spin-2 resonance, right hand side: via a Higgs resonance.

the option to switch between either a Higgs or a spin-2 resonance is provided. The contributing graphs are exemplified in Fig. 9 for WW production. Again, intermediate virtual photons leading to a leptonic final state are also included in the spin-2-resonant processes $gg \to ZZ \to 4l$ and $gg \to Z\gamma \to l^+l^-\gamma$. The spin-2-resonant processes are calculated via a new fast code and were cross-checked by implementing a second version with spin-2 HELAS routines, including newly written ones for the Tgg interaction and for higher-dimensional spin-2 structures studied in Sec. 3.5 (see also Appendix B). The corresponding new contributions to the decay width of the spin-2 particle were calculated by using the mathematica packages FeynArts [85] and FormCalc [86] and can be found in Appendix A.

In this approach, we assume that higher-order QCD corrections for spin-2-resonant production in gluon fusion are the same as for Higgs production, since the Tgg coupling is somewhat analogous to the effective Hgg coupling, which originates from the operator structure $HG^{\mu\nu}_a G^a_{\mu\nu}$. So in order to account for higher-order QCD corrections up to NNLL, which have sizable effects for Higgs production via gluon fusion [87,88], the LO cross sections calculated with VBFNLO are multiplied with a K-factor of 2.6. This K-factor was obtained by comparing with the value given in Ref. [89] (removing NLO electroweak corrections of about 5% [90] included therein). Due to the scale choice $\mu_F = \mu_R = m_h = 126$ GeV for gluon fusion (see Sec. 3.2.4), this K-factor is rather high. With $\mu_F = \mu_R = m_h/2$, it would be only ≈ 2.1, because of a higher LO cross section. Since higher-order QCD corrections also affect the decay of the spin-2 particle to gluons, the corresponding partial decay width is multiplied with the K-factor 1.7, again following results obtained for the $H \to gg$ decay [91]. Note that only the assumed ratio of K-factors is relevant for spin-2 phenomenology, since the overall coupling strength of the spin-2 resonance to gluons, f_9/Λ, is a free parameter in the present model.

3.2.4 Input parameters and selection cuts

As electroweak input parameters, $G_F = 1.16637 \cdot 10^{-5}\,\text{GeV}^{-2}$, $m_W = 80.399$ GeV and $m_Z = 91.1876$ GeV are used, which are taken from results of the Particle Data Group [92]. By using tree-level electroweak relations, $\sin^2\theta_w$ and α are derived from these quantities. We use the CTEQ6L1 [93] parton distribution function (PDF) set at LO and CT10 [94] PDFs at NLO with $\alpha_s(m_Z) = 0.118$. Jets are recombined from the final-state partons via the $k_\perp$ jet finding algorithm [95]. In vector-boson-fusion processes, the factorization scale and the renormalization scale are set to $\mu_F = \mu_R = Q = \sqrt{|q_{if}^2|}$, with q_{if} being the 4-momentum transfer between the respective initial and final state quarks at LO or, at NLO, the virtuality of the incoming weak bosons. With this scale choice, LO results were found to give a good approximation of NLO cross sections and distributions, while the NLO results are hardly sensitive to the scale choice [76]. For gluon fusion or quark–antiquark-initiated diboson-production processes, a fixed scale of 126 GeV is taken as factorization and renormalization scale.

Vector-boson-fusion events are characterized by two tagging jets, which are the jets of highest transverse momentum. They are located in the forward regions of the detector, while the decay products of the vector bosons (or the final-state photons, respectively) lie in the central-rapidity region between them. By imposing the following cuts in the VBF channels, these features can be employed to improve the signal-to-background ratio.
The two tagging jets are required to lie inside the rapidity range which is accessible to the detector and to have sizable transverse momenta:

$$|\eta_j| < 4.5, \qquad p_{T,j} > 30\,\text{GeV}. \tag{3.19}$$

They are reconstructed from massless partons with pseudorapidity $|\eta| < 5$ and have to be well separated:

$$\Delta R_{jj} \equiv \sqrt{(\eta_{j1} - \eta_{j2})^2 + (\phi_{j1} - \phi_{j2})^2} > 0.7. \tag{3.20}$$

Because of the characteristic VBF kinematics, a large rapidity separation and a large invariant mass of the tagging jets is required, [3]

$$\Delta\eta_{jj} > 4, \qquad m_{jj} > m_{jj}^{\text{min}}. \tag{3.21}$$

[3] $m_{jj}^{\text{min}} = 1000$ GeV for the process $pp \to e^+\,\nu_e\,\mu^-\,\overline{\nu}_\mu\,jj$ in Sec. 3.7 and $m_{jj}^{\text{min}} = 500$ GeV for all other VBF processes.

Additionally, the tagging jets have to lie in opposite detector hemispheres,

$$\eta_{j1} \times \eta_{j2} < 0. \tag{3.22}$$

The charged decay leptons (or decay photons, respectively) are required to be located at central rapidities, to be well-separated from the jets and to fall into the rapidity gap between the two tagging jets:

$$|\eta_l| < 2.5, \qquad \Delta R_{lj} > 0.4, \qquad \eta_{j,\min} < \eta_l < \eta_{j,\max}. \tag{3.23}$$

Here, depending on the considered process, l denotes a charged lepton or a final-state photon. In the leptonic decay modes, we apply a cut on the invariant mass of two oppositely charged leptons,

$$m_{ll} > 15\,\text{GeV} \tag{3.24}$$

and require the transverse momentum of the charged leptons to be

$$p_{T,l} > 10\,\text{GeV} \;\text{ in the } WW \text{ and } \; p_{T,l} > 7\,\text{GeV} \;\text{ in the } ZZ \text{ channel.} \tag{3.25}$$

In the diphoton channel, the photons are supposed to be hard, with

$$p_{T,\gamma} > 20\,\text{GeV}. \tag{3.26}$$

To have well isolated photons, we require a minimal photon-photon separation

$$\Delta R_{\gamma\gamma} > 0.4 \tag{3.27}$$

and apply a photon isolation from hadronic activity as recommended in Ref. [96] with separation parameter $\delta_0 = 0.7$, efficiency $\epsilon = 1$ and exponent $n = 1$.

By applying this set of cuts, the LO differential cross sections are finite, as they lead to finite scattering angles of the two jets. In the NLO calculation, initial-state singularities appear, resulting from collinear quark- and gluon splittings ($q \to qg$, $g \to q\bar{q}$). They are factorized into the PDFs. Furthermore, divergences from t-channel exchange of photons with low virtuality emerge in the real-emission contribution, when the additional radiated parton is resolved as a separate jet, but for the other quark line, the initial and final-state quarks become collinear. These divergences, which are of electroweak origin, could be eliminated by including a photon density in the PDFs. However, they can also

be removed by applying an extra cut on the virtuality of the photon,

$$Q_\gamma^2 > 4\,\mathrm{GeV}^2, \tag{3.28}$$

which is done in the present analysis. The precise treatment of these divergences does not affect cross sections appreciably, particularly if VBF cuts are imposed [82].
In Sec. 3.7, where distributions of a heavy spin-2 resonance in VBF processes are studied, it is convenient to cut off contributions which do not originate from the resonance. To this end, a minimal and a maximal invariant-mass cut of the final-state lepton system can be applied. This will be specified in Sec. 3.7.

In case of gluon fusion, we impose the same cuts on the charged decay leptons as in VBF, with

$$p_{T,l} > 10\,\mathrm{GeV}, \qquad |\eta_l| < 2.5, \qquad m_{ll} > 15\,\mathrm{GeV} \tag{3.29}$$

for the $W^+W^- \to l^+\nu l^-\bar{\nu}$ decay channel (and also for the diboson-production background) and

$$p_{T,l} > 7\,\mathrm{GeV}, \qquad |\eta_l| < 2.5, \qquad m_{ll} > 15\,\mathrm{GeV} \tag{3.30}$$

for $ZZ \to 4l$. In the diphoton mode, we again require

$$p_{T,\gamma} > 20\,\mathrm{GeV}, \qquad |\eta_\gamma| < 2.5, \qquad \Delta R_{\gamma\gamma} > 0.4. \tag{3.31}$$

Finally, the cuts for $gg \to Z\gamma \to l^+l^-\gamma$ are chosen as

$$p_{T,\gamma} > 15\,\mathrm{GeV},\ p_{T,l} > 10\,\mathrm{GeV}, \quad |\eta_l| < 2.5,\ |\eta_\gamma| < 2.5, \quad \Delta R_{ll} > 0.4,\ \Delta R_{l\gamma} > 0.4. \tag{3.32}$$

To eliminate unwanted off-shell contributions in phase space regions where some of our approximations fail, we apply an additional cut on the invariant mass of all final-state leptons and/or photons of ± 10 GeV around the 126 GeV resonance in all gluon-fusion processes.

3.3 Vector-boson Fusion

In this section, numerical results of the analysis of SM Higgs and spin-2 resonances in Vector-boson fusion are presented (see also Refs. [25, 26]). We consider the channels $\gamma\gamma$, $W^+W^- \to 2l2\nu$ and $ZZ \to 4l$, which represent the most important decay modes for the observation and analysis of the Higgs boson at the LHC (see Sec. 2.3.2). Cross sections

of $ZZ \to 2l2\nu$ are also included for illustration. We list the cross sections at LO and NLO QCD accuracy, discuss transverse-momentum distributions and the relevance of the formfactor (3.15) and present distributions which allow us to distinguish between spin-0 and spin-2. Additionally, different parameter settings of the spin-2 model are studied and the spin-2 singlet is compared to the spin-2 triplet scenario. Furthermore, the impact of the NLO QCD corrections is analyzed.
If not indicated otherwise, we consider a spin-2 singlet resonance with couplings

$$f_1 = 0.04, f_2 = 0.08, f_5 = 10, f_{i\neq 1,2,5} = 0 \quad \text{and} \quad \Lambda = 21\,\text{TeV}. \tag{3.33}$$

The Tgg coupling f_9, which has no equivalent in the triplet scenario, is set to zero throughout this section. This means we assume that all spin-2 particles couple only to electroweak bosons in this analysis of electroweak-boson fusion. The parameters of the formfactor are

$$\Lambda_{ff} = 400\,\text{GeV}, \quad n_{ff} = 3. \tag{3.34}$$

For the triplet scenario, we use the same formfactor parameters, but set the couplings to

$$f_6 = 8, f_7 = 0.047, f_{i\neq 6,7} = 0, \quad \Lambda = 8\,\text{TeV}. \tag{3.35}$$

These parameters are chosen in order to approximately reproduce the cross sections and transverse momentum distributions of a SM Higgs boson in the different VBF channels at the LHC (see below). The mass of the Higgs boson and the spin-2 particles is set to 126 GeV and we assume pp collisions at a centre of mass energy of 8 TeV. If not indicated otherwise, differential distributions are determined in the laboratory frame. In the following, when figures compare different values of coupling parameters, couplings f_i which are not given explicitly are set to zero and Λ is adjusted such that the cross section is approximately the same as the one of the SM Higgs resonance. Possible effects of a finite detector resolution were analyzed by performing a Gaussian smearing of the energy and the transverse momenta of the final-state particles in the diphoton channel. To this end, we used an in-house routine based on a CMS Monte-Carlo study [97] (for further details, see also Ref. [69]). However, this smearing was found to have no significant influence on the distributions we studied. Therefore, the results which are presented here were obtained without smearing.
Due to the free coupling parameters f_i of the Lagrangians (3.6) and (3.7), cross sections of spin-2 resonances can be tuned such that they mimic those of a SM Higgs boson within

Final State	Resonance	LO cross sec. [fb]	NLO cross sec. [fb]
$\gamma\gamma$	SM Higgs	0.7348	0.7448
	Spin-2 singlet	0.7711	0.7878
	Spin-2 triplet	0.7314	0.7475
$W^+W^- \to e^+\,\nu_e\,\mu^-\,\overline{\nu}_\mu$	SM Higgs	0.6515	0.6620
	Spin-2 singlet	0.5453	0.5585
	Spin-2 triplet	0.5377	0.5506
$ZZ \to e^+\,e^-\,\mu^+\mu^-$	SM Higgs	$1.038 \cdot 10^{-2}$	$1.056 \cdot 10^{-2}$
	Spin-2 singlet	$0.8727 \cdot 10^{-2}$	$0.8946 \cdot 10^{-2}$
	Spin-2 triplet	$0.8701 \cdot 10^{-2}$	$0.8920 \cdot 10^{-2}$
$ZZ \to e^+\,e^-\,\nu_\mu\overline{\nu}_\mu$	SM Higgs	$3.435 \cdot 10^{-2}$	$3.492 \cdot 10^{-2}$
	Spin-2 singlet	$2.707 \cdot 10^{-2}$	$2.773 \cdot 10^{-2}$
	Spin-2 triplet	$2.694 \cdot 10^{-2}$	$2.759 \cdot 10^{-2}$

Table 1: Integrated cross sections for SM Higgs, spin-2 singlet and triplet resonances with parameters as given in Eqs. (3.33), (3.34) and (3.35) in different vector-boson-fusion processes at LO and NLO QCD accuracy. The cuts of Section 3.2.4 are applied. Statistical errors from the Monte Carlo integration are less than one per mill.

experimental and theoretical uncertainties. This is not only possible for single production and decay modes, but simultaneously for all the channels studied here (and also for gluon fusion, see Sec. 3.4). In case of a SM Higgs boson, the decay to two photons is suppressed compared to WW and ZZ decays, since the $H\gamma\gamma$ coupling is loop-induced. A similar suppression can be achieved in our spin-2 model by tuning the different couplings f_i. In the Feynman rules of the spin-2 singlet scenario (3.9), the coupling f_5 appears only in the TWW and TZZ Vertex, but not in $T\gamma\gamma$ and $T\gamma Z$. So by choosing $f_5 \gg f_1,\ f_2$ the decay to $\gamma\gamma$ can be suppressed compared to WW and ZZ. Such a suppression can also be achieved in the triplet case with $f_6 \gg f_7$, since the structure of the Feynman rules (3.12) is analogous. That this kind of tuning is in fact possible for our parameter choice given above is illustrated in Table 1, which shows the integrated cross sections for a SM Higgs and a spin-2 singlet or triplet resonance in different VBF processes at LO and NLO QCD accuracy. It is important to note that for graviton spin-2 models, it is not possible to obtain Higgs-like ratios in such a way [22].

Due to the scale choice $\mu_F = \mu_R = Q$ (see Sec. 3.2.4), the NLO QCD corrections in the VBF channels are quite small. They are roughly the same for Higgs and spin-2 resonances, since the resonance is contained in the electroweak part of the process, whereas the NLO corrections only affect the QCD part.

Table 2 gives a comparison of the integrated cross sections of a Higgs and a spin-2 singlet resonance for the LHC at a centre of mass energy of 8 TeV and 14 TeV, exemplified for

	LO cross section [fb]		NLO cross section [fb]		$K = \frac{\sigma_{\text{NLO}}}{\sigma_{\text{LO}}}$	
$\sqrt{S}$	8 TeV	14 TeV	8 TeV	14 TeV	8 TeV	14 TeV
SM Higgs	0.7348(3)	2.179(1)	0.7448(4)	2.241(1)	1.014	1.028
Spin-2 singlet	0.7711(4)	2.409(1)	0.7878(4)	2.495(1)	1.022	1.036

Table 2: Integrated cross sections for a SM Higgs and a spin-2 singlet resonance at LO and NLO QCD accuracy for VBF photon pair-production at different centre of mass energies. The statistical errors from the Monte Carlo integration are given in brackets.

VBF photon pair-production. The shape of the distributions shown below is identical in both cases, so we will restrict ourselves to the 8 TeV case there.
The width of the Higgs resonance is only ≈ 4 MeV, whereas the width of the spin-2 resonance depends on the model parameters, but is even much smaller than the one of the Higgs boson for the different default parameter settings of this section and Sec. 3.4. In principle, the width of the spin-2 resonance can be adjusted to the one of the Higgs by multiplying it with an appropriate branching ratio parameter, which quantifies the amount of additional, possibly hard to detect, decay modes of the spin-2 particle (see Appendix A). At the same time, Λ can be rescaled such that the cross sections remain comparable to the Higgs case. However, the resonance peak, which can be reconstructed either in the diphoton or the $ZZ \to 4l$ channel at the LHC, features a width which is dominated by the experimental resolution. Therefore, these details do not play any role.

3.3.1 Transverse-momentum distributions and formfactor

Since it is not possible to distinguish spin-0 from spin-2 on the basis of cross sections alone, the next step is to study differential distributions for this purpose. Fig. 10 and 11 depict the normalized transverse-momentum distributions of a final-state photon or lepton and of the tagging jet with the largest transverse momentum for a SM Higgs and a spin-2 singlet resonance with and without the formfactor (3.15) at NLO QCD accuracy. For a spin-2 resonance without the formfactor (or with $n_{ff} = 0$ or $\Lambda_{ff} \to \infty$, respectively), the transverse momenta of the photons, leptons and jets are much higher than for a Higgs boson, so that both cases could be easily distinguished from one another via these p_T distributions. However, the harder transverse-momentum distributions for the spin-2 case without our specific formfactor setting originate from the higher energy dimensions of the couplings in the effective Lagrangians (3.6) and (3.7) instead of being an indicator of the spin. Furthermore, unitarity of the S-matrix in elastic weak-boson scattering is violated for the present spin-2 model if no formfactor is applied (for more details, see Ref. [69]). By a judicious choice of the formfactor, like Eq. (3.15) with $\Lambda_{ff} = 400\,\text{GeV}$, $n_{ff} = 3$,

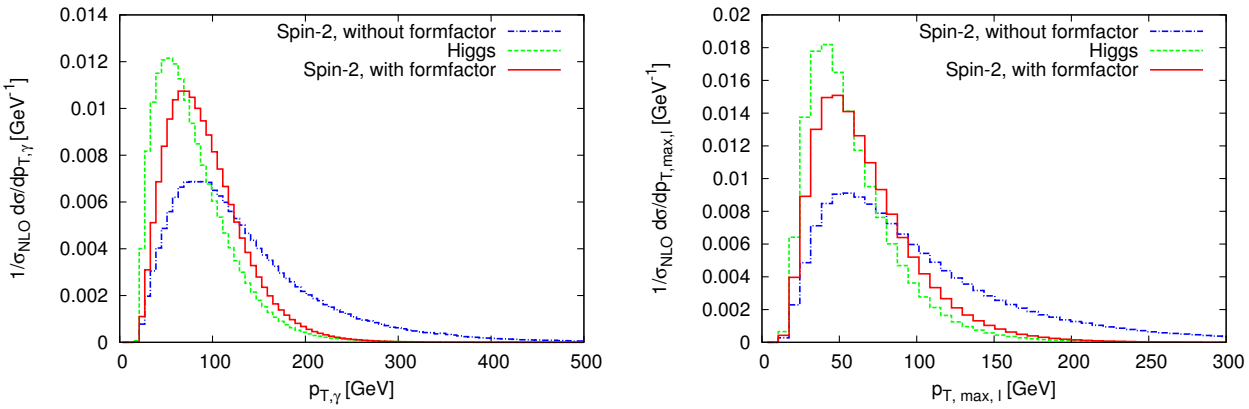

Figure 10: Transverse-momentum distributions for a SM Higgs and for a spin-2 singlet resonance with couplings $f_1 = 0.04, f_2 = 0.08, f_5 = 10, f_{i\neq 1,2,5} = 0$, with and without formfactor, at NLO QCD accuracy. Left hand side: p_T of a final-state photon in the VBF $\gamma\gamma$ channel, right hand side: p_T of the of the hardest final-state lepton in VBF $W^+W^- \to e^+\,\nu_e\,\mu^-\,\overline{\nu}_\mu$.

the p_T distributions of the spin-2 resonance can be adjusted to closely resemble those of the Higgs boson. This is simultaneously possible for the transverse momenta of the final-state photons or leptons and the jets in $\gamma\gamma$, WW and ZZ decays within our set of formfactor parameters, which is illustrated in Fig. 10 and 11 for $\gamma\gamma$ and WW and looks similar in the ZZ mode. Therefore, transverse-momentum distributions which look like those of the Higgs would not be a proof for a Higgs resonance. These distributions could originate from a spin-2 resonance with an adequate formfactor as well. In fact, a similar behavior was found in Ref. [73] for a Higgs boson with effective couplings (Eq. (3.16)). From now on, the formfactor parameters are set to $\Lambda_{ff} = 400\,\text{GeV}$, $n_{ff} = 3$ throughout this subsection.

On the left hand side of Fig. 12, the impact of the NLO QCD corrections on the transverse momentum of the hardest jet is exemplified for the diphoton channel. In order to compare the shape, LO distributions are normalized to the LO cross section and NLO distributions to the NLO cross section there. The NLO corrections tend to shift the distributions to smaller values of p_T, since a fraction of the total transverse momentum is carried by the additional gluon in the real emission contribution. This feature is analogous to the SM case [74, 78] and independent of the spin of the resonance. For spin-0 and spin-2, this is shown in Fig. 12, while an analogous plot for spin-1 can be found in Ref. [30]. Due to the present scale choice, the impact of the NLO corrections is small, as it is for the integrated cross section as well (see Tables 1,2). While the K-factor in the high p_T region ($400\,\text{GeV} < p_{\text{T, max, jet}} < 900\,\text{GeV}$) is around 0.9 for the spin-2 case with $\mu_F = \mu_R = Q$, it would be around 0.6 if we had chosen $\mu_F = \mu_R = m_W$ instead, mainly because of a higher

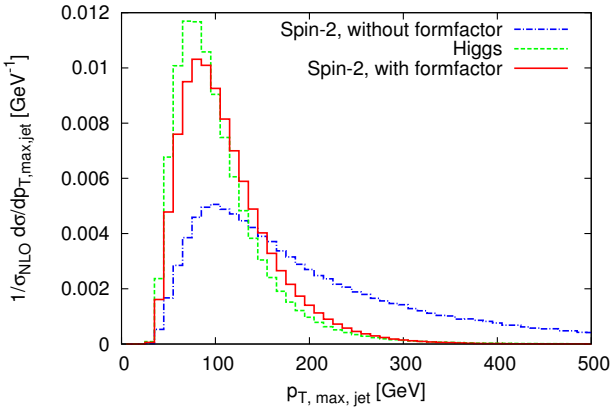

Figure 11: p_T distribution of the tagging jet with the largest transverse momentum in the VBF $\gamma\gamma$ channel for a SM Higgs and for a spin-2 singlet resonance with couplings $f_1 = 0.04, f_2 = 0.08, f_5 = 10, f_{i\neq 1,2,5} = 0$, with and without formfactor, at NLO QCD accuracy.

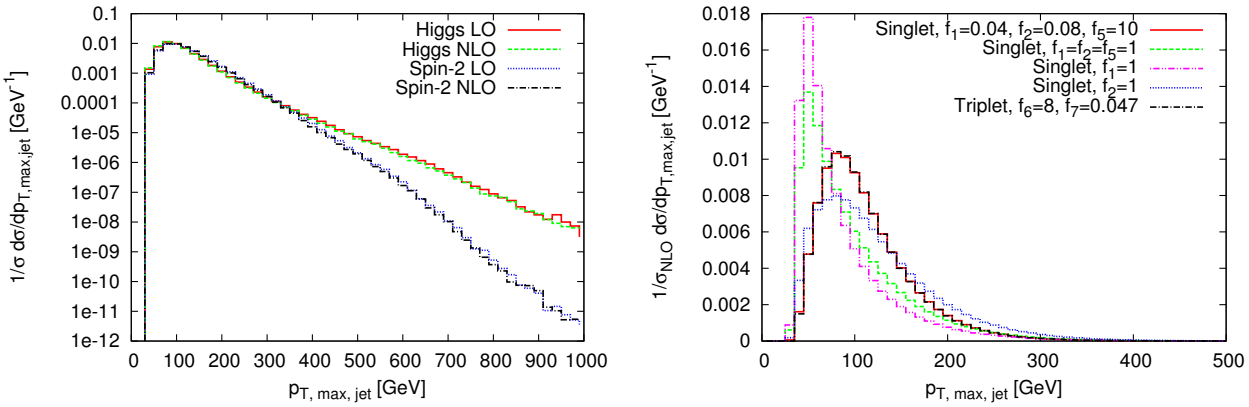

Figure 12: Normalized p_T distribution of the tagging jet with the largest transverse momentum in the VBF $\gamma\gamma$ channel. Left hand side: Higgs and spin-2 singlet resonance with parameters as given in Eq. (3.33) and the formfactor settings of Eq. (3.34) at LO and NLO QCD accuracy on a logarithmic scale. Right hand side: Spin-2 singlet and triplet resonance with different coupling parameters and the formfactor settings of Eq. (3.34) at NLO QCD accuracy.

prediction for the LO cross section.

The transverse-momentum distributions of a spin-2 resonance depend slightly on the coupling parameters, which is exemplified on the right hand side of Fig. 12 for the transverse momentum of the hardest jet in the $\gamma\gamma$ mode. This can be understood from the Feynman rules (3.9): For $f_1 = 1, f_{i\neq 1} = 0$, spin-2 resonances are mainly produced by initial photons, which leads to an enhancement of the low p_T region, while for the cases $f_2 = 1, f_{i\neq 2} = 0$ and $f_1 = 0.04, f_2 = 0.08, f_5 = 10$, initial W and Z bosons dominate. The transverse-

momentum distributions of the spin-2 triplet resonance resemble those of the singlet with corresponding couplings. Therefore, they can be adjusted to those of the Higgs boson with the same formfactor settings.

3.3.2 Azimuthal angle difference between the two tagging jets

In the following, we will study various angular and mass distributions which can be used to distinguish between spin-0 and spin-2 in the different VBF channels. Furthermore, the impact of the NLO QCD corrections and model parameters on these distributions will be illustrated. If not indicated otherwise, distributions are presented at NLO QCD accuracy. Note that the following figures include a normalization factor $1/\sigma_{\text{NLO}}$.
An excellent angular distribution in terms of a spin determination in all the VBF processes studied here is the azimuthal angle difference between the two tagging jets, $\Delta\Phi_{jj}$. The Figures 13 and 14 depict the respective distribution for a SM Higgs and a spin-2 singlet resonance at LO and NLO QCD accuracy in the $\gamma\gamma$, WW and ZZ channel. In all the cases, the $\Delta\Phi_{jj}$ distribution features a clear difference between a SM Higgs and a spin-2 resonance, which is not modified by the NLO corrections, the curves are just slightly shifted according to the overall K-factor. Different spin-2 couplings lead to a slightly different $\Delta\Phi_{jj}$ distribution of a spin-2 resonance (Fig. 15), yet its characteristic shape is nearly independent of these parameters. Note that the parameter choice $f_1 = f_2 = f_5 = 1$ resembles the electroweak part of the graviton scenario, but cannot reproduce SM Higgs cross sections, in contrast to our usual choice. As shown on the right hand side of Fig. 15, the $\Delta\Phi_{jj}$ distribution of the spin-2 triplet resonance with default couplings resembles the corresponding singlet case. In fact, this is the case for all distributions considered here. Even without the formfactor, the spin-2 $\Delta\Phi_{jj}$ distribution keeps its characteristic shape. By contrast, the spin-0 distribution is very model dependent: anomalous HVV couplings (Eq. (3.16)) strongly alter the $\Delta\Phi_{jj}$ distribution [73]. Furthermore, the SM Higgs distribution depends on cuts, which is illustrated in Fig. 14 for the ZZ channel. For more stringent lepton p_T cuts, e.g. $p_{T,l} > 20\,\text{GeV}$ instead of 7 GeV, the discriminating power gets worse. Also for WW (right hand side of Fig. 13), the $\Delta\Phi_{jj}$ distribution would be more central with e.g. $p_{T,l} > 20\,\text{GeV}$ instead of 10 GeV.
All in all, the $\Delta\Phi_{jj}$ distribution features a fundamental difference between a SM Higgs and a spin-2 resonance, which is nearly independent of the spin-2 model parameters, NLO QCD corrections and decay modes. This is why the azimuthal angle difference between the two tagging jets is such an important observable to distinguish between spin-0 and spin-2 in VBF.

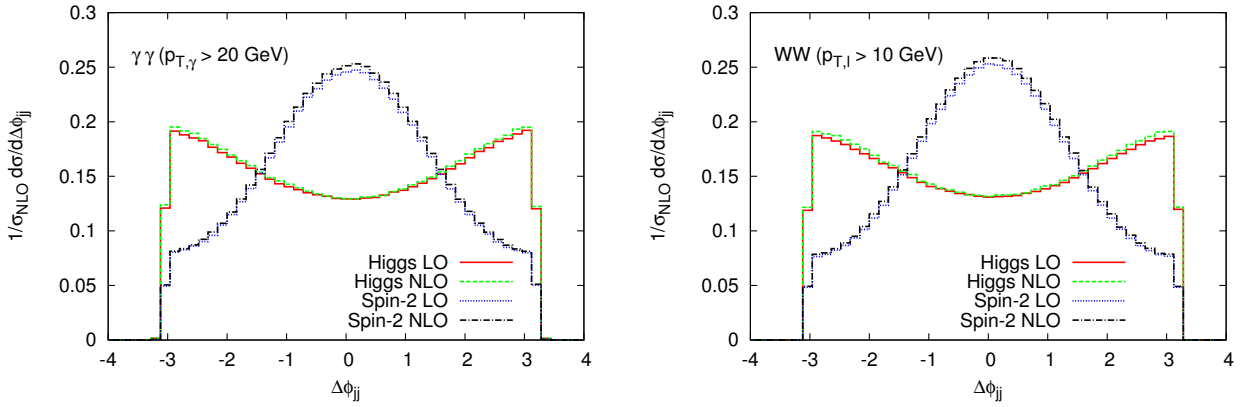

Figure 13: Azimuthal angle difference between the two tagging jets for a Higgs and for a spin-2 singlet resonance with couplings $f_1 = 0.04, f_2 = 0.08, f_5 = 10$, both at LO and NLO QCD accuracy. Left hand side: VBF $\gamma\gamma$, right hand side: VBF $WW \to e^+ \nu_e \mu^- \overline{\nu}_\mu$.

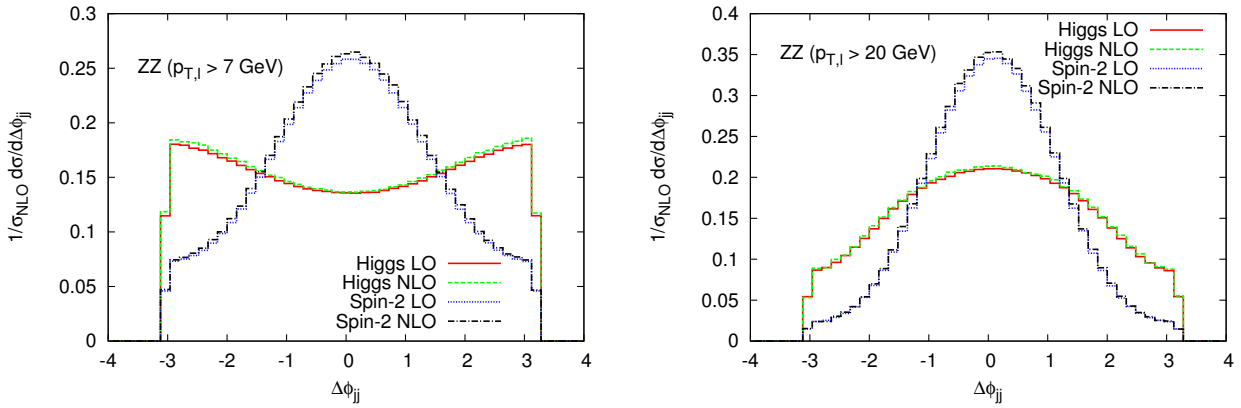

Figure 14: Azimuthal angle difference between the two tagging jets for a Higgs and for a spin-2 singlet resonance with couplings $f_1 = 0.04, f_2 = 0.08, f_5 = 10$, both at LO and NLO QCD accuracy. VBF $ZZ \to e^+ e^- \mu^+ \mu^-$ for different lepton p_T cuts.

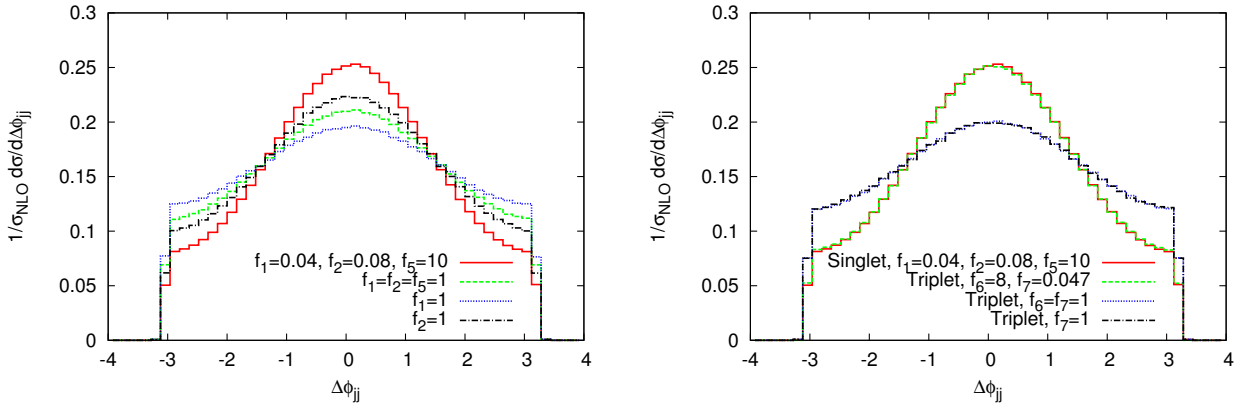

Figure 15: Azimuthal angle difference between the two tagging jets in VBF $\gamma\gamma$ for a spin-2 resonance with different coupling parameters at NLO QCD accuracy. Left hand side: spin-2 singlet, right hand side: spin-2 singlet and triplet.

In addition to jet distributions, which have similar features for different decay modes, we will analyze specific observables for the decay products in the different channels in the following.

3.3.3 Further relevant distributions in the diphoton channel

In the diphoton decay mode, an interesting variable for a spin determination in VBF is the angle Θ between the momentum of an initial electroweak boson and an outgoing photon in the rest frame of the resonance. Since the dependence of the matrix element on Θ is described by Wigner d-functions $d^j_{m,m'}(\Theta)$, even for off-shell initial bosons [18], the $\cos\Theta$ distribution should be an indicator of the spin of the resonance. In order to make this variable accessible not only in Monte Carlo studies, but also experimentally, the momenta of the initial electroweak bosons are reconstructed from those of the final-state photons and jets here. In particular, the jets are assigned to the initial quarks according to their rapidities, assuming that mainly forward scattering takes place.
Another, closely related, observable is the cosine of the Gottfried–Jackson angle, which is the angle between the momentum of the spin-2 particle or the Higgs boson in the laboratory frame and a final-state photon in the rest frame of the resonance. Both distributions are nearly independent of the NLO corrections and offer a difference between a SM Higgs and a spin-2 resonance (Fig. 16). The dependence on the spin-2 parameters is again weak, which is exemplified in Fig. 17 for the Gottfried–Jackson angle and is also true for the $\cos\Theta$ distribution. As mentioned before, the spin-2 singlet and triplet scenario with default couplings are indistinguishable. There are also other angular observables with very

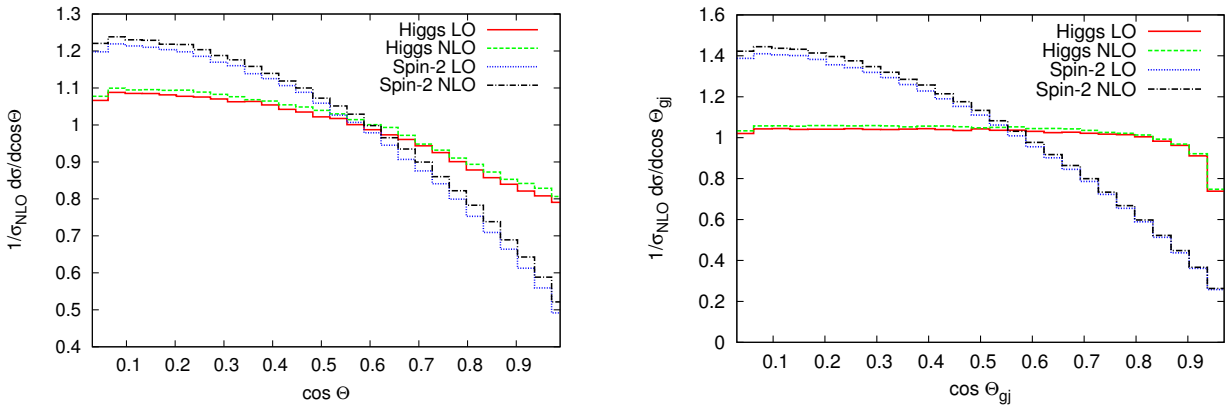

Figure 16: Angular distributions in the VBF $\gamma\gamma$ channel for a Higgs and for a spin-2 singlet resonance with couplings $f_1 = 0.04, f_2 = 0.08, f_5 = 10$, both at LO and NLO QCD accuracy. Left hand side: $\cos\Theta$, right hand side: cosine of the Gottfried–Jackson angle (see text for details).

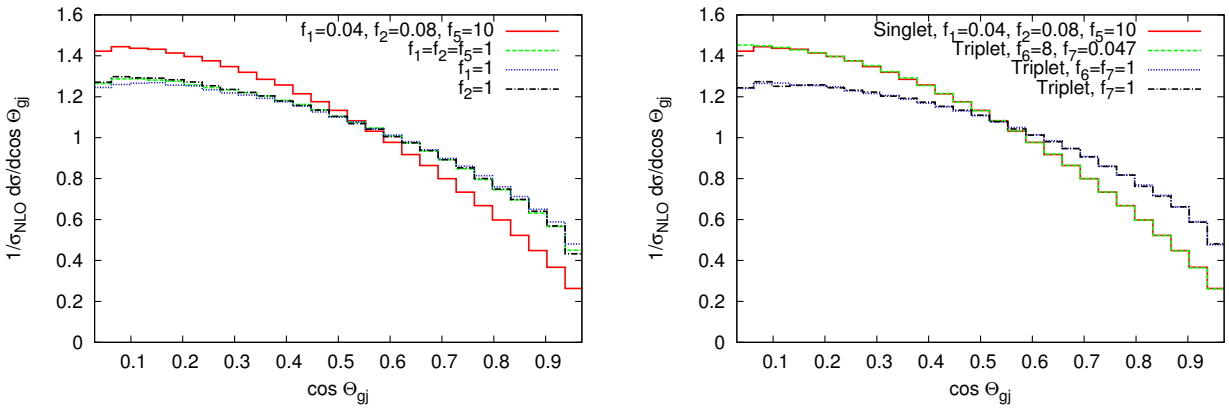

Figure 17: Cosine of the Gottfried–Jackson angle in VBF $\gamma\gamma$ for a spin-2 resonance with different coupling parameters at NLO QCD accuracy. Left hand side: spin-2 singlet, right hand side: spin-2 singlet and triplet.

similar characteristics, like the angle between a final-state photon and a tagging jet in the rest frame of the resonance.

In contrast, the azimuthal angle difference between the two final-state photons differs not only between a SM Higgs and a spin-2 resonance (left hand side of Fig. 18), but also between different spin-2 couplings (right hand side of Fig. 18). Therefore, the $\Delta\Phi_{\gamma\gamma}$ distribution is not sufficient for a spin-determination but, together with other distributions, it can provide useful information about a potential spin-2 resonance and its parameters.

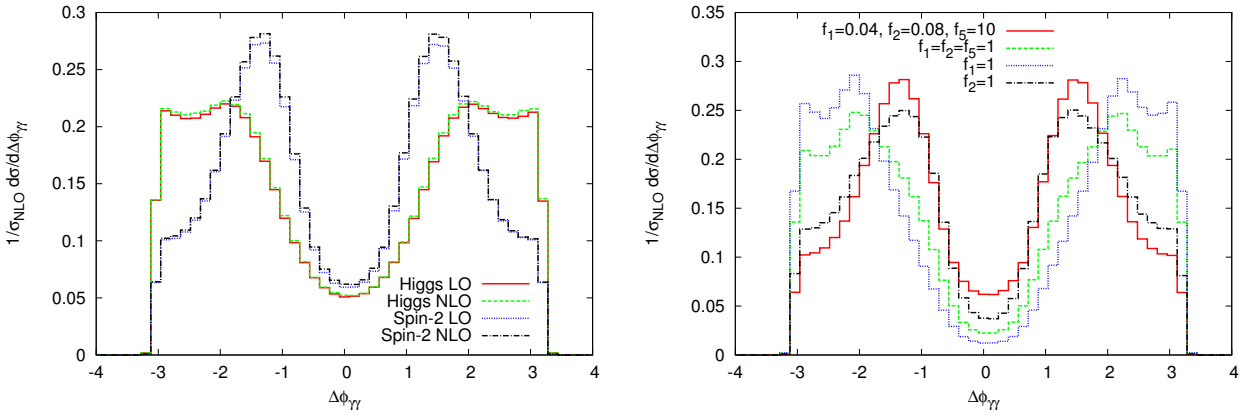

Figure 18: Azimuthal angle difference between the two final-state photons. Left hand side: SM Higgs and spin-2 singlet resonance with couplings $f_1 = 0.04, f_2 = 0.08, f_5 = 10$ at LO and NLO QCD accuracy, right hand side: spin-2 singlet resonance with different coupling parameters.

3.3.4 Lepton correlations in $W^+W^- \to 2l2\nu$

In the $W^+W^- \to l^+\nu l^-\bar{\nu}$ decay channel, the invariant mass of the two charged leptons is an important variable which is known to be an indicator of the spin [20, 21]. This can be understood from simple theoretical arguments [4], as illustrated in Fig. 19: For a spin-0 resonance, the spins of the two W bosons – and therefore also those of the two charged leptons – must be antiparallel. Because of the lepton helicities, this leads to parallel momenta of the two charged leptons and therefore to a small invariant dilepton mass $m_{ll} = \sqrt{(E_{l_1} + E_{l_2})^2 - (\boldsymbol{p}_{l_1} + \boldsymbol{p}_{l_2})^2}$. Contrarily, in the spin-2 case, the spins of the W bosons can be parallel, leading to antiparallel lepton momenta and a large invariant dilepton mass. This feature is demonstrated in Fig. 20, which shows that the invariant dilepton mass is much larger for a spin-2 resonance than for a SM Higgs boson and nearly independent of the spin-2 coupling parameters and the NLO QCD corrections. Note that these distributions include a cut of $m_{ll} > 15\,\text{GeV}$ (see Sec. 3.2.4). In the WW mode, we do not have to consider as many different spin-2 parameter choices as in the other channels, since the singlet coupling f_1 and the triplet coupling f_7 do not contribute to the TWW vertex (see (3.9), (3.12)).

The different lepton correlations also affect the azimuthal angle difference of the two charged leptons, which will be discussed for gluon fusion in Sec. 3.4.1, since the effect is more prominent there. Furthermore, the transverse mass, which is another related observable, will be studied there. The corresponding distribution (Fig. 24) looks similar in case of vector-boson fusion. However, the gluon-fusion process is much better accessible

[4] In case of spin-0, see also Ref. [98]

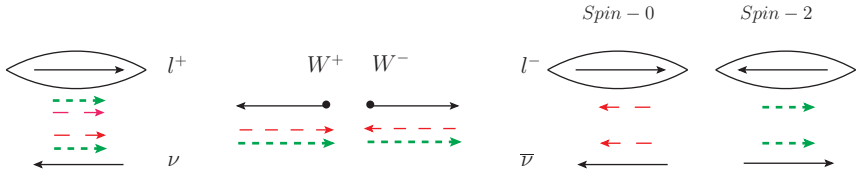

Figure 19: Illustration of lepton correlations in the decay of spin-0 or spin-2 resonances to $W^+W^- \to l^+\nu l^-\bar{\nu}$ in the rest frame of the resonance. Solid lines indicate the momenta, dashed lines the spins of the particles, which are red for spin-0 and green for spin-2. The momenta of the two charged leptons are encircled for both cases.

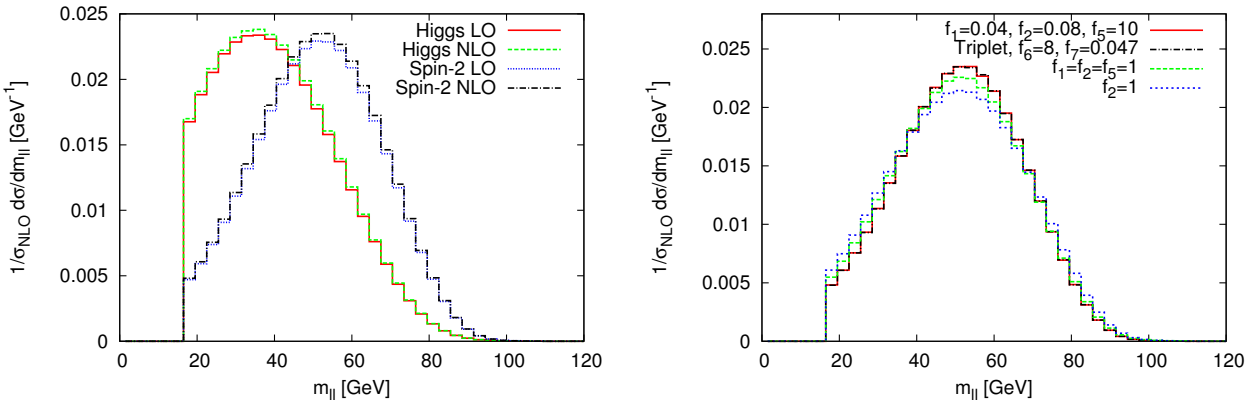

Figure 20: Invariant mass of the two charged leptons for $W^+W^- \to e^+\,\nu_e\,\mu^-\,\overline{\nu}_\mu$ in the VBF mode. Left hand side: SM Higgs and spin-2 resonance with couplings $f_1 = 0.04, f_2 = 0.08, f_5 = 10$, both at LO and NLO QCD accuracy; right hand side: spin-2 singlet or triplet resonance with different coupling parameters at NLO QCD accuracy.

experimentally and therefore better suited for such spin analyses.

For a spin determination in the $ZZ \to 4l$ channel, it is even more important to study the gluon-fusion production mode rather than VBF, since the VBF mode with a cross section of only around 10 ab (see Table 1) is very difficult to observe. Therefore, we will now discuss gluon fusion and perform further detailed spin studies in the ZZ channel in Section 3.4.4.

3.4 Gluon Fusion

In this section, spin-0 and spin-2 resonances produced in gluon fusion are studied for $\gamma\gamma$, $W^+W^- \to 2l2\nu$ and $ZZ \to 4l$ decays (see also Ref. [26]). The channel $Z\gamma \to l^+l^-\gamma$ will be included in Section 3.4.3. After comparing the rates of a SM Higgs and a spin-2 resonance, we present differential distributions which can be useful for a spin determination and study

Final State	Production mode	Higgs cross sec. [fb]	Spin-2 cross sec. [fb]
$\gamma\gamma$	VBF	0.745	0.864
	Gluon Fusion	37.1	35.7
$W^+W^- \to$ $e^+\,\nu_e\,\mu^-\,\overline{\nu}_\mu$	VBF	0.662	0.613
	Gluon Fusion	30.1	29.6
$ZZ \to$ $e^+\,e^-\,\mu^+\mu^-$	VBF	$1.06 \cdot 10^{-2}$	$0.982 \cdot 10^{-2}$
	Gluon Fusion	0.468	0.446

Table 3: Integrated cross sections for a SM Higgs and a spin-2 singlet resonance with couplings $f_1 = 0.04, f_2 = 0.08, f_5 = 10, f_9 = 0.04$ in VBF and gluon fusion (see text for details). The cuts of Section 3.2.4 are applied. Statistical errors from the Monte Carlo integration are less than one per mill.

the impact of spin-0 and spin-2 model parameters. Again, the mass of the Higgs boson and the spin-2 particle is set to 126 GeV and we assume pp collisions at a centre of mass energy of 8 TeV. Since in contrast to the spin-2 singlet case (3.9), the triplet model (3.12) does not provide a coupling to gluons, we only consider spin-2 singlet resonances here. To this end, we set the gluon coupling to $f_9 = 0.04$, while keeping the other couplings $f_1 = 0.04, f_2 = 0.08, f_5 = 10$ and the formfactor parameters $\Lambda_{ff} = 400\,\text{GeV}$, $n_{ff} = 3$ as in the last section. Since the non-vanishing gluon coupling induces an additional contribution to the spin-2 decay width, the overall energy scale Λ is rescaled to $\Lambda = 6.4\,\text{TeV}$ in order to compensate this effect on VBF cross sections. Indeed, with this parameter choice, the cross sections of all the decay modes considered here closely resemble those of a SM Higgs boson in gluon fusion and VBF simultaneously [5]. This is demonstrated in Table 3, where cross sections are presented at NLO QCD accuracy for VBF and account for higher-order QCD corrections in gluon fusion as described in Sec. 3.2. The effect of the minor coupling change on the phenomenology of spin-2 resonances in VBF is insignificant and the shapes of the distributions shown in Sec. 3.3 are not modified.

3.4.1 Leptonic observables in $W^+W^- \to 2l2\nu$

In order to distinguish spin-0 and spin-2 resonances produced in gluon fusion, the same differential distributions as in vector-boson fusion can be studied, apart from observables involving tagging jets, which do not exist here. In addition to the discussion of different spin-2 model parameters, we will also study the impact of alternative spin-0 scenarios in gluon fusion. Note that gluon-fusion distributions are determined at LO QCD and include a normalization factor $1/\sigma_{\text{LO}}$.

[5] Current LHC data suggest a slightly lower rate in WW and a somewhat higher one in $\gamma\gamma$, particularly in VBF [3, 11].

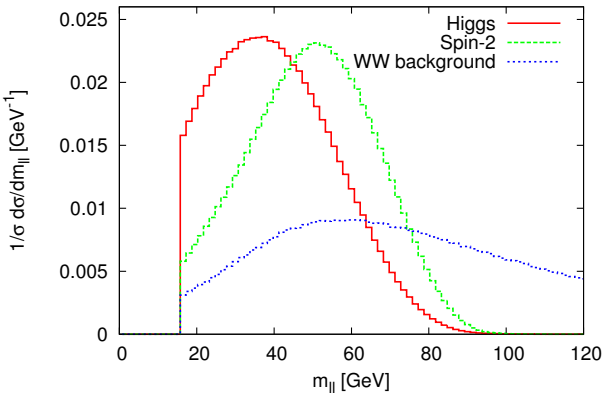

Figure 21: Normalized distribution of the invariant dilepton mass for $gg \to W^+W^- \to e^+\,\nu_e\,\mu^-\,\overline{\nu}_\mu$ for a SM Higgs and a spin-2 resonance with couplings $f_1 = 0.04, f_2 = 0.08, f_5 = 10, f_9 = 0.04$ at LO QCD accuracy and the diboson-production background including $q\bar{q} \to WW$ at NLO QCD plus the continuum production diagrams of $gg \to WW$. The cuts of Section 3.2.4 are applied.

In the WW decay channel, the invariant dilepton mass was found to be an important indicator of the spin. The same characteristic difference between a Higgs and a spin-2 resonance found in VBF (Sec. 3.3.4) also arises in the gluon-fusion mode, which is depicted in Fig. 21. This figure additionally shows the normalized diboson-production background for comparison, including $q\bar{q} \to W^+W^- \to e^+\,\nu_e\,\mu^-\,\overline{\nu}_\mu$ at NLO QCD accuracy and loop-induced $gg \to W^+W^- \to e^+\,\nu_e\,\mu^-\,\overline{\nu}_\mu$ fermion-box contributions. With an inclusive cross section of around 400 fb, this background exceeds the one of a Higgs or spin-2 resonance significantly, even after placing more stringent search cuts. Since the maximum of the invariant-dilepton-mass distribution is nearly at the same position for the spin-2 signal and the diboson continuum, a precise knowledge of the background is necessary. In Fig. 22, the model dependence of the invariant-dilepton-mass distribution is illustrated for the spin-0 and spin-2 cases. As in the VBF mode (Fig. 20), this observable is nearly independent of the spin-2 coupling parameters, whereas anomalous Higgs couplings can have a certain effect. Since only the HWW couplings are relevant for the process $gg \to W^+W^-$, we only consider the first two terms of the Lagrangian (3.16) and neglect the formfactor. While the $\mathcal{CP}$-even coupling g_{5e}^{HWW} alone or the mixed case $g_{5e}^{HWW} = g_{5o}^{HWW}$ tend to shift the distribution to smaller values of m_{ll}, which facilitates the spin determination, the m_{ll} distribution of a $\mathcal{CP}$-odd Higgs with g_{5o}^{HWW} is more similar to the one of a spin-2 resonance. This demonstrates that it is important to carefully disentangle spin and $\mathcal{CP}$ properties of the resonance.

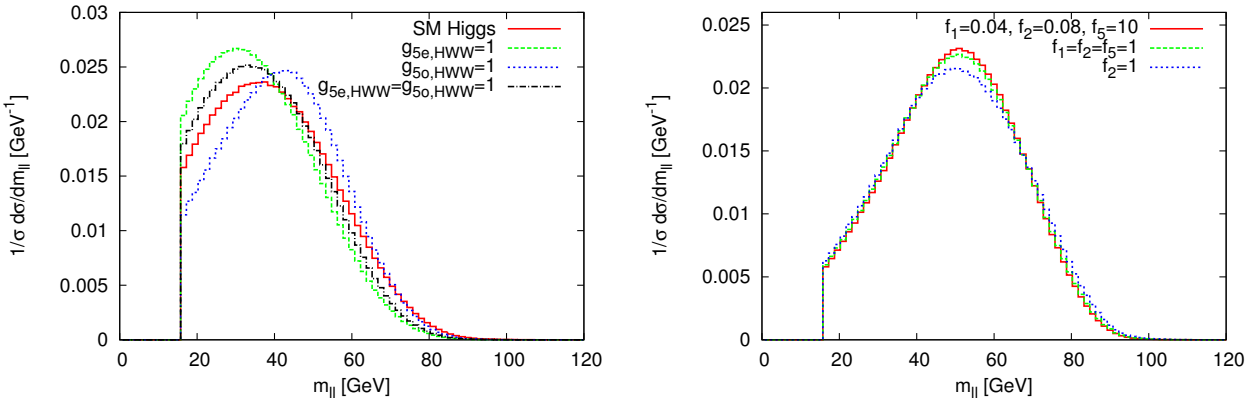

Figure 22: Spin-0 and spin-2 model dependence of the invariant dilepton mass in $gg \to W^+W^- \to e^+\,\nu_e\,\mu^-\,\overline{\nu}_\mu$. Left hand side: Higgs resonance with SM couplings, $\mathcal{CP}$-even and $\mathcal{CP}$-odd anomalous couplings; right hand side: spin-2 resonance with different coupling parameters (always including $f_9 = 0.04$).

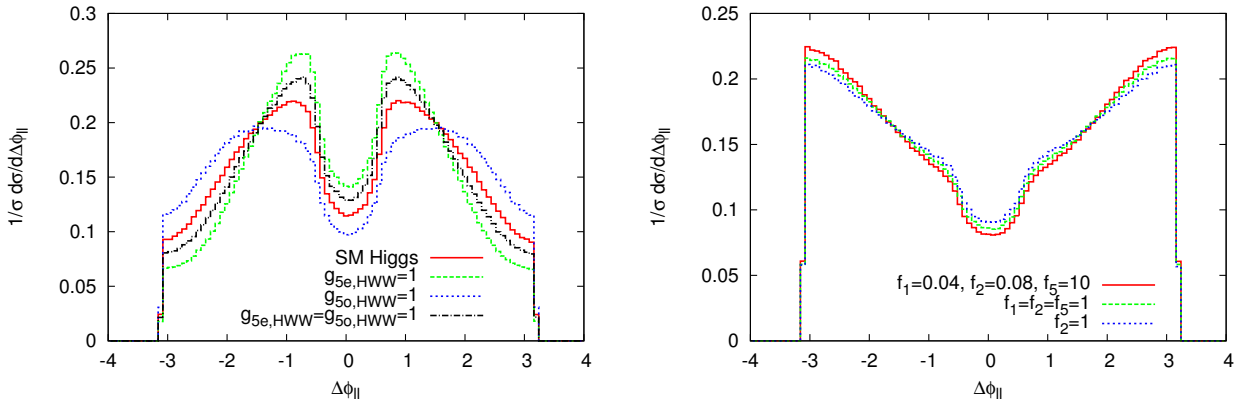

Figure 23: Azimuthal angle difference of the charged final-state leptons in $gg \to W^+W^- \to e^+\,\nu_e\,\mu^-\,\overline{\nu}_\mu$. Left hand side: Higgs resonance with SM couplings, $\mathcal{CP}$-even and $\mathcal{CP}$-odd anomalous couplings; right hand side: spin-2 resonance with different coupling parameters (always including $f_9 = 0.04$).

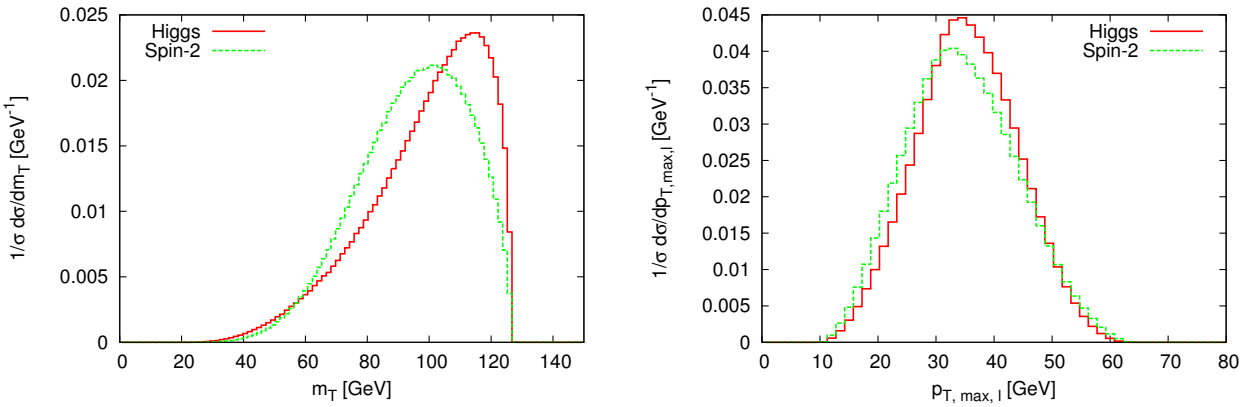

Figure 24: Differential distributions for a SM Higgs and a spin-2 resonance with couplings $f_1 = 0.04, f_2 = 0.08, f_5 = 10, f_9 = 0.04$ in $gg \to W^+W^- \to e^+\,\nu_e\,\mu^-\,\bar{\nu}_\mu$. Left hand side: transverse mass; right hand side: transverse momentum of the of the hardest final-state lepton.

Corresponding to a large (small) invariant dilepton mass, the azimuthal angle difference of the charged final-state leptons is also large (small) for a spin-2 (spin-0) resonance (Fig. 23). Also the model dependence shows the same behavior.

The different lepton correlations of spin-0 and spin-2 resonances also influence the transverse mass, which is an important experimental observable in processes involving neutrinos, where the resonance cannot be reconstructed in the full invariant-mass spectrum. In this process, it can be defined as [74, 99]:

$$m_T = \sqrt{(E_{T,ll} + E_{T,\text{miss}})^2 - (\boldsymbol{p}_{T,ll} + \boldsymbol{p}_{T,\text{miss}})^2}, \tag{3.36}$$

with

$$E_{T,ll} = \sqrt{\boldsymbol{p}_{T,ll}^2 + m_{ll}^2}\ , \quad E_{T,\text{miss}} = \sqrt{\boldsymbol{p}_{T,\text{miss}}^2 + m_{\nu\nu}^2} \to |\boldsymbol{p}_{T,\text{miss}}|. \tag{3.37}$$

Here, $E_{T,ll}$ and $\boldsymbol{p}_{T,ll}$ denote the transverse energy and momentum of the two charged leptons and $E_{T,\text{miss}}$ and $\boldsymbol{p}_{T,\text{miss}}$ those of the two neutrinos. Similar to the invariant mass of the two charged leptons, also the invariant mass of the two neutrinos, $m_{\nu\nu}$, is larger for spin-2 than for spin-0 (which can be observed in Monte Carlo, but not experimentally). Therefore, a larger fraction of $E_{T,\text{miss}}$ is omitted in the transverse mass in case of spin-2, which leads to smaller values of m_T than in case of spin-0. This feature is demonstrated on the left hand side of Fig. 24. However, the transverse mass could also be defined with an alternative approximation of $E_{T,\text{miss}}$, namely $E_{T,\text{miss}} = \sqrt{\boldsymbol{p}_{T,\text{miss}}^2 + m_{\nu\nu}^2} \to \sqrt{\boldsymbol{p}_{T,\text{miss}}^2 + m_{ll}^2}$. In this case, the difference between spin-0 and spin-2 decreases significantly, with both distributions reaching their maximal value around the mass of the resonance. The right

hand side of Fig. 24 shows that the transverse momentum of a final-state lepton is similar for a Higgs and a spin-2 resonance with default parameters. Both distributions of Fig. 24 hardly depend on spin-0 and spin-2 model parameters.

3.4.2 Spin determination in $gg \to \gamma\gamma$

In the process $gg \to \gamma\gamma$, there are only two (identical) final-state particles and therefore not as many different observables as in other processes studied before. However, the scattering angle, defined in some suitable reference frame, was theoretically found to be sensitive to the spin of the resonance [23] and indeed turned out to be very important for experimental Higgs spin analyses at CMS [12] and ATLAS [6]. There, the cosine of the photon angle in the Collins–Soper frame [100], $\cos\Theta_{CS}$, was used, which is defined as [6]:

$$\cos\Theta_{CS} = \frac{\sinh\left(\eta_{\gamma_1} - \eta_{\gamma_2}\right)}{\sqrt{1 + \left(p_{T_{\gamma\gamma}}/m_{\gamma\gamma}\right)^2}} \cdot \frac{2 p_{T_{\gamma 1}} p_{T_{\gamma 2}}}{m_{\gamma\gamma}^2}, \tag{3.38}$$

with $p_{T_{\gamma\gamma}}$ being the transverse momentum of the diphoton system.

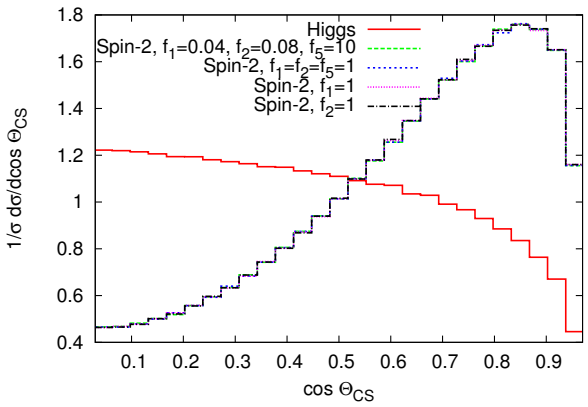

Figure 25: Cosine of the photon angle in the Collins–Soper frame in $gg \to \gamma\gamma$ for a SM Higgs and a spin-2 resonance with different coupling parameters (always including $f_9 = 0.04$).

The corresponding distribution within our model is presented in Fig. 25. It features a sizable difference between a SM Higgs and a spin-2 resonance and does not depend on the spin-2 couplings at all, since there is only one possible tensor structure for the Tgg and the $T\gamma\gamma$ vertex (see 3.9). However, this can change considerably when higher-dimensional spin-2 structures are included, which we will discuss in Sec. 3.5.

In gluon fusion, the photon angle in the Collins–Soper frame is equal to the Gottfried–

Jackson angle, which was studied in Sec. 3.3.3. In VBF however, this is not the case. There, the separation power of $\cos\Theta_{CS}$ is weaker than the one of the cosine of the Gottfried–Jackson angle (Fig. 16), so we did not consider this observable there.

3.4.3 Including the decay channel $Z\gamma \to l^+l^-\gamma$

In order to complete the set of decay channels which involve the spin-2 vertices (3.9) and are accessible at the LHC, the (Higgs or spin-2 resonant) process $gg \to Z\gamma \to l^+l^-\gamma$ is considered in the following. Here, intermediate photons decaying to l^+l^- instead of Z bosons are also included. Although $Z\gamma$ is not among the most relevant Higgs analysis channels at the LHC because of its small branching fraction, Higgs searches are performed in this channel as well [101, 102], since it can provide information about the loop-induced $H\gamma Z$ coupling and its possible BSM effects.
With the spin-2 coupling parameters of Sec.3.4, $f_1 = 0.04, f_2 = 0.08, f_5 = 10, f_9 = 0.04$, which reproduce SM Higgs cross sections in the $\gamma\gamma$, WW and ZZ modes (see Table 3), the cross section in $gg \to Z\gamma \to e^+e^-\gamma$ is 0.143 fb, which is much lower than the one of the SM Higgs boson (0.771 fb). Enhancing the spin-2 cross section in this channel without changing the others too much is possible by enhancing the difference of f_1 and f_2, since the Feynman rule of the $T\gamma Z$ vertex is governed by $f_2 - f_1$ (3.9). With the parameter choice $f_1 = 0.01, f_2 = 0.2, f_5 = 10, f_9 = 0.04$ (and $\Lambda = 6.4\,\text{TeV}$, $\Lambda_{ff} = 400\,\text{GeV}$, $n_{ff} = 3$ unchanged), all Higgs cross sections in this enlarged set of processes can be roughly reproduced simultaneously (Table 4). The shapes of differential distributions shown before are not modified by this change of the couplings.
Furthermore, this parameter choice leads to the same ratio of intermediate $Z\gamma$ and $\gamma\gamma$ contributions, which is visible in the invariant-mass spectrum of the two final-state leptons (left hand side of Fig. 26). There, the peak at $m_Z \approx 91$ GeV indicates leptons originating from a Z boson, while the rest stems from an intermediate photon. For $f_1 = 0.04, f_2 = 0.08, f_5 = 10, f_9 = 0.04$, not only the cross section, but also the relative $Z\gamma$ contribution is smaller than in case of the SM Higgs boson. The choice $f_1 = f_2 = f_5 = 1, f_9 = 0.04$ leads to a complete suppression of $Z\gamma$, since $f_2 - f_1$ is zero. Nevertheless, with 1.13 fb, the integrated cross section is even larger than the one of the Higgs, since the $\gamma\gamma$ contribution, which is governed by the value of f_1, is strongly enhanced. However, this cross section will be reduced significantly if a cut on the invariant dilepton mass, e.g. $m_{ll} > 50\,\text{GeV}$, is applied, which is done by CMS [101] in order to remove the $\gamma\gamma$ contribution. Differential distributions, like the azimuthal angle difference of the two leptons (right hand side of Fig. 26) and the transverse momentum of a final-state lepton or photon (Fig. 27),

Final State	Production mode	Higgs cross sec. [fb]	Spin-2 cross sec. [fb]
$\gamma\gamma$	VBF	0.745	0.996
	Gluon Fusion	37.1	37.7
$W^+W^- \to$ $e^+\,\nu_e\,\mu^-\,\overline{\nu}_\mu$	VBF	0.662	0.589
	Gluon Fusion	30.1	27.6
$ZZ \to$ $e^+\,e^-\,\mu^+\mu^-$	VBF	$1.06 \cdot 10^{-2}$	$0.933 \cdot 10^{-2}$
	Gluon Fusion	0.468	0.412
$Z\gamma \to e^+e^-\gamma$	Gluon Fusion	0.771	0.743

Table 4: Integrated cross sections for a SM Higgs and a spin-2 singlet resonance with couplings $f_1 = 0.01, f_2 = 0.2, f_5 = 10, f_9 = 0.04$ in VBF and gluon fusion, including the channel $gg \to Z\gamma \to l^+l^-\gamma$ (see text for details). The cuts of Section 3.2.4 are applied. Statistical errors from the Monte Carlo integration are less than one per mill.

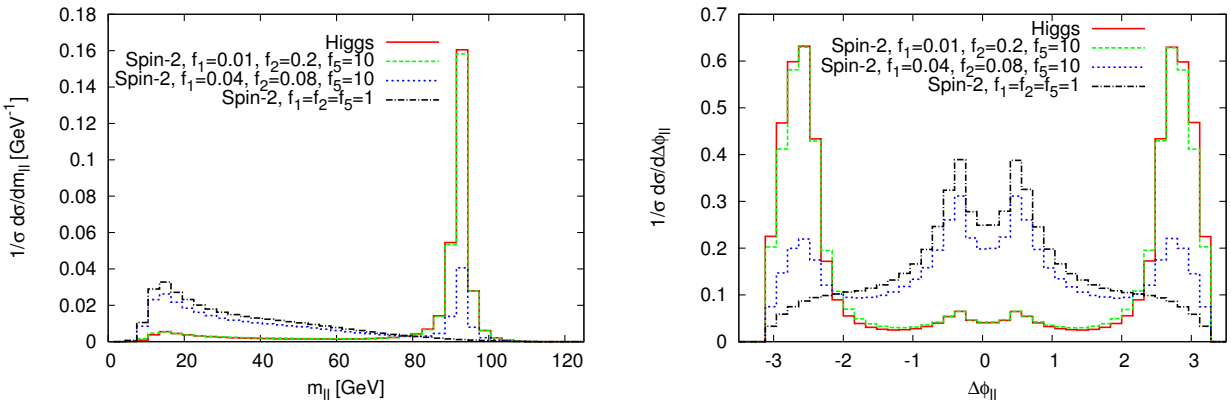

Figure 26: $gg \to e^+e^-\gamma$, SM Higgs and spin-2 resonance with different coupling parameters (always including $f_9 = 0.04$). Left hand side: invariant dilepton mass, right hand side: azimuthal angle difference of the two leptons.

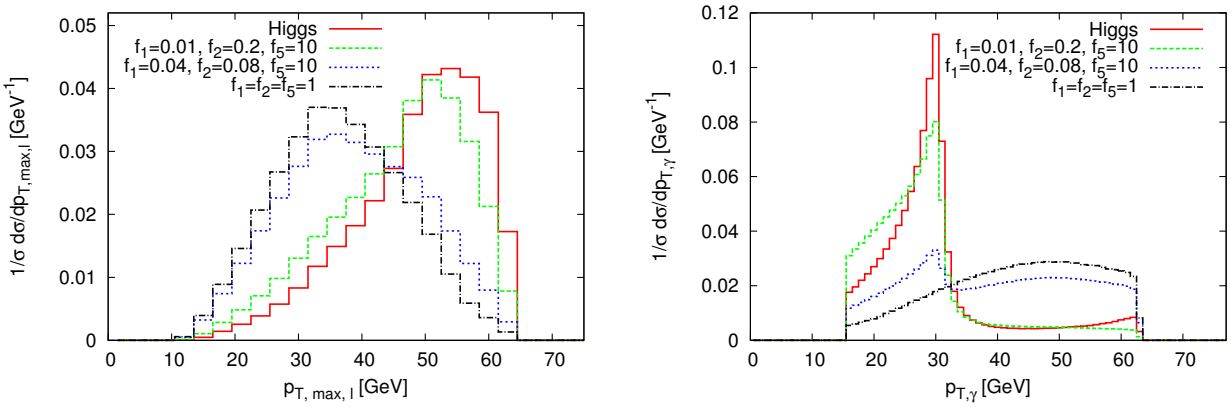

Figure 27: $gg \to e^+e^-\gamma$, SM Higgs and spin-2 resonance with different coupling parameters (always including $f_9 = 0.04$). Left hand side: transverse momentum of the hardest lepton, right hand side: transverse momentum of the final-state photon.

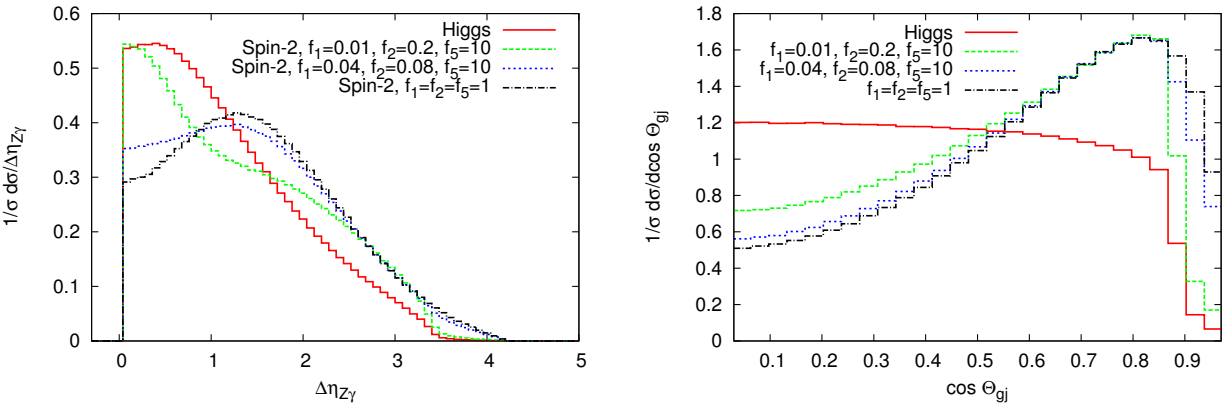

Figure 28: $gg \to e^+e^-\gamma$, SM Higgs and spin-2 resonance with different coupling parameters (always including $f_9 = 0.04$). Left hand side: pseudorapidity difference between the final-state photon and the intermediate Z boson (or photon), right hand side: cosine of the Gottfried–Jackson angle.

are strongly affected by different $Z\gamma/\gamma\gamma$ ratios. Although the pseudorapidity difference between the final-state photon and the intermediate Z boson (or photon) (left hand side of Fig. 28) suggests some additional information on the spin of the resonance, the only definite indicator of the spin is the (cosine of the) Gottfried–Jackson angle [6] (right hand side of Fig. 28). Independently of the spin-2 parameters, i.e. also of the $Z\gamma/\gamma\gamma$ ratio, this distribution clearly distinguishes between spin-0 and spin-2.

[6] In this case, the Gottfried–Jackson angle is defined as the angle between the momentum of the spin-2 particle or the Higgs boson in the laboratory frame and the final-state photon in the rest frame of the resonance, but the distribution looks the same if defined with the intermediate boson instead of the final-state photon.

3.4.4 $gg \to ZZ \to e^+ e^- \mu^+ \mu^-$

Finally, we will now discuss the decay to four leptons, which provides the largest set of potentially spin-sensitive observables among the considered gluon fusion channels. Again, intermediate photons decaying to lepton pairs instead of Z bosons are also included, leading to the different possible intermediate states ZZ, $Z\gamma$, γZ and $\gamma\gamma$. A set of angles which are known to be suited for analyzing a resonance decaying to two weak bosons are the Cabibbo-Maksymowicz-Dell'Aquila-Nelson angles [17, 103]. Furthermore, two invariant-mass distributions can be studied, which are those of lepton pairs having the same flavour and opposite charge [5, 9]. The distribution of the pair whose invariant mass is closer to the mass of the Z boson is denoted as m_{Z_1}, the other one as m_{Z_2}. The latter, as well as the invariant mass of the $e^+ e^-$ system, are presented in the figures 29 and 30 for a SM Higgs and a spin-2 singlet resonance with different coupling parameters. In case of the Higgs resonance, both peaks in $m_{e^+ e^-}$ (or those in m_{Z_1} and m_{Z_2}, respectively) originate from a Z boson, of which one is (nearly) on-shell and the second one far off-shell to account for the Higgs mass of 126 GeV. The same is true for a spin-2 resonance with $f_5 \gg f_1$, f_2, since in this case, the $T\gamma\gamma$ and $T\gamma Z$ vertex are suppressed (3.9), such that the contribution of two intermediate Z bosons dominates. For settings like $f_1 = f_2 = f_5 = 1$ or $f_1 = 1$, however, there is a substantial contribution of intermediate photons. Such a characteristic is analogous to the one observed in the channel $Z\gamma \to l^+ l^- \gamma$ (Sec. 3.4.3), which is simpler because it features only two different intermediate states, $Z\gamma$ and $\gamma\gamma$. There, we found that different spin-2 parameter choices can lead to substantially different distributions because of different amounts of intermediate photons or Z bosons. The same is true here, which is illustrated in Fig. 31 for two interesting angular distributions: the cosine of the Gottfried–Jackson angle, here defined as the angle between the momentum of the spin-2 particle or the Higgs boson in the laboratory frame and an intermediate photon or Z boson in the rest frame of the resonance, and $\cos\Theta_e$, which is the angle between the momentum of the positron and the intermediate boson which decays into $\mu^+\mu^-$ in the rest frame of the other intermediate boson, closely following the definition in Ref. [24]. In such distributions, the difference between different spin-2 settings (which feature different contributions of intermediate photons and Z bosons) is larger than between a Higgs and spin-2 resonance. Therefore, a spin determination in this channel is more intricate than in other channels like $\gamma\gamma$ or WW. However, the ZZ mode can be useful to distinguish between different spin-2 scenarios and to exclude some of them. In contrast to the $Z\gamma$ mode (see Fig. 26 and 27), the parameter choices $f_1 = 0.01, f_2 = 0.2, f_5 = 10$ and $f_1 = 0.04, f_2 = 0.08, f_5 = 10$ lead to similar distributions here. This is because for

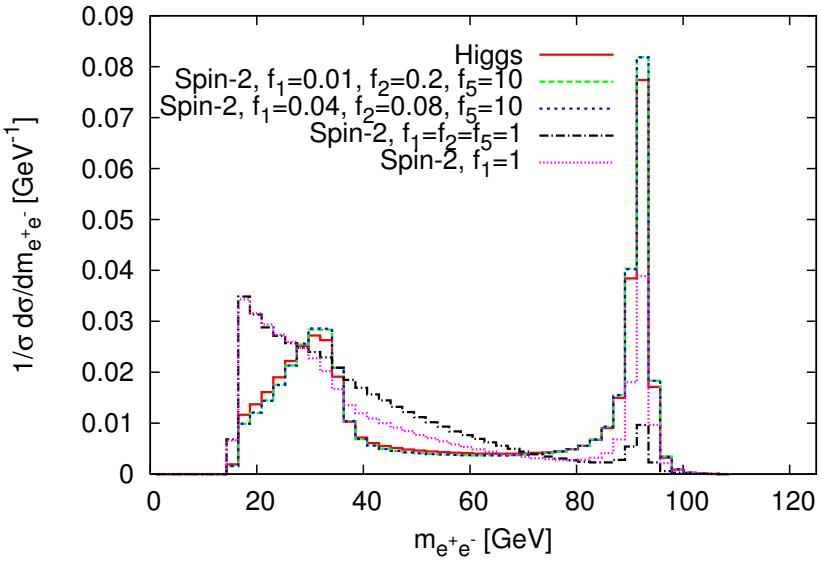

Figure 29: Invariant mass of the $e^+\,e^-$ system in $gg \to e^+\,e^-\,\mu^+\mu^-$ for a SM Higgs and a spin-2 resonance with different coupling parameters (always including $f_9 = 0.04$).

$f_5 \gg f_1$, f_2, the intermediate ZZ contribution, stemming from the TZZ vertex involving f_5, dominates in the four-lepton mode, while the $e^+e^-\gamma$ final state only involves the $T\gamma\gamma$ and $T\gamma Z$ vertex, where f_5 is absent and the relation between f_1 and f_2 is relevant (see (3.9)). Note that the cut imposed on the invariant mass of two oppositely charged leptons ($m_{ll} > 15$ GeV, see Sec. 3.2.4) does not influence the features of the distributions shown here. For a less stringent cut of e.g. $m_{ll} > 5$ GeV, they are not modified, in spite of the additional low invariant-mass contributions of different size.

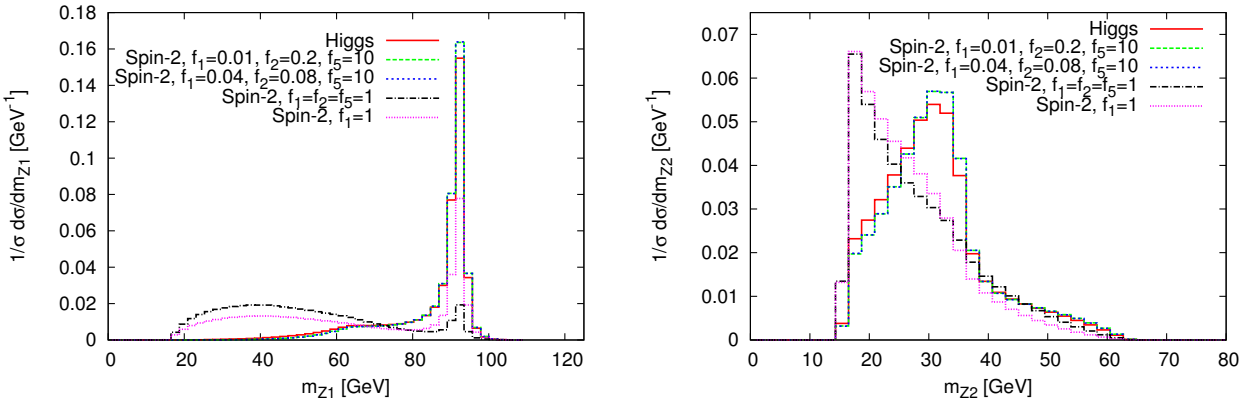

Figure 30: $gg \to e^+ e^- \mu^+ \mu^-$, SM Higgs and spin-2 resonance with different coupling parameters (always including $f_9 = 0.04$). Left hand side: invariant same-flavour dilepton mass closer to the Z boson mass, right hand side: other invariant same-flavour dilepton mass.

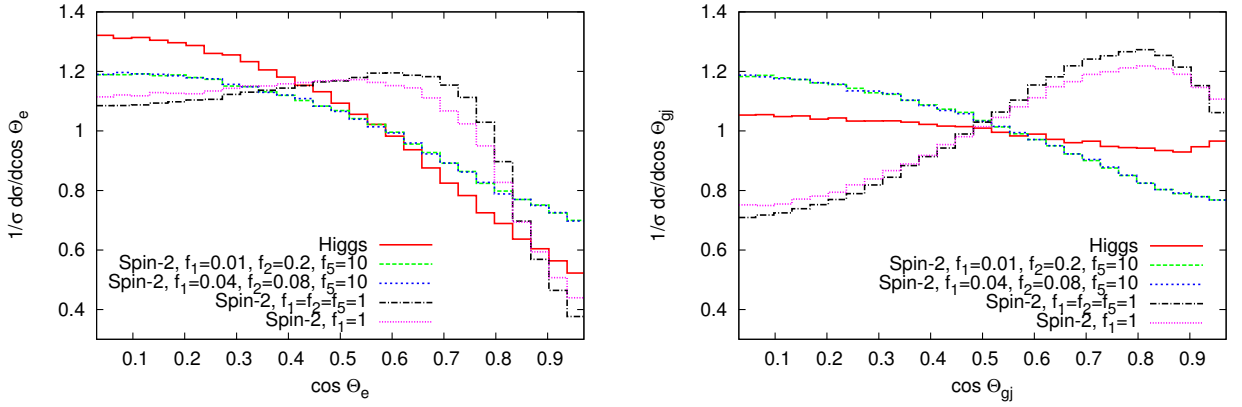

Figure 31: $gg \to e^+ e^- \mu^+ \mu^-$, SM Higgs and spin-2 resonance with different coupling parameters (always including $f_9 = 0.04$). Left hand side: $\cos\Theta_e$, right hand side: cosine of the Gottfried–Jackson angle (see text for details).

3.5 Higher-dimensional Spin-2 structures

So far, the properties of spin-2 particles and their distinction from a Higgs boson were studied in the framework of an effective Lagrangian, where only the lowest order of the expansion in inverse powers of the energy scale Λ was considered (see Sec. 3.1). In this framework, various characteristic differences between spin-0 and spin-2 arise, which allow for a Higgs spin determination rather independently of the spin-2 model parameters. However, since a definite spin determination requires the most general spin-2 parametrization, the effects of higher-dimensional spin-2 structures should also be studied. Even though they are expected to be suppressed by inverse powers of a high energy scale, they might alter differential distributions by their different kinematic structure. Since the most stringent exclusion limits of specific spin-2 models are currently extracted from the cosine of the photon angle in the Collins–Soper frame in the process $gg \to \gamma\gamma$ [4,6] (see Sec. 3.4.2), we will now exemplify the effects of higher-dimensional spin-2 terms in this process. While at lowest order it was convenient to construct the spin-2 Lagrangian and derive the Feynman rules from it, it is easier to find all possible independent terms which contribute to the spin-2 vertex $T\gamma\gamma$ in case of higher-dimensional structures. This can be achieved by means of the following considerations. Since terms in a spin-2 Lagrangian can only contain even numbers of field strength tensors and covariant derivatives, the corresponding vertex terms contain even numbers of photon momenta p_1 and p_2.[7] In case of $\mathcal{CP}$-even terms, the four indices α, β, μ, ν can be carried either by p_1, p_2 or metric tensors g^{μ_1,μ_2}. Several features of the spin-2 field significantly reduce the number of possible terms: Interchanging the indices μ and ν yields equivalent terms, since the spin-2 field $T^{\mu\nu}$ is symmetric. Terms containing a metric tensor $g^{\mu\nu}$ do not contribute due to $T^{\mu}_{\mu} = 0$. Furthermore, terms involving $p_1^{\mu}\, p_1^{\nu}$, $p_2^{\mu}\, p_2^{\nu}$ and $p_1^{\mu}\, p_2^{\nu}$ are related in case of a spin-2 resonance, since the spin-2 field is transverse. Additionally, various terms which could contribute to a spin-2 vertex with massive gauge bosons are not present in case of massless photons. In particular, expressions with p_1^2 or p_2^2 vanish for on-shell photons and current conservation eliminates terms comprising p_1^{α} or p_2^{β}. Gauge invariance, which is respected automatically if the Feynman rules are derived from a gauge invariant Lagrangian, can be incorporated in the vertex construction by imposing Ward identities, i.e. the vertex expression must vanish when contracted with $p_{1,\alpha}$ or $p_{2,\beta}$. This further restricts the number of independent terms. By constructing the complete set of vertex terms which comprise zero or two photon momenta and fulfill all these conditions, one obtains exactly the tensor structure

[7] As in Sec. 3.1, p_1 is the incoming four-momentum of the first photon with index α and p_2 the one of the second photon with index β.

$K_1^{\alpha\beta\mu\nu}$ (Eq. (3.10)) of the $T\gamma\gamma$ vertex (3.9) from the lowest order Lagrangian (3.6). This is a nice cross-check that both approaches are equivalent.
The next step is to include the vertex structures which contain four photon momenta. This corresponds to the next order in the expansion of an effective Lagrangian, which would contain terms with two field strength tensors and two covariant derivatives acting on them. By writing down all possible terms with free coefficients and imposing all the mentioned conditions, we end up with the following vertex:

$$T\gamma\gamma_{\text{ highdim}}: \ \frac{2i}{\Lambda}(f_1 c_w^2 + f_2 s_w^2) K_1^{\alpha\beta\mu\nu} + \frac{i}{\Lambda^3} K_3^{\alpha\beta\mu\nu}, \tag{3.39}$$

with the new higher-dimensional tensor structure

$$\begin{aligned} K_3^{\alpha\beta\mu\nu} &= d_1\,(p_1^\nu\, p_2^\mu\, g^{\alpha\beta}(p_1\cdot p_2) - p_1^\mu\, p_2^\nu\, p_1^\beta\, p_2^\alpha) \\ &\quad + d_2\,(p_1^\beta\, p_2^\nu\, g^{\alpha\mu}(p_1\cdot p_2) + p_2^\alpha\, p_1^\nu\, g^{\beta\mu}(p_1\cdot p_2) - g^{\alpha\nu} g^{\beta\mu}(p_1\cdot p_2)^2 - p_1^\mu\, p_2^\nu\, p_1^\beta\, p_2^\alpha), \end{aligned} \tag{3.40}$$

where d_1 and d_2 are free parameters. For on-shell spin-2 resonances, $p_1 \cdot p_2$ is equal to $\frac{1}{2}m_T^2$ and Eq. (3.40) can be rewritten as

$$\begin{aligned} K_3^{\alpha\beta\mu\nu} &= d_1\,(\frac{m_T^2}{2} K_{1,1}^{\alpha\beta\mu\nu} - p_1^\mu\, p_2^\nu\, p_1^\beta\, p_2^\alpha) \\ &\quad + d_2\,(-\frac{m_T^2}{2}(K_{1,2}^{\alpha\beta\mu\nu} + K_{1,3}^{\alpha\beta\mu\nu} + K_{1,4}^{\alpha\beta\mu\nu}) - p_1^\mu\, p_2^\nu\, p_1^\beta\, p_2^\alpha), \end{aligned} \tag{3.41}$$

where $K_{1,1(2...)}^{\alpha\beta\mu\nu}$ is the first (second ...) term in $K_1^{\alpha\beta\mu\nu}$ (see Eq. (3.10)). From this formulation, one can see that there is only one actually new higher-dimensional index structure, $p_1^\mu\, p_2^\nu\, p_1^\beta\, p_2^\alpha$, yet it has to be incorporated into a gauge invariant combination of other terms. A similar feature already arises in the lower-dimensional tensor structures (Eqs. (3.10), (3.11)), where $K_1^{\alpha\beta\mu\nu}$, which comprises the terms with two momenta, also involves the zero-momentum structure $K_2^{\alpha\beta\mu\nu}$ in a certain gauge invariant combination.
Terms of even higher dimension, i.e. terms with six or more momenta, cannot lead to additional new structures, since there are only four indices α, β, μ, ν, which means that at most four momenta can carry an index, while the others have to be contracted, which leads to combinations of existing structures with momentum-dependent factors. The $T\gamma\gamma$ vertex (3.39) agrees with alternative general formulations of spin-2 vertices [17,20] in case of $\mathcal{CP}$-even couplings to two photons.
Fig. 32 illustrates the phenomenological impact of the higher-dimensional $T\gamma\gamma$ structures (3.40) in the process $gg \to \gamma\gamma$. On the left hand side, the normalized LO differential

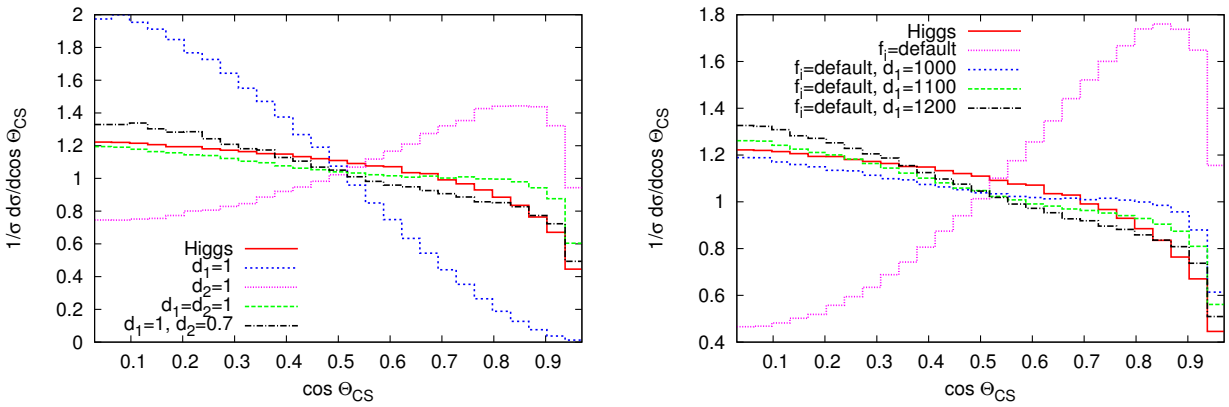

Figure 32: Influence of higher-dimensional spin-2 structures on the cosine of the photon angle in the Collins–Soper frame in $gg \to \gamma\gamma$, with $\Lambda = 6.4\,\text{TeV}$. Left hand side: spin-2 resonance with different higher-dimensional couplings (and Tgg coupling $f_9 = 0.04, f_{i\neq 9} = 0$), right hand side: combination of higher-dimensional couplings and default low-dimensional couplings ($f_1 = 0.04, f_2 = 0.08, f_5 = 10, f_9 = 0.04$).

distribution of the cosine of the photon angle in the Collins–Soper frame is depicted for different higher-dimensional couplings d_1 and d_2 and compared to the SM Higgs distribution. The gluon coupling is $f_9 = 0.04$ as before, since the Tgg vertex was not modified, yet all other low-dimensional couplings f_i are set to zero. Apart from that, the settings are the same as in Sec. 3.4. One can clearly see that the two different new structures with couplings d_1 and d_2 lead to very different, complementary distributions, so they can roughly mimic the SM Higgs distribution if combined properly. Since the d_1 structure also leads to a distribution which is opposite to the one of the low-dimensional couplings f_i (for the latter, see Fig. 25 and the purple line on the right hand side of Fig. 32), combinations of these two types of couplings can also lead to Higgs-like distributions, which is demonstrated on the right hand side of Fig. 32. These features also hold for other distributions in the $gg \to \gamma\gamma$ channel. For settings like $d_1 = 1200$, $f_1 = 0.04, f_2 = 0.08, f_5 = 10, f_9 = 0.04$, $\Lambda = 6.4$ TeV and the usual formfactor parameters, the cross section is roughly twice as large as the one of the SM Higgs, so the couplings would have to be rescaled appropriately to reproduce the rate measured at the LHC.

It could also be interesting to study whether such higher-dimensional structures alter important spin-discriminating distributions in other processes and whether there is still a set of couplings which can reproduce all the measured rates in all the channels. However, such an analysis is beyond the scope of this work, since it would require the knowledge of relations between all the higher-dimensional couplings in all TVV vertices, which would have to be derived from a full high-dimensional effective Lagrangian, where many orders

in the expansion in inverse powers of Λ have to be considered if Λ is rather small. Moreover, a ratio of the couplings d_1/f_i of order $\mathcal{O}(10^4)$ (required for a Higgs-like $\cos\Theta_{CS}$ distribution) seems quite unrealistic, although it would be smaller if the scale Λ would be lowered and the couplings rescaled appropriately, since these couplings are divided by different powers of a free parameter Λ. In fact, the relevant parameter is not d_1 alone, but $\frac{d_1 m_T^2}{\Lambda^2}$, as can be seen from Eqs. (3.39) and (3.41). From the latter, it also follows that the parameter choice $d_1 = -d_2$ reproduces $K_1^{\alpha\beta\mu\nu}$ in case of on-shell spin-2 resonances.

3.6 Conclusion and experimental status

In conclusion, cross sections alone cannot definitely exclude the spin-2 hypothesis for the newly discovered $125 - 126$ GeV resonance, since a spin-2 resonance can approximately reproduce SM Higgs rates in the considered channels in case of adjusted spin-2 couplings. In spite of many free model parameters, this result is non-trivial, as the electroweak spin-2 couplings are related by an $SU(2) \times U(1)$ gauge symmetry. Likewise, transverse-momentum distributions of a spin-2 resonance can be adjusted to those of a SM Higgs boson by tuning formfactor parameters. In contrast, various angular and invariant-mass distributions allow for a spin determination in the main detection channels $\gamma\gamma$, $W^+W^- \to 2l2\nu$ and $ZZ \to 4l$. Recently, the collaborations of the LHC experiments ATLAS and CMS have also performed analyses of some of these distributions in the same channels. Thereby, specific spin-2 scenarios could be excluded [4–7,9–12]. In this thesis, it was found that most of the distributions depend only little on spin-2 model parameters. Thus, such observables severely constrain the parameter space of spin-2 resonances, whereas experimental data obtained for the new particle are compatible with being the scalar Higgs boson of the Standard Model. Nevertheless, it is difficult to exclude all possible spin-2 models definitely, since in a framework beyond lowest order in an effective Lagrangian approach, there are many free parameters, which in certain combinations can mimic differential distributions of a SM Higgs resonance. These specific scenarios, however, are quite unrealistic within the effective spin-2 framework.

3.7 Heavy Spin-2 Resonances in Vector-boson Fusion

So far, light spin-2 resonances in the context of a Higgs spin determination were investigated. However, with the high energies which can be achieved with the LHC, it might also be possible to detect new, heavy resonances that are manifestations of physics beyond the Standard Model, which might also include a modified Higgs sector. For such resonances, a spin determination would also be needed. Whereas heavy spin-1 resonances have already been studied within the VBFNLO framework [30], we will analyze the characteristics of heavy spin-2 resonances in this section (see also Refs. [25, 69]). Here, the 126 GeV resonance studied previously is assumed to be the SM Higgs boson.[8] In this analysis, we consider different VBF processes with final states containing four leptons and two jets, namely $e^+ e^- \mu^+\mu^- jj$, $e^+ e^- \nu_\mu\overline{\nu}_\mu jj$, $e^+ \nu_e \mu^- \overline{\nu}_\mu jj$, $e^+ \nu_e \mu^+\mu^- jj$ and $e^- \overline{\nu}_e \mu^+\mu^- jj$. The electroweak continuum background from VBF within the SM is always included (see Sec. 3.2 for details). Since a resonance in the invariant-mass spectrum of the leptons can be exactly reconstructed if the final state does not contain a neutrino, we mainly focus on the $e^+ e^- \mu^+\mu^- jj$ mode to present the characteristic transverse-momentum and angular distributions of spin-2 resonances. Furthermore, cross sections of the different processes with and without spin-2 resonances are compared, the impact of NLO QCD corrections is studied and we investigate how the spin-2 singlet and triplet case, as well as different coupling parameters, can be distinguished from one another.

If not indicated otherwise, a spin-2 singlet resonance with $f_1 = f_2 = f_5 = 1$, $f_{i\neq 1,2,5} = 0$, and $\Lambda = 1.5\,\text{TeV}$ is considered. This choice of couplings resembles the electroweak part of a graviton scenario. The parameters of the formfactor are $\Lambda_{ff} = 3\,\text{TeV}$, $n_{ff} = 4$ and the mass is set to 1 TeV. For the triplet case, the same parameters are used, apart from the couplings, which are set to $f_6 = f_7 = 1, f_{i\neq 6,7} = 0$. In this section, a centre of mass energy of 14 TeV is assumed.

Table 5 gives an overview of the integrated cross sections for the different VBF processes with four final-state leptons with and without spin-2 resonances at LO and NLO QCD accuracy. For a given process, these cross sections correspond to a specific leptonic final state. The cross sections for all combinations of lepton generations together can be obtained by multiplying the given cross sections with an appropriate factor. For some final states, there is some interference between different processes, but this interference is negligible. One such example is $e^+ e^- \nu_e \overline{\nu}_e$, which can be produced both as $(e^+ e^-)\,(\nu_e \overline{\nu}_e)$ and

[8] In this section, the mass of the Higgs boson is set to 130 GeV, since this analysis was performed before the $125 - 126$ GeV resonance was discovered at the LHC, yet the results do not change for slightly different masses such as 126 GeV.

Final-state leptons	Scenario	LO cross section [fb]	NLO cross section [fb]
$e^+ e^- \mu^+\mu^-$	SM without spin-2	0.0520	0.0549
	Spin-2 singlet	0.0541	0.0567
	Spin-2 triplet	0.0523	0.0557
$e^+ e^- \nu_\mu\overline{\nu}_\mu$,	SM without spin-2	0.203	0.212
	Spin-2 singlet	0.215	0.226
	Spin-2 triplet	0.212	0.224
$e^+ \nu_e \mu^- \overline{\nu}_\mu$	SM without spin-2	2.207	2.278
	Spin-2 singlet	2.249	2.297
	Spin-2 triplet	2.200	2.267
$e^+ \nu_e \mu^+\mu^-$	SM without spin-2	0.1726	0.1795
	Spin-2 singlet	0.1720	0.1792
	Spin-2 triplet	0.1734	0.1805
$e^- \overline{\nu}_e \mu^+\mu^-$	SM without spin-2	0.0946	0.1001
	Spin-2 singlet	0.0943	0.1000
	Spin-2 triplet	0.0951	0.1005

Table 5: Integrated cross sections with and without spin-2 resonances at 1 TeV for different VBF processes with four leptons and two jets in the final state, at LO and NLO QCD accuracy, including the electroweak SM continuum background. The cuts of Section 3.2.4 are applied. The parameter settings of the spin-2 model can be found at the beginning of Section 3.7. Statistical errors from the Monte Carlo integration are at the half percent level.

as $(e^+\nu_e)\,(e^-\,\overline{\nu}_e)$, where the brackets group the fermions into pairs which are connected by a continuous fermion line. The first case leads to events with $m_{e^+e^-} \approx m_Z \approx m_{\nu_e\overline{\nu}_e}$, while the second case gives rise to $m_{e^+\nu_e} \approx m_W \approx m_{e^-\overline{\nu}_e}$. As in case of light, Higgs-like resonances (Sec. 3.3), the NLO QCD corrections are relatively small, with K-factors around 1.05. Spin-2 resonances lead to a relative enhancement of the cross section, which is larger for the $e^+ e^- \mu^+\mu^- jj$ and $e^+ e^- \nu_\mu\overline{\nu}_\mu jj$ channel than for the other processes, which means that the relative contribution of the continuum background is smaller for ZZ than for WW or WZ. For $pp \to e^+ \nu_e \mu^+\mu^- jj$ and $pp \to e^- \overline{\nu}_e \mu^+\mu^- jj$, there is no spin-2 singlet resonance, since only the charged resonances of the spin-2 triplet can be generated in these processes. The spin-2 triplet leads to a weaker enhancement than the singlet scenario throughout, corresponding to a narrower resonance (see Table 6). Although the effects of spin-2 resonances on the cross sections of Table 5 are small, they become much more significant when additional mass cuts around the resonance are imposed, which will be discussed below.

Spin-2 Resonance	Width [GeV]
Singlet, 500 GeV	0.982
Singlet, 750 GeV	3.238
Singlet, 1000 GeV	7.607
Singlet, 1250 GeV	14.795
Singlet, 1500 GeV	25.505
Triplet, 1000 GeV	1.004

Table 6: Total widths of the spin-2 resonances shown in Fig. 33.

3.7.1 $pp \to VV\,jj \to e^+\,e^-\,\mu^+\mu^-\,jj$

In the process $pp \to VV\,jj \to e^+\,e^-\,\mu^+\mu^-\,jj$, the invariant-mass spectrum of the four final-state leptons can be fully reconstructed experimentally, since there are no neutrinos in the final state. Fig. 33 shows different kinds of spin-2 resonances in this distribution. For the Standard Model, a Higgs resonance at 126 GeV is followed by the electroweak continuum which vanishes for high energies. The spin-2 singlet resonance peak is depicted for masses up to 1.5 TeV for the given parameter choice. The triplet case, which is analogous except for the height and width of the resonance, is exemplified for a mass of 1 TeV. In this process, the spin-2 triplet resonance is generated by the neutral triplet particle. Because of the formfactor, there are no unphysical high-energy contributions outside the mass range of Fig. 33, which otherwise would result from unitarity violation. For a mass of 500 GeV, these contributions are not suppressed completely for our choice of formfactor parameters. For such small masses, Λ_{ff} should be set to a smaller value than 3 TeV. The total widths of the spin-2 resonances in Fig. 33 are given in Table 6. It should be noted, however, that the widths given in this table merely reflect the parameter choice given above. By increasing the couplings f_i by a factor of, e.g., 5 (or lowering the scale Λ, respectively), all widths and also the spin-2 resonance contributions to the cross sections of Table 5 would increase by a factor of 25, making them much more readily observable.

In Figs. 34 - 37, characteristic transverse-momentum and angular distributions of spin-2 singlet and triplet resonances at 1 TeV are presented. We have selected those distributions which show the most distinctive differences between the different scenarios. On the left hand sides, the distributions of the SM electroweak continuum with and without a spin-2 resonance are depicted at LO and NLO QCD accuracy. The right hand sides compare the singlet and triplet resonance and different coupling parameters at NLO QCD accuracy. In all cases, the electroweak SM continuum is included in a mass bin around the resonance.

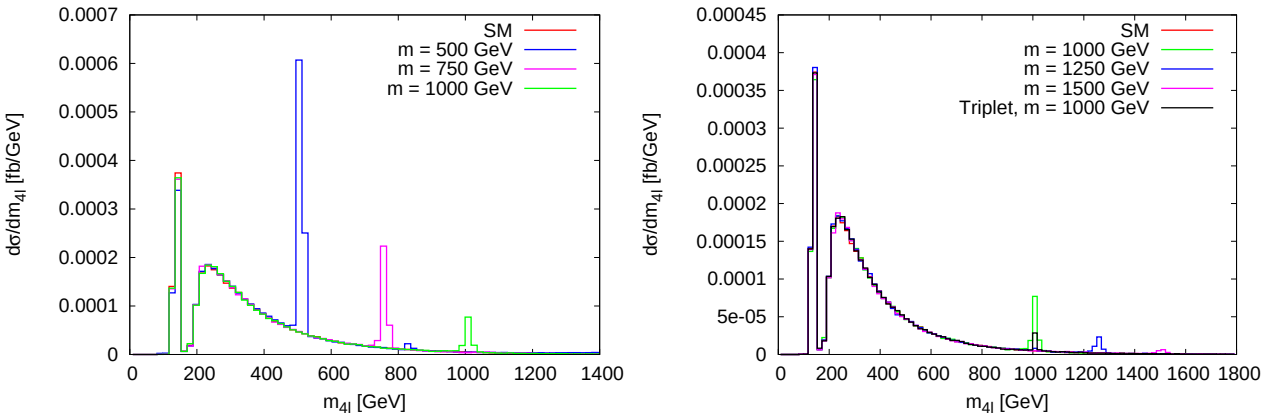

Figure 33: Invariant-mass distribution of the four final-state leptons: Spin-2 singlet and triplet resonance with different masses in the VBF process $pp \to e^+ e^- \mu^+ \mu^- jj$ at NLO QCD accuracy.

All figures are normalized to the NLO cross section. In order to reveal the characteristics of spin-2 resonances, additional cuts on the invariant mass of the four leptons are imposed. For the coupling scenarios $f_1 = f_2 = f_5 = 1$, $f_1 = f_2 = 1$ and for the SM continuum without a spin-2 resonance, they are chosen as $m_{4l} = 1000 \pm 50$ GeV. For the triplet case, we set $m_{4l} = 1000 \pm 10$ GeV and for $f_5 = 1$, we use $m_{4l} = 1000 \pm 5$ GeV. The latter cases are presented for illustration only, since the experimental resolution is expected to be worse. However, for larger values of f_i/Λ and resulting larger production cross sections of the spin-2 resonances, the characteristic distributions would also be visible for less stringent mass cuts. With these additional cuts, we obtain a signal-to-background ratio of approximately one in case of $f_5 = 1$, approximately three for $f_1 = f_2 = 1$ and approximately four in the other cases, where "background" again refers to the electroweak SM continuum.

Distinctive differences between a spin-2 resonance and the electroweak SM background appear especially in the distribution of the transverse momentum of the hardest final-state lepton (Fig. 34), the azimuthal angle difference between the two tagging jets (Fig. 35), the cosine of the angle between the momenta of an incoming and an outgoing electroweak boson in the rest frame of the spin-2 resonance (or of the four final-state leptons, respectively) (Fig. 36) and the pseudorapidity difference between the two positively charged final-state leptons (Fig. 37). The NLO QCD corrections do not have a considerable impact on cross sections and distributions in the high invariant-mass region analyzed here. A spin-2 triplet resonance resembles a singlet resonance with couplings $f_1 = f_2 = f_5 = 1$. The coupling f_5 alone leads to different distributions throughout. This is not just an effect of the sizable electroweak background for small values of f_5/Λ, but originates from the different tensor structure, as we have verified by comparing with the case $f_5 = 10$:

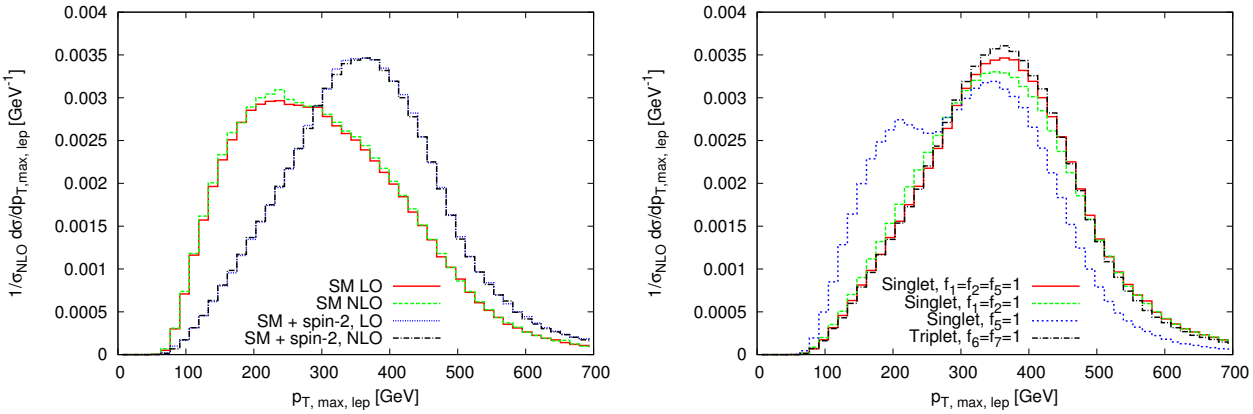

Figure 34: Normalized transverse-momentum distribution of the hardest final-state lepton for events near the spin-2 resonance at 1 TeV (see text for details). Left hand side: Electroweak SM continuum with and without a spin-2 singlet resonance with couplings $f_1 = f_2 = f_5 = 1$ at LO and NLO QCD accuracy; right hand side: with a spin-2 singlet or triplet resonance with different coupling parameters at NLO QCD accuracy.

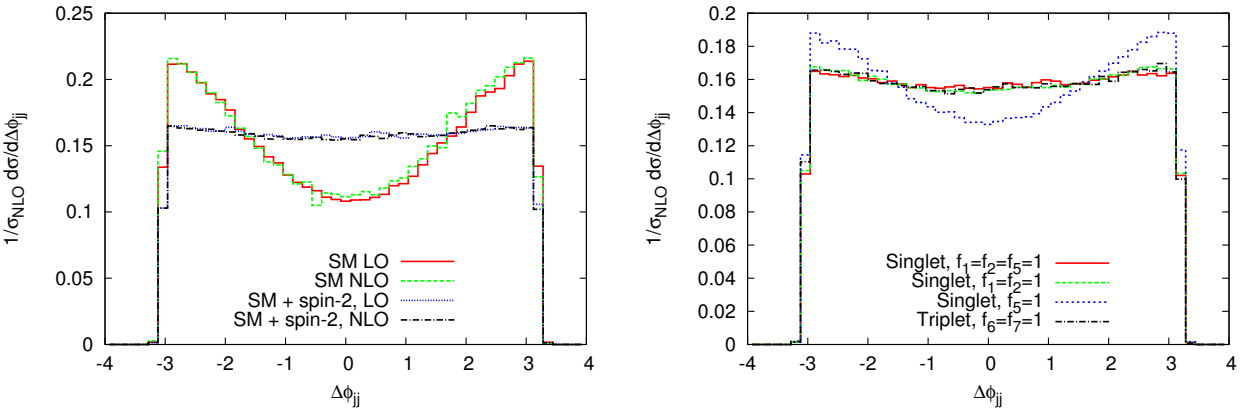

Figure 35: Azimuthal angle difference between the two tagging jets for different cases as in Fig. 34.

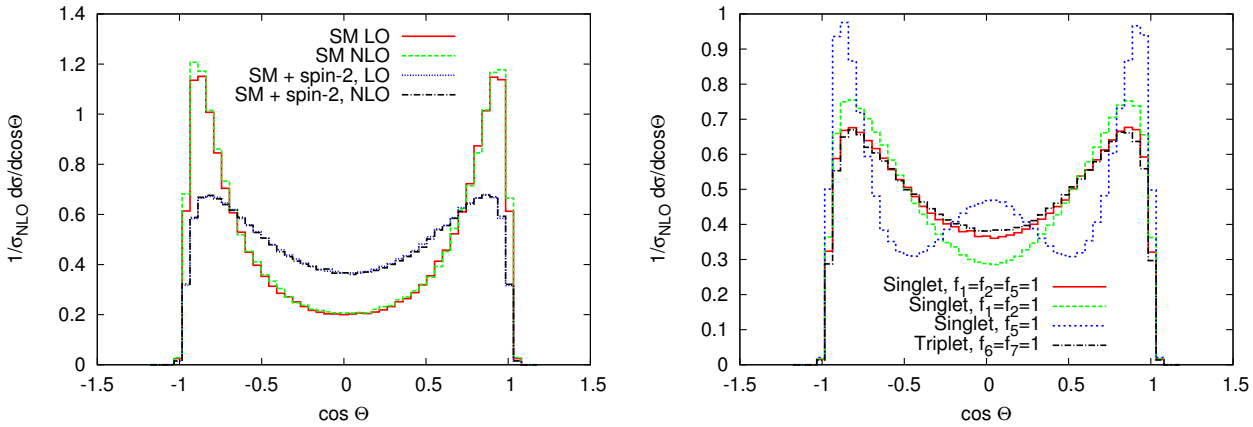

Figure 36: Cosine of the angle between the momenta of an incoming and an outgoing electroweak boson in the rest frame of the spin-2 resonance. The parameters for the different cases are as in Fig. 34.

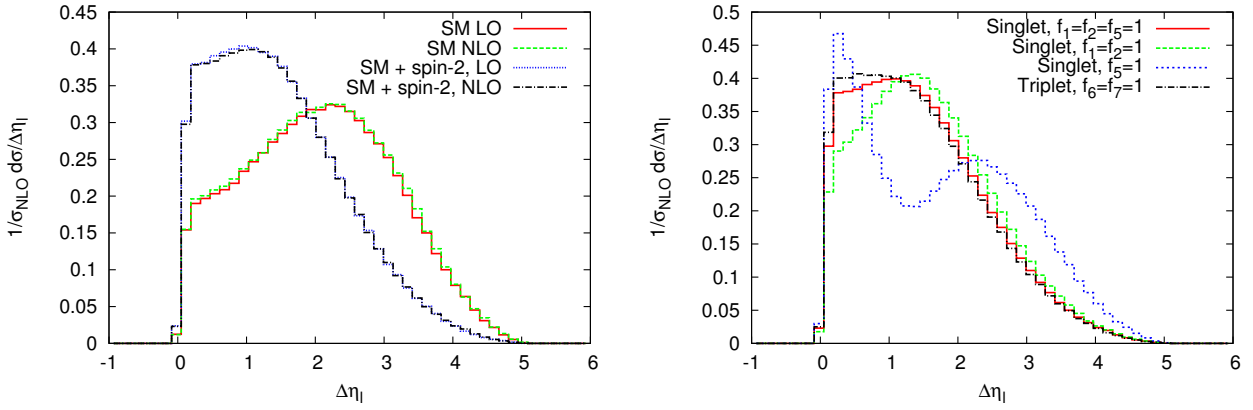

Figure 37: Pseudorapidity difference between the two positively charged final-state leptons, different cases as in Fig. 34.

For $f_5 = 10$, the $\Delta\Phi_{jj}$ distribution approaches the one of the other spin-2 cases, whereas for the $\cos\Theta$ distribution the peak around $\cos\Theta = 0$ becomes more prominent. The cases $f_1 = f_2 = f_5 = 1$ and $f_1 = f_2 = 1$ are difficult to distinguish because of the numerically insignificant f_5 contribution. However, small differences, which do not only stem from contamination of the SM continuum, arise in the $\cos\Theta$ and $\Delta\eta_l$ distribution.
The $\cos\Theta$ distribution of Fig. 36 is not accessible experimentally for processes with final-state neutrinos. However, the corresponding results can be directly transferred to such cases, since for Fig. 36, the momenta of the electroweak bosons were not reconstructed from final-state momenta, as in Sec. 3.3, but taken directly from the Monte Carlo information. Apart from $\cos\Theta$, we have also studied the angle between the momenta of an outgoing electroweak boson and one of the tagging jets in the rest frame of the spin-2 resonance (or of the four final-state leptons, respectively). This distribution shows characteristics similar to $\cos\Theta$.

3.7.2 Other VBF processes with four final-state leptons

The VBF process $pp \to e^+ e^- \nu_\mu \overline{\nu}_\mu jj$ is very similar to $pp \to e^+ e^- \mu^+ \mu^- jj$, which was studied previously, since both channels are dominated by $ZZjj$ production. Theoretically, a spin-2 resonance in the invariant-mass spectrum of the four final-state leptons as well as the transverse-momentum and angular distributions with a cut on the invariant four-lepton mass look the same, apart from the fact that there is no use in analyzing correlations of the two charged leptons, since they originate from the same electroweak boson then. In this case, since the invariant four-lepton mass cannot be reconstructed experimentally, the transverse mass of the final-state lepton system $e^+ e^- \nu_\mu \overline{\nu}_\mu$ has to be considered instead, which is defined as [99]:

$$m_T = \sqrt{(E_{T,ll} + E_{T,\text{miss}})^2 - (\boldsymbol{p}_{T,ll} + \boldsymbol{p}_{T,\text{miss}})^2}, \tag{3.42}$$

with

$$E_{T,ll} = \sqrt{\boldsymbol{p}_{T,ll}^2 + m_Z^2} \ , \quad E_{T,\text{miss}} = \sqrt{\boldsymbol{p}_{T,\text{miss}}^2 + m_Z^2}. \tag{3.43}$$

Here, $E_{T,ll}$ and $\boldsymbol{p}_{T,ll}$ denote the transverse energy and momentum of the two charged leptons and $E_{T,\text{miss}}$ and $\boldsymbol{p}_{T,\text{miss}}$ those of the two neutrinos.
Even though an excess from the spin-2 resonance is hardly visible in the transverse-mass spectrum for the present parameter choice, some of the features of the differential distributions remain accessible if a transverse-mass cut like $m_T = 1000 \pm 100$ GeV is imposed instead of the cut on the invariant four-lepton mass discussed in Sec. 3.7.1. While the

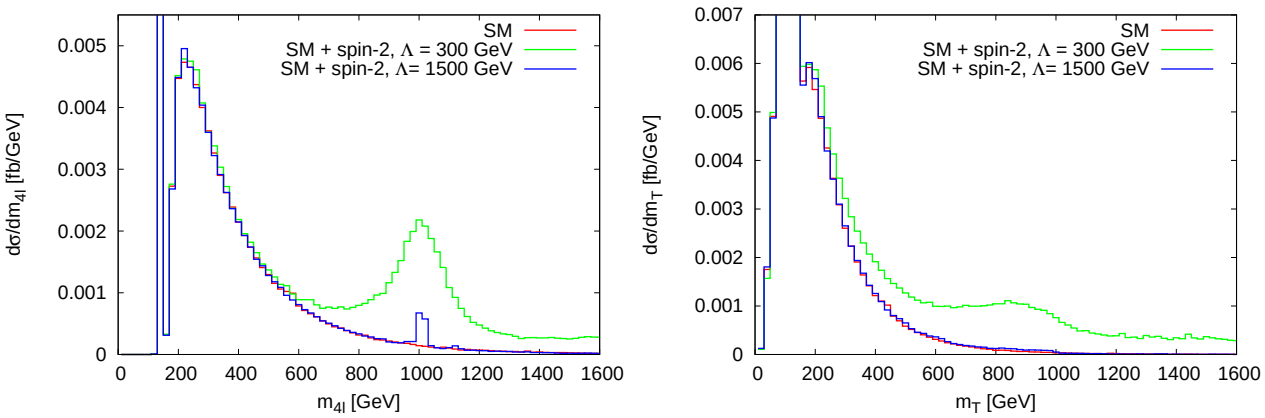

Figure 38: $pp \to W^+W^- jj \to e^+ \nu_e \mu^- \overline{\nu}_\mu jj$ with and without a spin-2 singlet resonance for different values of Λ at NLO QCD accuracy. Left hand side: Invariant mass of the four final-state leptons, right hand side: Transverse mass.

difference in the transverse-momentum distribution of the hardest lepton (left hand side of Fig. 34) disappears, the azimuthal angle difference of the two tagging jets (Fig. 35) persists.

In the VBF process $pp \to W^+W^- jj \to e^+ \nu_e \mu^- \overline{\nu}_\mu jj$, it is hard to access the characteristics of spin-2 resonances experimentally, since $t\bar{t}$ + jets constitute a large background to this process at the LHC. Moreover, the spin-2 singlet resonance (Fig. 38) is smaller than in the processes studied before and the triplet resonance is even smaller, since the uncharged triplet particle couples to two W bosons only via the f_6 term, whereas the Feynman rules for vertices with photons and Z bosons involve the coupling f_7 (see 3.12). As before, the invariant four-lepton mass is not accessible experimentally and the transverse mass of the lepton system $e^+ \nu_e \mu^- \overline{\nu}_\mu$ (Eq. (3.36)) has to be considered instead.

Fig. 38 depicts a spin-2 singlet resonance for different values of Λ in the invariant four-lepton mass spectrum, which is only theoretically accessible, and in the transverse-mass distribution. Here, the high Higgs-resonance peak is cut off in order to focus on the spin-2 resonance region. For the usual parameters, with $\Lambda = 1.5$ TeV, the transverse-mass spectrum is approximately the same for the electroweak SM continuum with and without a spin-2 resonance. Even for Λ as small as 300 GeV (or for large couplings f_i, respectively), the resonance is smeared out. The characteristic features of the transverse-momentum and angular distributions, which are theoretically similar to those of the VBF process $pp \to e^+ e^- \mu^+ \mu^- jj$, remain accessible with a cut on the transverse mass, if the couplings are not too small. For the usual settings, with $\Lambda = 1.5$ TeV, the differences between the distributions of the electroweak continuum with and without a spin-2 resonance are small and difficult to access in the W^+W^- channel at the LHC.

In $pp \to VV\,jj \to e^+\,\nu_e\,\mu^+\mu^-\,jj$ and $pp \to VV\,jj \to e^-\,\overline{\nu}_e\,\mu^+\mu^-\,jj$, only charged resonances are possible. Therefore, these processes can feature a spin-2 triplet resonance generated by the charged triplet particle, but no singlet resonance, which is useful to distinguish between the spin-2 singlet and triplet scenario. Again, the resonance is only theoretically accessible in the invariant four-lepton mass spectrum, and the features of the distributions with a mass cut around the resonance are the same as before. The corresponding transverse mass in this case reads [99]:

$$m_T = \sqrt{(E_{T,lll} + E_{T,\text{miss}})^2 - (\boldsymbol{p}_{T,lll} + \boldsymbol{p}_{T,\text{miss}})^2}, \tag{3.44}$$

with

$$E_{T,lll} = \sqrt{\boldsymbol{p}_{T,lll}^2 + m_{lll}^2}\ , \quad E_{T,\text{miss}} = |\boldsymbol{p}_{T,\text{miss}}|, \tag{3.45}$$

where m_{lll} is the invariant mass of the charged-lepton system, $E_{T,lll}$ ($\boldsymbol{p}_{T,lll}$) its transverse energy (momentum) and $E_{T,\text{miss}}, \boldsymbol{p}_{T,\text{miss}}$ those of the neutrino.
The spin-2 triplet resonance peak can be observed in the transverse-mass spectrum if the couplings are not too small. However, the usual parameters only yield a marginal signal. With a transverse-mass cut of $m_T = 1000 \pm 100$ GeV, the features of the distributions, like the pseudorapidity difference between two final-state leptons of the same charge, can be studied and yield results similar to those found for $pp \to e^+\,e^-\,\mu^+\mu^-\,jj$.

All in all, heavy spin-2 resonances feature specific transverse-momentum and angular distributions in the considered VBF processes, which differ from those of the SM electroweak continuum and might be accessible at the LHC with appropriate cuts if the spin-2 couplings are not too small. Since in the $WZjj$-dominated channels $e^+\,\nu_e\,\mu^+\mu^-\,jj$ and $e^-\,\overline{\nu}_e\,\mu^+\mu^-\,jj$, only charged resonances are possible, they can be useful to distinguish between the spin-2 singlet and triplet scenario.

4 Unitarity of Vector-boson Scattering with Spin-0, Spin-1 or Spin-2 Resonances

A very important feature of the SM Higgs boson is that it preserves the unitarity of the S-matrix (Eq. (2.15)) in elastic vector-boson scattering. In case of the SM without the Higgs boson (which could by realized by a non-linear σ-model), the amplitude of longitudinal WW scattering would grow with the squared center-of-mass energy s, eventually violating unitarity at approximately $s = 1.6$ TeV. In the SM with its Higgs mechanism, unitarity implies that the mass of the physical Higgs boson must be lower than approximately 800 GeV [104]. This condition is naturally fulfilled for the $125 - 126$ GeV particle discovered at the LHC.

Since the S-matrix is related to physical cross sections, any modification of the SM must also imply this conservation of probability (unless the probabilistic interpretation of the S-matrix and, thus, a basic principle of quantum mechanics, is abandoned). Particularly, one can ask if the capability to restore unitarity of vector-boson scattering is a unique feature of the spin-0 Higgs boson or if resonances with a different spin are able to perform the same task. This question is investigated for spin-1 and spin-2 particles in this chapter [9]. To this end, unitarity properties are analyzed by studying the high-energy behavior of partial waves. First, we will focus on the special case of longitudinal WW scattering, which is usually considered to be the most important channel in this context. In order to give a more complete picture of the unitarity properties, we will then generalize the partial-wave analysis to a combined study of all uncharged combinations of weak bosons in the initial and final state, including both longitudinal and transverse modes. Spin-2 particles are investigated within the framework of the effective Lagrangian model described in Sec. 3.1. Additional spin-1 particles appear in a huge variety of different models (see e.g. Ref. [105] and references therein), like in Grand Unified Theories [106], Little Higgs [48] or Extra Dimension models [41] or in superstring constructions [107]. In order to analyze the unitarization power of spin-1 particles in a general way, however, we choose a model-independent ansatz [108], which is outlined in the following section.

4.1 Framework for Spin-1 Resonances

As proposed in many publications in recent years [42,109], it is possible to delay unitarity violation in longitudinal WW scattering by the exchange of heavy spin-1 particles instead of the Higgs boson of the SM. In the proposed five-dimensional or deconstructed models

[9] Work done in collaboration with Franziska Schissler.

(see Sec. 2.2.2), there is usually a tension between unitarity requirements, which impose a relatively light mass scale for the new resonances, and electroweak precision data (EWPD), which tend to favor heavy masses for the new vector states. Furthermore, LHC data set strong limits on the masses of additional W' and Z' bosons which couple to fermions from searches in various decay channels: $W' \to l\nu$ [110], $W' \to tb$ [111], $W'/Z' \to jj$ [112], $Z' \to ll$ (with $ll = e^+e^-, \mu^+\mu^-$ [113] or $\tau^+\tau^-$ [114]), $Z' \to t\bar{t}$ [115] and $Z' \to b\bar{b}$ [116]. Therefore, we will only consider additional vector resonances with tiny or vanishing couplings to SM fermions here.

From EWPD, lower-mass bounds of $250 - 380$ GeV [117–119] were derived, where the exact value depends on the considered models. The tension between EWPD and relatively light spin-1 resonances mainly stems from changes in the WWZ-coupling. This coupling is related to the parameter Δg_{1Z} [120] which should be of $\mathcal{O}(10^{-2})$ [121]. The oblique electroweak corrections at tree level, parametrized by S, T and U [122], can be adjusted to vanish, as argued in [123]. It is shown that $\alpha T \approx 0$ if one incorporates a custodial symmetry which ensures

$$\rho = \frac{m_W}{m_Z \cos\theta_W} = 1 \tag{4.1}$$

at tree level. $\alpha S \approx 0$ at tree level can be achieved for tiny or vanishing fermion couplings. Even at the one-loop level, it should be possible to find parameter combinations leading to small oblique corrections, which was shown for the Three Site Higgsless Model in [124]. To construct a model of EWSB, one can take the Four Site Higgsless model [117,125] as a starting point. It predicts all the known SM particles except for the Higgs boson and six additional vector bosons, denoted by $W^{\pm}_{1,2}$ and $Z_{1,2}$. In this framework, one needs to fix the WWZ-coupling to its SM value (or the allowed Δg_{1Z} region) to avoid conflicts with EWPD.

To delay unitarity violation in models with additional vector states to very high energies, one has to impose sum rules which have to be fulfilled by the various couplings of vector bosons among each other. They can be derived from vector-boson scattering amplitudes. In these amplitudes, there exist terms which grow continuously with the energy and need to be canceled in order to obtain a UV complete amplitude. This cancellation then leads to relations between different couplings, which are the mentioned sum rules. In theories with a finite extra dimension, these sum rules emerge naturally from the completeness of Kaluza-Klein modes [42]. Alternatively, they can be built into a deconstructed theory by the use of hidden symmetries as was argued in Ref. [119] and references therein.

In the framework of two additional vector-boson triplets, like in the Four Site Higgsless

model, the terms quadratic and quartic in the center-of-mass energy vanish in the longitudinal scattering amplitudes of $WW \to WW$ and $WZ \to WZ$ (or $WW \to ZZ$ or $ZZ \to WW$, respectively) scattering, if we impose the following sum rules for the six additional $W^{\pm}_{1,2}$ and $Z_{1,2}$ resonances [126, 127]:

$$g_{WWWW} = \sum_{k=0}^{2} g^2_{WWZ_k} + g^2_{WW\gamma}, \tag{4.2}$$

$$4\, m_W^2\, g_{WWWW} = 3 \sum_{k=0}^{2} m^2_{Z_k}\, g^2_{WWZ_k}, \tag{4.3}$$

$$g_{WWZZ} = \sum_{k=0}^{2} g^2_{W_kWZ}, \tag{4.4}$$

$$2\left(m_W^2 + m_Z^2\right) g_{WWZZ} = \sum_{k=0}^{2} \left(3\, m^2_{W_k} - \frac{\left(m_W^2 - m_Z^2\right)^2}{m^2_{W_k}}\right) g^2_{W_kWZ}. \tag{4.5}$$

Here, $g_{abc(d)}$ denotes the coupling of a, b, c (and d) bosons, with $W_0 = W$ and $Z_0 = Z$ being the weak bosons with SM mass. The equations (4.2) and (4.4) result from the cancellation of terms which grow proportional to s^2, whereas Eqs. (4.3) and (4.5) ensure the cancellation of terms proportional to s.

By combining Eqs. (4.2) and (4.3), g_{WWWW} can be eliminated, yielding

$$g^2_{WWZ_2} = \underbrace{\frac{1}{\left(3m^2_{Z_2} - 4m^2_W\right)}}_{>0} \Bigg[\overbrace{4m^2_W g^2_{WW\gamma} + g^2_{WWZ}\left(4m^2_W - 3m^2_Z\right)}^{>0} + \underbrace{g^2_{WWZ_1}\left(4m^2_W - 3m^2_{Z_1}\right)}_{<0} \Bigg]. \tag{4.6}$$

Demanding that the coupling of the Z_2 boson to SM particles should be real, the square bracket in Eq. (4.6) must be positive. This constraint implies a maximal value of g_{WWZ_1}:

$$g^2_{WWZ_1} \leq \frac{4m^2_W g^2_{WW\gamma} + g^2_{WWZ}\left(4m^2_W - 3m^2_Z\right)}{\left(3m^2_{Z_1} - 4m^2_W\right)} = \left(g^{\max}_{WWZ_1}\right)^2. \tag{4.7}$$

The same procedure, using Eqs. (4.4) and (4.5), leads to a maximal value for g_{W_1WZ}:

$$g^2_{W_1WZ} \leq \frac{\left(2(m_W^2+m_Z^2)-3m_W^2+(m_Z^2-m_W^2)^2/m_W^2\right)}{\left(3m_{W_1}^2-2(m_W^2+m_Z^2)-(m_Z^2-m_W^2)^2/m_{W_1}^2\right)}\, g^2_{WWZ} = \left(g^{\max}_{W_1WZ}\right)^2. \tag{4.8}$$

Note that the maximal values $g^{\max}_{WWZ_1}$(4.7) and $g^{\max}_{W_1WZ}$(4.8) are dominated by a $1/m_{V_1}$ dependence (with $V = W,\, Z$).

Motivated by these inequalities, the parameters $\xi_i \in [-1,1]$ ($i = W,\, Z$) are introduced, which will be used to find configurations in which unitarity violation can be delayed to very high energies:

$$g_{WWZ_1} = \xi_Z\, g^{\max}_{WWZ_1}\,, \;\; g_{W_1WZ} = \xi_W\, g^{\max}_{W_1WZ}. \tag{4.9}$$

$\xi_i = 1$ corresponds to no second additional spin-1 states, since e.g. g_{WWZ_1} reaches its maximal values and the square bracket in Eq. (4.6) vanishes. The sum rules (4.2)-(4.5) are then fulfilled by the first additional vector states. Using g_{WWZ_1}, g_{W_1WZ} and g_{WWZ}, the other couplings can be determined via the sum rules (4.2)-(4.5). $g_{WW\gamma}$ has the same value as in the SM since it is determined by the charge of the W boson. In the present analysis, the mass of the first resonances W_1 and Z_1 as well as of the second resonances W_2 and Z_2 are taken as free parameters. ξ_W and ξ_Z will also be varied, whereas the WWZ-coupling will be fixed to its SM value to comply with EWPD, as mentioned before.

4.2 Analyzing Unitarity: Theoretical Concepts and Practical Tools

For the analysis of the high-energy behavior of the considered models, a partial-wave analysis is an adequate tool. Following Ref. [128], the partial-wave decomposition of the matrix element for fixed helicity combinations is given by

$$\mathcal{M} = 16\pi \sum_J (2J+1)\, a^J_{\lambda\mu}\, d^J_{\lambda\mu}(\theta), \tag{4.10}$$

where $\lambda\,(\mu)$ is the helicity difference between the initial (final) electroweak bosons and $d^J_{\lambda\mu}(\theta)$ are the Wigner d-functions which can be found in [92]. The d-functions obey the following orthogonality relation [128]:

$$\int_0^\pi d^J_{m,m'}\,(\theta)\, d^{J'}_{m,m'}\,(\theta)\, \sin\theta\, d\theta = \delta_{JJ'}\, \frac{2}{2J+1}. \tag{4.11}$$

This relation can be used to obtain the coefficients $a^J_{\lambda\mu}$: Multiplying Eq. (4.10) by $d^{J'}_{\lambda\mu}(\theta)$, integrating over $\sin\theta\, d\theta$ and inserting Eq. (4.11) yields

$$a^J_{\lambda\mu} = \frac{1}{32\pi} \int_0^\pi \mathcal{M}\, d^J_{\lambda\mu}(\theta) \sin\theta\, d\theta\,. \tag{4.12}$$

The calculation of the coefficients $a^J_{\lambda\mu}$ was performed by using a FORTRAN program, which was originally written by C. Englert [129] and was modified and extended for the present analysis. It uses HELAS routines [77] to calculate the tree-level matrix elements and the routine *gaussint* [130] for the integration over θ. To avoid singularities originating from t-channel photon exchange, the lower integration limit was set to 0.1° in the case of WW scattering. We also performed internal checks against the FeynArts [85]/ FormCalc [86] framework.
Since partial waves with small angular momentum give the largest contributions to the scattering amplitude, we will only consider the $J = 0$ partial wave a^0_{00} (=: a_0) in the following.

Unitarity of the S-matrix implies [131]

$$|\mathrm{Re}(a_0)| \leq \frac{1}{2}. \tag{4.13}$$

This provides a useful requirement which can be applied to investigate unitarity.
A first step of the analysis is to apply the condition (4.13) to the coefficients a_0 for particular modes (either the transverse modes, denoted by $++$ and $--$, or the longitudinal ones, labeled 00) and particular initial and final-state weak bosons. However, in order to obtain more general results, a combined analysis of all modes and all weak bosons should be performed. To this end, we apply a method which can e.g. be found in Refs. [104,132]. We set up a matrix of all relevant combinations of uncharged initial and final states,

$$\mathcal{A} = \begin{pmatrix} a_0(W^+W^- \to W^+W^-) & a_0(W^+W^- \to ZZ)/\sqrt{2} \\ a_0(ZZ \to W^+W^-)/\sqrt{2} & a_0(ZZ \to ZZ)/2 \end{pmatrix}, \tag{4.14}$$

with the sub-matrices

$$a_0(VV \to VV) = \begin{pmatrix} (--) \to (--) & (--) \to (00) & (--) \to (++) \\ (00) \to (--) & (00) \to (00) & (00) \to (++) \\ (++) \to (--) & (++) \to (00) & (++) \to (++) \end{pmatrix}. \tag{4.15}$$

Taking external photons into account is not necessary for our analysis, since in case of additional spin-1 particles, the SM photons only couple to the charged W bosons and for spin-2 resonances, it is not useful to consider the couplings which lead to vertices involving photons (see Sec. (4.3.2)).
All the sub-matrices (4.15) are symmetric and also $a_0(WW \to ZZ)$ and $a_0(ZZ \to WW)$ are mirror images of each other, which was used as a test of the calculation. Additionally, the entries in $\mathcal{A}$ stemming from different helicity combinations in the initial and final state are found to be negligible, since these amplitudes are zero in the massless limit due to angular-momentum conservation.

The eigenvalue of the matrix (4.14) with the largest absolute value is labeled $a_0^{\max}$ in the following and must fulfill the more general unitarity requirement

$$|\mathrm{Re}(a_0^{\max})| \leq \frac{1}{2}. \tag{4.16}$$

The matrix (4.14) was diagonalized using the LAPACK ZGEEV subroutine [133]. In our calculation, we use the electroweak input parameters given in Sec. 3.2.4 and apply a narrow-width approximation, where the widths of intermediate particles are set to zero. Since we are considering energies much higher than the masses of the resonances, this is a reasonable assumption.

4.3 Unitarity with Spin-2 Resonances

4.3.1 Longitudinal WW scattering

In this section, we investigate whether it is possible to unitarize longitudinal WW scattering for the SM without a Higgs boson by including the spin-2 $SU(2)$ singlet particle of the effective model presented in Sec. 3.1 [10]. For the SM without a Higgs boson, the Feynman graphs contributing to WW scattering are given in Fig. 39. In this case, unitarity is violated above approximately 1.6 TeV, but restored by including the Higgs boson. Since the spin-2 model yields the same Feynman diagrams as the SM Higgs mechanism, namely s- and t-channel exchange of a neutral particle (Fig. 40), one can already conjecture that the spin-2 particle could perform the task of the Higgs boson in that particular process.
When analyzing the high-energy behavior of the matrix elements for purely longitudinal $WW \to WW$ scattering, one finds that for the SM without a Higgs boson, the amplitude

[10] Note that this approach differs significantly from the one used in Ref. [134], where an analysis of unitarity in WW scattering with a triplet of antisymmetric tensor bosons is provided.

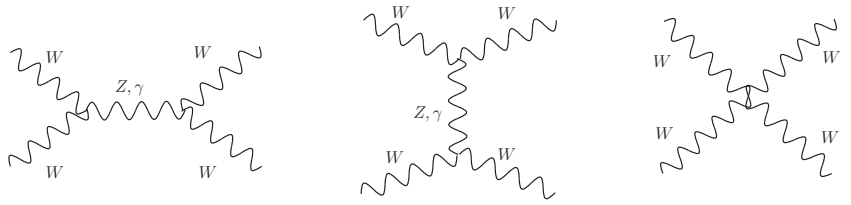

Figure 39: SM Feynman graphs without a Higgs boson in WW scattering.

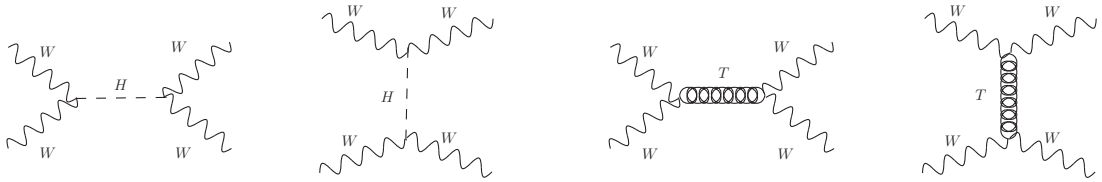

Figure 40: Feynman graphs in WW scattering. Left hand side: with a Higgs boson, right hand side: with a spin-2 particle.

(and therefore also $\mathrm{Re}(a_0)$) is proportional to s, whereas for the spin-2 diagrams without a formfactor, it is proportional to s^3. A cancellation of both contributions is only possible if the spin-2 and the SM diagrams without a Higgs boson have opposite signs (which turns out to be the case) and if their absolute values grow with the same power of s for high energies. The high-energy behavior of the spin-2 contributions can be varied by multiplying the amplitude with the formfactor (3.15), which is proportional to $s^{-n_{ff}}$ for high energies. Hence, by choosing $n_{ff} = 2$, the spin-2 contributions cancel the SM ones for adjusted parameters of the spin-2 model. Thereby, unitarity can be preserved up to nearly arbitrary high energies.

This is illustrated by Fig. 41, which depicts the energy dependence of $\mathrm{Re}(a_0)$ for the SM with and without a Higgs boson and a spin-2 particle, both with a mass of 126 GeV. The couplings of the spin-2 model are chosen as $f_5 = 1, f_{i\neq 5} = 0$, the parameters of the formfactor are $n_{ff} = 2$, $\Lambda_{ff} = 1$ TeV and the energy scale Λ is tuned to 7655 GeV. The longitudinal WW scattering amplitude depends only weakly on the coupling f_2 and a change of the value of f_5 or the mass of the spin-2 particle can be compensated by a change of Λ. Other couplings f_i are not involved in WW scattering. The energy scales Λ and Λ_{ff}, however, have to be fine-tuned. The impact of a variation of these parameters is investigated in Fig. 42, which shows the dependence of $\mathrm{Re}(a_0)$ on either Λ (left hand side) or Λ_{ff} (right hand side), while keeping all other parameters fixed to the values given above. One can see that already deviations of few GeV impair the high-energy behavior,

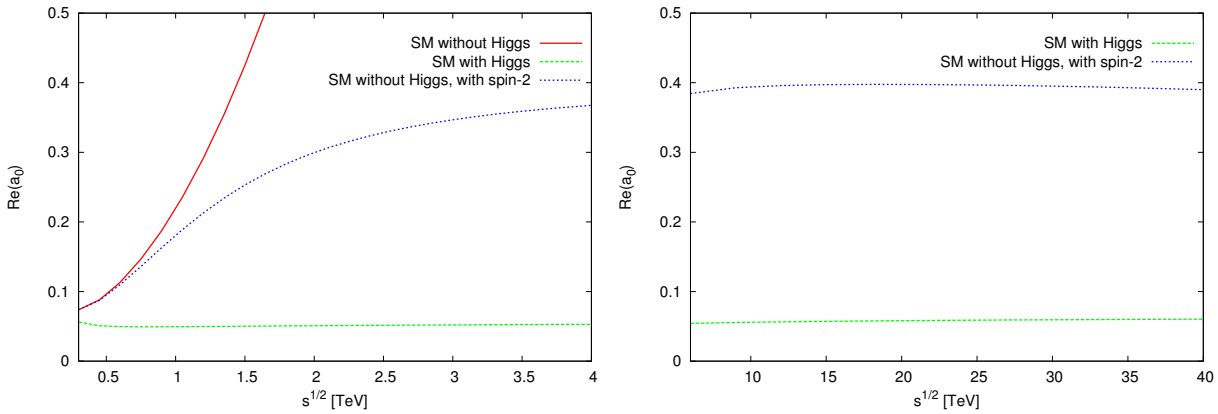

Figure 41: Longitudinal WW scattering: Energy dependence of $\mathrm{Re}(a_0)$ for the SM with and without a Higgs boson or a spin-2 particle, both with a mass of 126 GeV. The parameters of the spin-2 model are $f_5 = 1, f_{i\neq 5} = 0$, $n_{ff} = 2$, $\Lambda_{ff} = 1\,\mathrm{TeV}$, $\Lambda = 7655\,\mathrm{GeV}$.

especially for Λ_{ff}, which leads to a violation of the unitarity condition $|\mathrm{Re}(a_0)| \leq 0.5$ (Eq. (4.13)) at low scales. This implies that a significant amount of fine-tuning is required in order to preserve unitary in longitudinal WW scattering with a spin-2 particle instead of a SM Higgs boson.

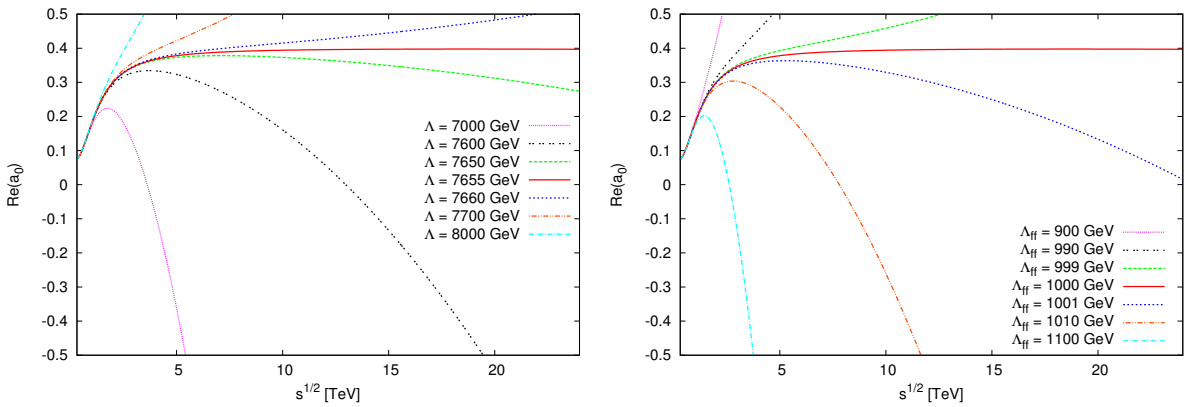

Figure 42: Dependence of $\mathrm{Re}(a_0)$ on the spin-2 parameters Λ (left hand side) and Λ_{ff} (right hand side) in longitudinal WW scattering.

4.3.2 General Case

Now we investigate the more general case by considering the longitudinal and transverse modes of the relevant electroweak bosons together. Therefore, we analyze the eigenvalues of the matrix (4.14) and apply the condition (4.16). Fig. 43 illustrates the high-energy behavior of the largest eigenvalue for the SM with and without a Higgs boson and a

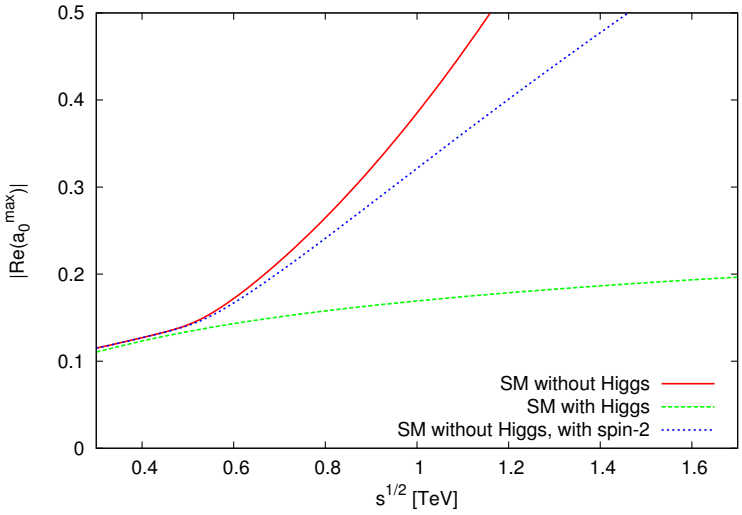

Figure 43: Energy dependence of the largest eigenvalue of the matrix (4.14) for the SM with and without a Higgs boson or a spin-2 particle, both with a mass of 126 GeV. The parameters of the spin-2 model are $f_5 = 1, f_{i\neq 5} = 0$, $n_{ff} = 2$, $\Lambda_{ff} = 1\,\text{TeV}$ and $\Lambda = 7655\,\text{GeV}$.

spin-2 particle, both with a mass of 126 GeV. We consider the same set of spin-2 model parameters as before, $f_5 = 1, f_{i\neq 5} = 0$, $n_{ff} = 2$, $\Lambda_{ff} = 1\,\text{TeV}$ and $\Lambda = 7655\,\text{GeV}$, which was found to preserve unitarity in longitudinal WW scattering.
For the SM without a Higgs boson, unitarity is violated already above approximately 1.2 TeV, whereas considering only longitudinal WW scattering yields the weaker bound of approximately 1.6 TeV, as shown in Sec. 4.3.1. By including a Higgs boson, unitarity can be restored.

This figure also illustrates that for the SM without a Higgs boson, but with a spin-2 particle, it is possible to delay unitarity violation from approximately 1.2 TeV to 1.5 TeV for the given fine-tuned parameter set. However, in contrast to the case of longitudinal WW scattering, it is not possible to restore unitarity by including a spin-2 particle with an appropriate formfactor instead of a Higgs boson.

To understand this, the different sub-matrices (4.15) of $\mathcal{A}$ in Eq. (4.14) have to be investigated: The sub-matrix $a_0(WW \to WW)$ contains the longitudinal WW scattering of Sec. 4.3.1, where we have illustrated that the spin-2 amplitudes can cancel the SM ones due to their opposite signs. The spin-2 contribution to the transverse modes is negligible. Therefore, unitarity can be restored for the sub-matrix $a_0(WW \to WW)$ if the parameters are fine-tuned as in Sec. 4.3.1.
However, the situation is different in case of the sub-matrices $a_0(WW \to ZZ)$ and

$a_0(ZZ \to WW)$, where the spin-2 and the SM amplitudes have the same sign, which means that a cancellation among them is not possible. The entries of the $a_0(ZZ \to ZZ)$ sub-matrix are equal to zero for the SM without a Higgs boson, whereas for the spin-2 amplitudes, they grow continuously when the center-of-mass energy is increased and cannot be canceled.
One might think that these different effects can be counterbalanced by tuning the spin-2 coupling parameters. However, this is not possible, since the Feynman rules of the TWW and the TZZ vertex have the same structure (see Eq. (3.9)). It is not advantageous to include the couplings f_1 and f_2, because they enhance the transverse modes, but yield a minor contribution to the crucial longitudinal ones. Additionally, they lead to non-vanishing couplings of the spin-2 particle to photons (see Eq. (3.9)), which would have to be taken into account by enlarging the matrix (4.14) by the various combinations with photons in the initial and final state. This would impair the high-energy behavior of the largest eigenvalue even more, since the additional sub-matrices containing photons would exhibit further diverging spin-2 contributions which cannot be canceled, as in case of the $ZZ \to ZZ$ sub-matrix.

After analyzing the general case, we arrive at the conclusion that it is not possible to restore unitarity by including a spin-2 particle. Therefore, we now investigate the impact of spin-1 resonances.

4.4 Unitarity with Spin-1 Resonances

In contrast to the spin-2 case, unitarity can be restored for combined channels of SM weak-boson scattering by additional spin-1 particles within the framework of Sec. 4.1. The imposed sum rules (4.2)–(4.5) ensure the cancellation of terms which grow quadratically and quartically with the center-of-mass energy. In the general spin-2 case of Sec. 4.3.2, the ZZ scattering caused the violation of unitarity already at low energies. For intermediate neutral spin-1 particles, however, there is no such scattering.
Fig. 44 depicts the real parts of the eigenvalues of the 6×6 partial-wave matrix (4.14), where two of the eigenvalues are degenerate. The red solid lines show their energy dependence for the SM with a 126 GeV Higgs boson. The blue dotted lines correspond to the SM without Higgs, but with additional spin-1 particles $W_1^\pm$ and Z_1 with masses $m_{W_1} = m_{Z_1} = 275$ GeV and no second triplet of vector states. As we will discuss below, this is the best configuration we found to mimic the high-energy behavior of the SM with the Higgs boson. Within the SM with the Higgs boson, all the longitudinal contributions

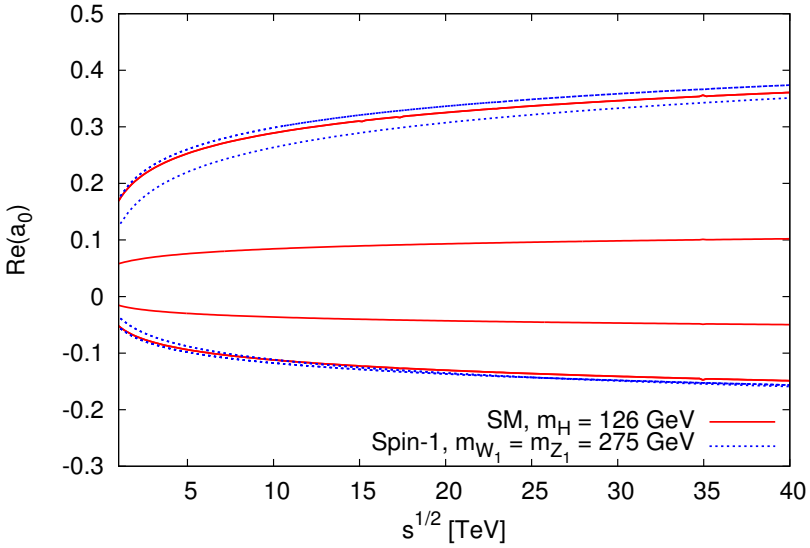

Figure 44: Eigenvalues of the partial-wave matrix (4.14) for the SM with a Higgs boson or with an additional triplet of spin-1 particles.

of the four sub-matrices (4.15) are of order $\mathcal{O}(10^{-2})$, yet the contributions from transverse modes have larger values ($\mathcal{O}(10^{-1})$). For additional intermediate spin-1 particles instead of a Higgs boson, transverse modes are approximately of the same size, whereas the longitudinal contributions are larger than in the SM with Higgs. Nevertheless, Fig. 44 demonstrates that it is possible to restore unitarity in vector-boson scattering without a scalar boson. In contrast to the spin-2 case, no formfactor is needed to control the high-energy behavior of the scattering amplitudes.

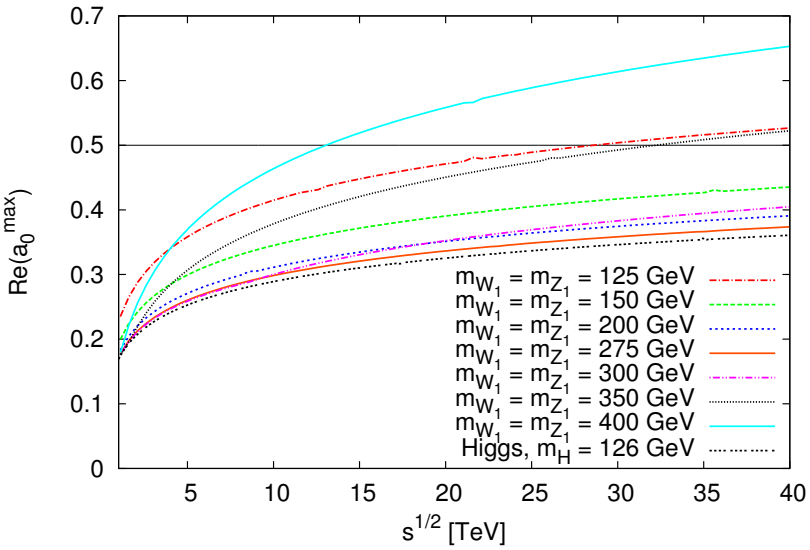

Figure 45: Largest eigenvalue of the partial-wave matrix (4.14) for the SM with a Higgs boson ($m_H = 126$ GeV) or with an additional triplet of spin-1 particles with different masses.

Fig. 45 shows the energy dependence of the largest eigenvalue of (4.14) for the SM with a Higgs boson ($m_H = 126$ GeV) or with one additional triplet of spin-1 states with different masses $m_{W_1} = m_{Z_1}$. It demonstrates that the condition $|\mathrm{Re}(a_0^{\max})| \leq 0.5$ (Eq. (4.16)) is

fulfilled up to energies above 40 TeV if $m_{W_1} = m_{Z_1} \approx 150 - 300$ GeV. Hence, the unitarity of weak-boson scattering amplitudes can be restored with one additional triplet of light spin-1 states, with the ideal value of the masses being $m_{W_1} = m_{Z_1} = 275$ GeV.

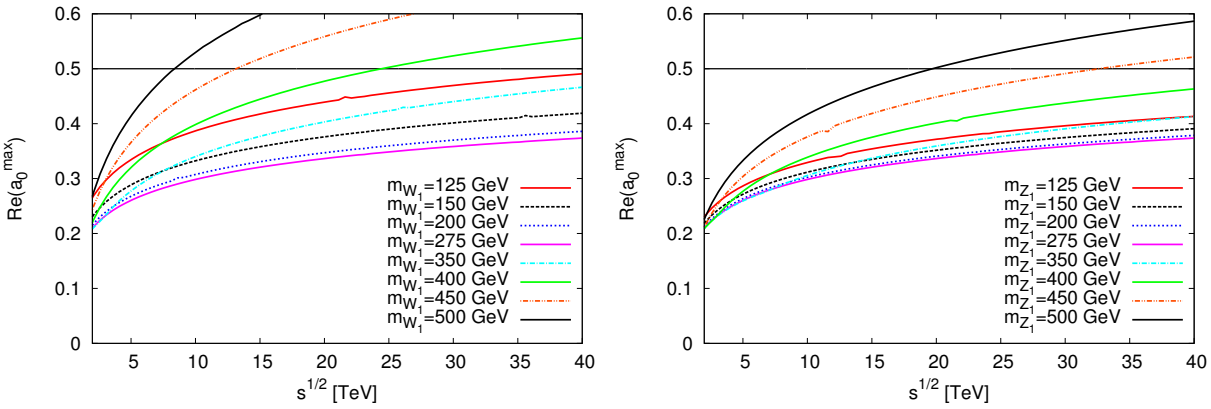

Figure 46: Dependence of the largest eigenvalue on m_{W_1} for $m_{Z_1} = 275$ GeV (left hand side) and on m_{Z_1} for $m_{W_1} = 275$ GeV (right hand side).

While only mass-degenerate spin-1 states have been considered so far, we will now study the more general scenario where the W_1 and the Z_1 boson have different masses. The impact of the variation of either m_{W_1} or m_{Z_1} is investigated in Fig. 46, where the respective other mass is fixed to the ideal value of 275 GeV. One can see that a light mass of the W_1 boson is crucial for unitarity, whereas the Z_1 mass can vary between $\approx 125 - 400$ GeV. In particular, a higgsless scenario with a $125 - 126$ GeV Z_1 boson (and a 275 GeV W_1 boson) can preserve unitarity. However, the newly discovered $125 - 126$ GeV resonance cannot be such a Z_1 boson, since its detection in the diphoton channel excludes a spin-1 resonance because of the Landau–Yang theorem, as mentioned before.

Now we move on to the scenario where two additional triplets of spin-1 states are present in the particle spectrum instead of only one. Within our framework (Sec. 4.1), this corresponds to parameters $\xi_i < 1$ ($i = W, Z$), whereas the special case $\xi_i = 1$ implies that just one additional vector-boson triplet is present, which was already discussed above. Fig. 47 shows the ξ_i-dependence of the largest eigenvalue. The masses of the second additional states are chosen as $m_{W_2} = m_{Z_2} = 550$ GeV, i.e. twice the mass of the first ones. This figure illustrates that including a second additional vector-boson triplet is not advantageous in terms of unitarity, since it impairs the high-energy behavior. Changing ξ_W has a larger impact than changing ξ_Z. The parameter ξ_W measures the fulfillment of the sum

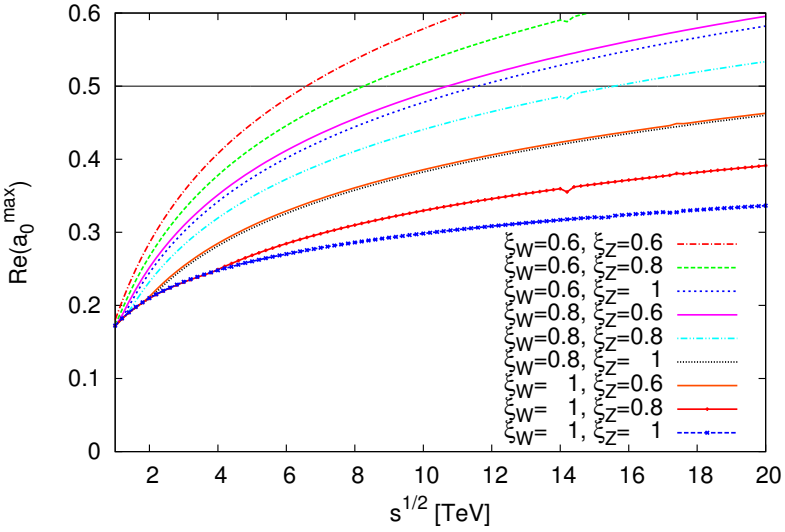

Figure 47: Dependence of the largest eigenvalue on ξ_i for $m_{W_1} = m_{Z_1} = 275$ GeV, $m_{W_2} = m_{Z_2} = 550$ GeV (ξ_i=1 corresponds to no second i boson).

rules (4.4) and (4.5) derived from $WZ \to WZ$ scattering (or $WW \to ZZ$, $ZZ \to WW$, respectively) by the W_1 boson. Therefore, these sum rules are even more important than the often discussed $WW \to WW$ sum rules (4.2) and (4.3) and have to be taken into account to give a reliable estimate of the scale of unitarity violation.

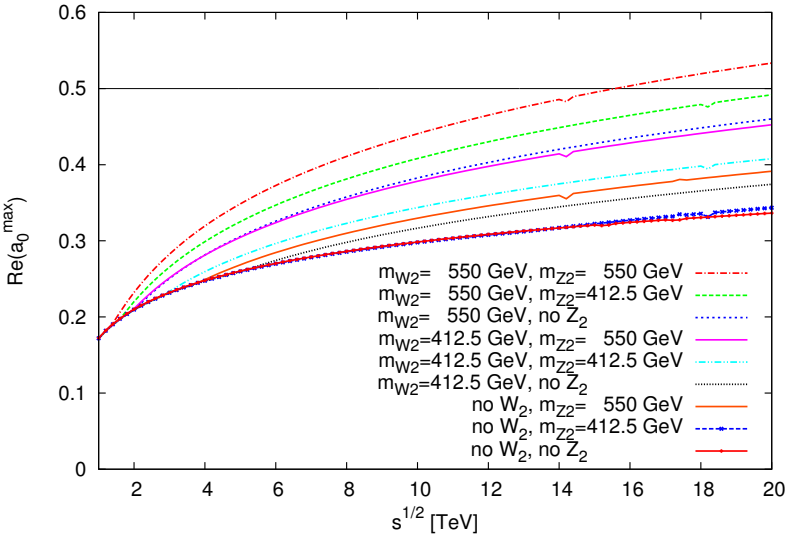

Figure 48: Dependence of the largest eigenvalue on m_{W_2} and m_{Z_2} for $m_{W_1} = m_{Z_1} = 275$ GeV, $\xi_i = 0.8$ (no second i boson corresponds to ξ_i=1).

This feature is also demonstrated by the larger impact of m_{W_1} than m_{Z_1} in Fig.46 and can be proven further by studying the dependence of the largest eigenvalue on the masses of the second spin-1 particles m_{W_2} and m_{Z_2}, which is shown in Fig. 48 for $m_{W_1} = m_{Z_1} = 275$ GeV. In case of a second resonance, ξ_i is chosen as 0.8. If no second resonance is present, ξ_i is equal to 1. Again, m_{W_2} has a greater influence than m_{Z_2}, so again the $WZ \to WZ$ sum rules are more important. Fig. 48 also demonstrates that the high-

energy behavior gets worse when the mass gap between the first and the second triplet is increased. The scenario with no W_2 and Z_2 bosons, but only one triplet of additional vector states is again the best choice for the preservation of unitarity.

From the Figures 45 - 48, we conclude that in scattering processes of weak SM bosons, unitarity can be restored for one additional triplet of light spin-1 states with masses around $m_{W_1} = m_{Z_1} \approx 150 - 300$ GeV, where the optimal mass value is ≈ 275 GeV. However, if such light additional weak bosons are present, one should investigate whether scattering processes involving these new bosons as external particles are also unitary. To this end, an extended set of sumrules for $W_iW_i \to W_jW_j$ and $W_iW_i \to Z_jZ_j$ was derived, where $i, j = 0, 1$, with 0 indicating a SM boson. The $W_iW_i \to W_jW_j$ case can also be found in Ref. [127] and the equations for $W_iW_i \to Z_jZ_j$ are

$$g_{W_iW_iZ_jZ_j} = \sum_{k=0}^{1} g^2_{W_kW_iZ_j} \tag{4.17}$$

$$2\,(M^2_{W_i} + M^2_{Z_j})\, g_{W_iW_iZ_jZ_j} = \sum_{k=0}^{1} \left(3M^2_{W_k} - \frac{(M^2_{W_i} - M^2_{Z_j})^2}{M^2_{W_k}} \right) g^2_{W_kW_iZ_j}. \tag{4.18}$$

We found that this extended set of sumrules cannot be fulfilled simultaneously. This implies that unitarity cannot be preserved in all channels, including the new vector states as external particles. Moreover, it was not even possible to find a configuration of couplings which postpones unitarity violation up to a reasonably high energy scale, neither via the above sumrules nor with randomly generated couplings. This observation agrees with the statement of Ref. [42], that scattering processes of the heaviest additional vector state cannot be unitarized unless an even heavier state is added, such that there is an infinite tower of modes in the end. Furthermore, it is consistent with the theorem by Cornwall et al. [135], which states that unitarity can only be preserved with scalar particles (if a finite number of particles is assumed). In case of the SM with a light Higgs boson, unitarity is preserved in the complete set of channels, including external Higgs bosons [104].

5 Summary

The discovery of the new $125-126$ GeV resonance at the LHC requires detailed studies of its properties, including its spin, in order to definitely verify or disprove whether it is the Higgs boson of the Standard Model. The observation of the resonance in the diphoton decay mode immediately excludes a spin-1 particle due to the Landau–Yang theorem, leaving spin-2 as an alternative hypothesis to the spin-0 of the Higgs boson. In order to distinguish these two possibilities, the phenomenology of light spin-2 resonances was studied in this work. Since the SM Higgs boson is mainly produced in gluon fusion or vector-boson fusion at the LHC, while the most important decay modes for its identification comprise $\gamma\gamma$, $W^+W^- \to 2l2\nu$ and $ZZ \to 4l$, these channels were investigated in most detail. For the present analysis of spin-2 resonances, an effective model for the interaction of a spin-2 electroweak singlet or triplet state with SM gauge bosons was implemented into the Monte Carlo program VBFNLO. This model features free coupling parameters, which can be tuned in order to adjust rates to those of the SM Higgs boson. Furthermore, it includes a formfactor that is multiplied with the amplitudes in order to parametrize high-energy contributions beyond the effective model and restore the unitarity of the S-matrix.

It was demonstrated that with a suitable choice of model parameters, a spin-2 resonance can indeed approximately reproduce SM Higgs rates in the considered channels. In spite of free spin-2 model parameters, this result is non-trivial, since the electroweak spin-2 couplings are related via an $SU(2) \times U(1)$ gauge symmetry. Likewise, transverse-momentum distributions of a spin-2 resonance can be adjusted to those of a SM Higgs boson by tuning formfactor parameters, leaving angular and invariant-mass distributions for a spin determination.
Different decay channels provide several observables that are particularly well suited to distinguish between spin-0 and spin-2. In the diphoton mode, scattering angles defined in specific frames clearly separate the two hypotheses, as long as no higher-dimensional spin-2 coupling structures are considered. Such structures can mimic angular distributions of the SM Higgs resonance for very specific values of the couplings, which, however, are quite unrealistic within the effective spin-2 framework.
In the $W^+W^- \to 2l2\nu$ decay, the invariant mass of the two charged leptons clearly distinguishes between a SM Higgs and a spin-2 resonance in VBF as well as in gluon fusion. Anomalous spin-0 scenarios, however, can lead to distributions which significantly differ

from those of the SM Higgs boson. Therefore, it is important to carefully disentangle spin, $\mathcal{CP}$ properties and tensor structures of the new resonance.
Although the four-lepton final state of the ZZ mode provides many observables that can be analyzed, a spin determination in this channel is intricate, since the difference between different spin-2 scenarios is larger than between a Higgs and a spin-2 resonance because of different contributions of intermediate photons and Z bosons. However, the ZZ mode can be useful to distinguish between particular choices of spin-2 couplings.
In order to complete the set of decay modes which involve spin-2 vertices and are accessible at the LHC, one should also consider the $Z\gamma$ channel and compare the spin-2 rate with current exclusion limits from LHC Higgs searches. Again, the SM Higgs rates including this channel can be approximately reproduced with a suitable choice of spin-2 model parameters, which also implies that there is no contradiction with current LHC data from the $Z\gamma$ mode. As in the ZZ channel, different contributions of intermediate photons and Z bosons strongly alter spin-2 distributions. However, the Gottfried–Jackson angle, defined as the angle between the momentum of the spin-2 particle or the Higgs boson in the laboratory frame and the final-state photon in the rest frame of the resonance, is a clear indicator of the spin.
In the VBF production mode, the two tagging jets in the final state give rise to further interesting observables. Particularly, the azimuthal angle difference between them was found to be an important variable to distinguish between spin-0 and spin-2. The characteristics of this distribution are nearly independent of spin-2 model parameters and decay modes. NLO QCD corrections are small for SM Higgs and spin-2 resonances in the VBF processes and have no impact on the characteristics of the differential distributions. In vector-boson fusion, the phenomenology of a neutral spin-2 triplet resonance resembles the one of the singlet particle, since its couplings to electroweak bosons features the same tensor structure. Also the triplet couplings can be adjusted to mimic the rates of the SM Higgs boson in $\gamma\gamma$, WW and ZZ decays. However, since there is no analog to the coupling of the singlet particle to two gluons, a SM Higgs boson in gluon fusion cannot be imitated by the spin-2 triplet.

Even if the $125-126$ GeV resonance is a spin-0 particle, new spin-2 resonances might exist at higher energies. Such heavy spin-2 resonances in VBF processes with four leptons and two jets in the final state were found to feature characteristic differential distribution as well, which can be utilized to identify a spin-2 resonance above the electroweak SM continuum. In the processes $pp \to VV\,jj \to e^+\,\nu_e\,\mu^+\mu^-\,jj$ and $pp \to VV\,jj \to e^-\,\overline{\nu}_e\,\mu^+\mu^-\,jj$,

only charged resonances are possible. Thus, they can be useful to distinguish between the spin-2 singlet and triplet scenarios.
As in case of light Higgs or spin-2 resonances, NLO QCD corrections are small in these VBF processes, both with and without heavy spin-2 resonances in addition to the electroweak SM continuum. The NLO QCD corrections lead to slightly enhanced cross sections with K-factors of approximately 1.05 and do no alter the differential distributions.

Another task of this thesis was to analyze the prospects of preserving the unitarity of the S-matrix in scattering processes of weak bosons by means of additional spin-2 or spin-1 particles instead of the spin-0 Higgs boson. In these cases, it is mandatory to consider not only longitudinal WW scattering, but all relevant combinations of initial and final-state bosons and polarizations together. It was found that by including a spin-2 particle, the preservation of unitarity is possible for longitudinal WW scattering if the spin-2 model parameters, including formfactor settings, are fine-tuned. However, it is not possible to restore the unitarity of all scattering channels of SM weak bosons simultaneously by including spin-2 particles.
From a theoretical perspective, spin-1 resonances with masses around 150 - 300 GeV were found to be a promising alternative. If only one additional triplet of vector states is included, the unitarity of SM weak-boson scattering can be preserved up to nearly arbitrary high energies. With more additional states, this is harder to achieve, but also possible for specific parameters and masses. Additionally, the often neglected sum rule stemming from WZ scattering was found to play a crucial role in deriving the scale of unitarity violation. However, simultaneous unitarization of a larger set of channels, containing also the additional spin-1 bosons as external particles, is not possible. Including both spin-1 and spin-2 resonances at the same time cannot restore unitarity either, since both of them contribute to the amplitudes with the same sign, which means that diverging contributions cannot cancel each other.

While rates and transverse-momentum distributions cannot definitely exclude the spin-2 hypothesis for the newly discovered $125-126$ GeV resonance, various angular and invariant-mass distributions allow for a spin determination. Corresponding experimental analyses by the ATLAS and CMS collaborations have already excluded specific spin-2 scenarios. Depending only little on spin-2 model parameters, such observables severely constrain the parameter space of spin-2 resonances, whereas experimental data obtained for the new particle are compatible with being the scalar Higgs boson of the Standard Model. The

finding that neither spin-1 nor spin-2 particles can completely mimic the ability of the SM Higgs boson for the preservation of unitarity in weak-boson scattering further confirms that indeed the SM Higgs boson has been discovered. Nevertheless, further experimental and theoretical effort is required in order to definitely prove this fundamental statement. This might be achieved by means of a future linear collider, which could allow for precision measurements of the Higgs boson properties.

Appendix

A Decay widths of the Spin-2 particles

This section provides explicit expressions for the partial decay widths of spin-2 singlet and triplet particles. Except for Γ_{gg} and $\Gamma_{\gamma\gamma}$ with higher-dimensional structures, they can also be found in Refs. [25, 69].
The total decay width of a spin-2 particle,

$$\Gamma_{\text{total}} = \sum_j \Gamma_j, \tag{A.1}$$

is the sum of the partial decay widths of all possible decay modes, which for two-body decays read [58]

$$\Gamma_j = \frac{|\vec{p}|}{8\pi m_T^2} |\mathcal{M}|^2. \tag{A.2}$$

Here, m_T is the mass of the spin-2 particle, $\mathcal{M}$ is the matrix element corresponding to a spin-2 particle decaying at rest, including an additional symmetry factor $\frac{1}{2}$ in case of identical decay products and $|\vec{p}|$ is the absolute value of the three-momenta of the two decay products in the rest frame of the resonance.

A.1 Spin-2 singlet

The explicit results for the partial decay widths Γ_j of the spin-2 singlet particle T are:

$$\begin{aligned}\Gamma_{W^+W^-} = \Bigg(& \frac{24 f_2^2 (m_T^4 - 3 m_T^2 m_W^2 + 6 m_W^4) + 40 f_2 f_5 g^2 v^2 (m_T^2 - m_W^2)}{12 \Lambda^2} \\ & + \frac{f_5^2 g^4 v^4 (m_T^4 + 12 m_T^2 m_W^2 + 56 m_W^4)}{96 \Lambda^2 m_W^4} \Bigg) \cdot \frac{\sqrt{(m_T^2/4 - m_W^2)}}{(40 \pi m_T^2)},\end{aligned} \tag{A.3}$$

$$\begin{aligned}\Gamma_{ZZ} = \Big(& [24 f_2^2 c_w^4 (m_T^4 - 3 m_T^2 m_Z^2 + 6 m_Z^4) + 8 c_w^2 f_2 (6 f_1 s_w^2 (m_T^4 - 3 m_T^2 m_Z^2 + 6 m_Z^4) \\ & + 5 f_5 v^2 (g^2 + g'^2)(m_T^2 - m_Z^2)) + 24 f_1^2 s_w^4 (m_T^4 - 3 m_T^2 m_Z^2 + 6 m_Z^4) \\ & + 40 f_1 f_5 s_w^2 v^2 (g^2 + g'^2)(m_T^2 - m_Z^2)] / (12 \Lambda^2) \\ & + \frac{f_5^2 v^4 (g^2 + g'^2)^2 (m_T^4 + 12 m_T^2 m_Z^2 + 56 m_Z^4)}{96 \Lambda^2 m_Z^4} \Big) \cdot \frac{\sqrt{m_T^2/4 - m_Z^2}}{80 \pi m_T^2},\end{aligned} \tag{A.4}$$

$$\Gamma_{\gamma Z} = \frac{c_w^2 s_w^2 (f_1 - f_2)^2 (m_T^2 - m_Z^2)^3 (6m_T^4 + 3m_T^2 m_Z^2 + m_Z^4)}{240\pi\Lambda^2 m_T^7}, \tag{A.5}$$

$$\begin{aligned}\Gamma_{\gamma\gamma} = \frac{m_T^3}{7680\,\pi\Lambda^6} \,(&96c_w^4 f_1^2\Lambda^4 + 48c_w^2 f_1\Lambda^2(4f_2\Lambda^2 s_w^2 - d_2 m_T^2) \\ &+ d_1^2 m_T^4 + 2d_1 m_T^4 d_2 + 7d_2^2 m_T^4 - 48 d_2 f_2 \Lambda^2 m_T^2 s_w^2 + 96 f_2^2 \Lambda^4 s_w^4),\end{aligned} \tag{A.6}$$

2005/06/28ver

$$\Gamma_{gg} = \frac{0.17\, f_9^2\, m_T^3}{\pi\Lambda^2}. \tag{A.7}$$

Note that Γ_{gg} contains a factor 1.7, which accounts for higher-order QCD corrections (see Sec. 3.2.3). $\Gamma_{\gamma\gamma}$ includes the higher-dimensional structures of Sec. 3.5. If they are neglected, i.e. their coefficients d_1 and d_2 are set to zero, it simplifies to

$$\Gamma_{\gamma\gamma,\,\mathrm{lowdim}} = \frac{(f_1 c_w^2 + f_2 s_w^2)^2 m_T^3}{80\pi\Lambda^2}. \tag{A.8}$$

The total decay width is obtained by adding up all partial widths where the mass of the spin-2 particle is larger than the sum of the final-state particle masses. However, there might be additional (and possibly hard to detect) decay modes of the spin-2 particle, which are not considered in the present model, leading to a larger total width. This is taken into account by introducing an additional branching ratio parameter b, which is the fraction of the considered decays over all possible ones. This parameter has to be greater than zero and less than or equal to one, where $b = 1$ indicates that no additional decay modes exist. Then, the total width is

$$\Gamma_{\mathrm{total}} = \frac{1}{b}\left(\Gamma_{W^+W^-} + \Gamma_{ZZ} + \Gamma_{\gamma Z} + \Gamma_{\gamma\gamma} + \Gamma_{gg}\right). \tag{A.9}$$

By modifying the parameter b, the width of a spin-2 resonance could also be varied in order to mimic a SM Higgs boson. However, the precise value of the width, which is very small for the parameters considered here, is not relevant for the present analysis. Therefore, b is set to one here.

A.2 Spin-2 triplet

For the decay width of the neutral and charged spin-2 triplet particles, the same definitions are applied. The parameter b can differ from the singlet case and can be different for the neutral and the charged particles, yet it is set to 1 in the present analysis for all cases. The resulting partial decay widths for the neutral particle are:

$$\Gamma_{W^+W^-} = \frac{f_6^2 g^4 v^4 (m_T^4 + 12 m_T^2 m_W^2 + 56 m_W^4)}{384 \Lambda^2 m_W^4} \cdot \frac{\sqrt{m_T^2/4 - m_W^2}}{40\pi m_T^2}, \tag{A.10}$$

$$\begin{aligned}\Gamma_{ZZ} = \big(\big(&768 f_7^2 c_w^2 s_w^2 m_Z^4 (m_T^4 - 3 m_T^2 m_Z^2 + 6 m_Z^4) + 640 c_w f_6 f_7 m_Z^4 s_w v^2 \\ &(g^2 + g'^2)(m_T^2 - m_Z^2) + f_6^2 v^4 (g^2 + g'^2)^2 (m_T^4 + 12 m_T^2 m_Z^2 + 56 m_Z^4)\big) \\ &/(384 \Lambda^2 m_Z^4)\big) \cdot \frac{\sqrt{m_T^2/4 - m_Z^2}}{80\pi m_T^2},\end{aligned} \tag{A.11}$$

$$\Gamma_{\gamma\gamma} = \frac{f_7^2 c_w^2 s_w^2 m_T^3}{80\pi\Lambda^2}, \tag{A.12}$$

$$\Gamma_{\gamma Z} = \frac{f_7^2 (c_w^2 - s_w^2)^2 (m_T^2 - m_Z^2)^3 (6 m_T^4 + 3 m_T^2 m_Z^2 + m_Z^4)}{960\pi\Lambda^2 m_T^7}. \tag{A.13}$$

Here, m_T denotes the mass of the neutral spin-2 triplet particle.

The partial decay widths of the charged spin-2 particles are:

$$\Gamma_{W\gamma} = \frac{f_7^2 c_w^2 (m_T^2 - m_W^2)^3 (6 m_T^4 + 3 m_T^2 m_W^2 + m_W^4)}{960\pi\Lambda^2 m_T^7}, \tag{A.14}$$

$$\begin{aligned}\Gamma_{WZ} = &((m_T^2 m_W^2 (m_T^2 m_Z^2 (13 f_6^2 g^2 v^4 (g^2 + g'^2) + 256 f_7^2 m_W^2 m_Z^2 s_w^2) \\ &+ 1/4 (m_T^2 - m_W^2 + m_Z^2)^2 (7 f_6^2 g^2 v^4 (g^2 + g'^2) - 96 f_7^2 m_W^2 m_Z^2 s_w^2)) \\ &+ 1/4 (m_T^2 + m_W^2 - m_Z^2)^2 (m_T^2 m_Z^2 (7 f_6^2 g^2 v^4 (g^2 + g'^2) - 96 f_7^2 m_W^2 m_Z^2 s_w^2) \\ &+ (m_T^2 - m_W^2 + m_Z^2)^2 (f_6^2 g^2 v^4 (g^2 + g'^2) + 32 f_7^2 m_W^2 m_Z^2 s_w^2)) \\ &+ m_T^2 (m_T^2 - m_W^2 - m_Z^2)(1/4 (m_T^2 + m_W^2 - m_Z^2)(m_T^2 - m_W^2 + m_Z^2) \\ &(128 f_7^2 m_W^2 m_Z^2 s_w^2 - f_6^2 g^2 v^4 (g^2 + g'^2)) + 40 f_6 f_7 g m_T^2 m_W^2 m_Z^2 s_w v^2 \sqrt{g^2 + g'^2}) \\ &+ 1/4 m_T^4 (-m_T^2 + m_W^2 + m_Z^2)^2 (f_6^2 g^2 v^4 (g^2 + g'^2) + 32 f_7^2 m_W^2 m_Z^2 s_w^2) \\ &+ 40 f_6 f_7 g m_T^2 m_W^2 m_Z^2 s_w v^2 \sqrt{g^2 + g'^2} (m_T^2 + m_W^2 - m_Z^2) \\ &(m_T^2 - m_W^2 + m_Z^2))/(96 \Lambda^2 m_T^4 m_W^2 m_Z^2)) \\ &\cdot \frac{\sqrt{(m_T^2 - m_W^2 - m_Z^2)^2 - 4 m_W^2 m_Z^2}}{80\pi m_T^3},\end{aligned} \tag{A.15}$$

with m_T now being the mass of the charged spin-2 triplet particles.

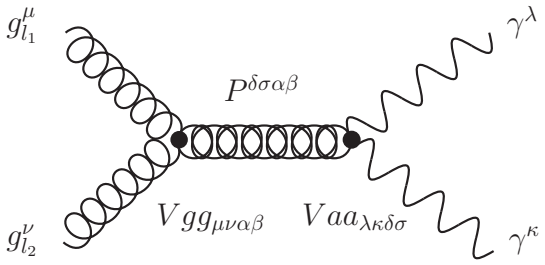

Figure 49: Illustration of a calculation involving a spin-2 particle in $gg \to \gamma\gamma$.

B Calculation of Spin-2 diagrams

This section illustrates the calculation of amplitudes corresponding to Feynman diagrams with spin-2 particles. One way to calculate such amplitudes consists of calls of HELAS routines, which contain the Feynman rules of the spin-2 model (see Sec. 3.1). There are two different kinds of spin-2 HELAS routines for each combination of bosons which couple to the spin-2 particle: those which calculate an off-shell tensor current and those which calculate a vertex. Furthermore, each spin-2 particle (the singlet particle T, the neutral triplet particle T^0 and the charged triplet particles $T^{\pm}$) has its own set of routines. As an example, consider a spin-2 singlet resonance produced in gluon fusion and decaying into two photons (Fig. 49). The corresponding amplitude for given gluon polarizations l_1 and l_2 can be written as

$$i\,\mathcal{M}(l_1,l_2) \propto g^{\mu}_{l_1} g^{\nu}_{l_2}\,\mathrm{Vgg}_{\mu\nu\alpha\beta}\,P^{\delta\sigma\alpha\beta}\,\mathrm{Vaa}_{\lambda\kappa\delta\sigma}\,\gamma_1^{\lambda}\gamma_2^{\kappa}. \tag{B.1}$$

Here, g (γ) are the polarization vectors of gluons (photons), Vgg(aa) denotes the Tgg ($T\gamma\gamma$) vertex and P is the spin-2 propagator. For the final-state photons, random helicities are used. From right to left, the off-shell tensor current is calculated first from the final photons via a call of the HELAS routine UAAXXX_SING_HIGHDIM(a1,a2 , uaa), which calculates the tensor current

$$\begin{aligned} yaa^{\alpha\beta} &= P^{\delta\sigma\alpha\beta}\,\mathrm{Vaa}_{\lambda\kappa\delta\sigma}\,\gamma_1^{\lambda}\gamma_2^{\kappa} \\ &= -\frac{B^{\delta\sigma\alpha\beta}}{k^2 - m_T^2 + i m_T \Gamma_T}\,\left(\frac{2\,(f_1 c_w^2 + f_2 s_w^2)}{\Lambda} K_{1,\,\lambda\kappa\delta\sigma} + \frac{1}{\Lambda^3} K_{3,\,\lambda\kappa\delta\sigma}\right)\,\gamma_1^{\lambda}\,\gamma_2^{\kappa}. \end{aligned} \tag{B.2}$$

$B^{\delta\sigma\alpha\beta}, K_{1,\,\lambda\kappa\delta\sigma}$ and $K_{3,\,\lambda\kappa\delta\sigma}$ are defined in Eqs. (3.14), (3.10) and (3.40). m_T denotes the mass of the spin-2 particle with momentum k and width Γ_T (see Appendix A). The input of UAAXXX_SING_HIGHDIM(a1,a2 , uaa) consists of complex functions a1 and a2 with six

components, which, apart from the photon polarizations, contain their four-momenta in the fifth and sixth component. The 16 entries of yaa are stored in the first 16 components of the output uaa. This complex output additionally contains the momentum of the spin-2 particle in the 17th and 18th component, which is calculated by adding the four-momenta of the two photons.
Then, the result uaa is used as an input tc for the vertex routine GGTXXX_SING(g1,g2,tc , amp), which calculates the amplitude for specific gluon polarizations:

$$\text{amp} = g^{\mu}_{l_1} g^{\nu}_{l_2} \, \text{Vgg}_{\mu\nu\alpha\beta} \, yaa^{\alpha\beta} = \frac{2 f_9}{\Lambda} K_{1,\,\mu\nu\alpha\beta} \; g^{\mu}_{l_1} \, g^{\nu}_{l_2} \, yaa^{\alpha\beta}. \tag{B.3}$$

Afterwards, the results amp, which depend on the gluon polarizations l_1 and l_2, are multiplied with the formfactor (3.15), squared and added up. The square of the matrix element is finally provided with a factor $\frac{1}{2^2 \cdot 8^2}$ for the average over the polarizations and colors of the two initial gluons and a factor 8 from the color delta of the Tgg vertex.

The calculation with HELAS routines features a clear modular structure. However, the code is slow in case of spin-2 particles, since the automated contraction of many indices via nested do loops is not very efficient. Therefore, a second method was implemented, which also served as a check. In this fast code, most of the indices of Eq. (B.1) were contracted beforehand and expressions were simplified. The corresponding routine GGSP2TOVV(idfsvv,p1,p2,q1,q2,eps1,eps2 , ggsp2vv) in case of gluon fusion calculates the output

$$\text{ggsp2vv}_{\mu\nu} = t_{11,\,\mu\nu} \, \frac{4 f_9 (f_1 c_w^2 + f_2 s_w^2)}{\Lambda^2} \tag{B.4}$$

for a spin-2 singlet resonance in the diphoton channel without higher-dimensional structures. $t_{11,\,\mu\nu}$ is the sum of many terms resulting from contractions of γ_1^{λ}, γ_2^{κ} and the various terms in $\text{Vgg}_{\mu\nu\alpha\beta}$, $B^{\delta\sigma\alpha\beta}$ and $\text{Vaa}_{\lambda\kappa\delta\sigma}$, which comprise components of four-momenta and the metric tensor. One of these terms is e.g.

$$6\, m_T^4 \, ((p1 + p2) \cdot \text{eps2}) \, ((p1 + p2)^2 - (p1 - p2)^2) \, \text{eps1}_{\mu} \, (q1_{\nu} - q2_{\nu}). \tag{B.5}$$

Furthermore, $t_{11,\,\mu\nu}$ contains the formfactor and the denominator of the spin-2 propagator. The input of the routine GGSP2TOVV(idfsvv,p1,p2,q1,q2,eps1,eps2 , ggsp2vv) consists of the incoming momenta of the two gluons p1 and p2, the outgoing momenta of the two final bosons q1 and q2 and the polarization vectors of the final bosons eps1 and eps2, which in case of further decays are replaced by the currents from final-state leptons. idfsvv

specifies the final-state bosons (e.g. 1 for two photons, 2 for two W bosons etc). The output ggsp2vv$_{\mu\nu}$ is then contracted with $g^{\mu}_{l_1} g^{\nu}_{l_2}$. As before, the contributions of different gluon polarizations are finally squared, added up and polarization and color factors are included in the square of the matrix element.

Both methods, which were exemplified for gluon fusion here, were also applied to spin-2-resonant vector-boson-fusion processes. The main difference is that in this case, leptonic tensors $\mathcal{L}_{\mu\nu}$ are calculated instead of the full amplitudes. They are then contracted with the currents from the two quarks according to Eq. (3.18).

Bibliography

[1] B. Odom, D. Hanneke, B. D'Urso, and G. Gabrielse, Phys. Rev. Lett. **97**, 030801 (2006).

[2] G. Aad *et al.* [ATLAS Collaboration], Phys. Lett. B **716** (2012) 1; S. Chatrchyan *et al.* [CMS Collaboration], Phys. Lett. B **716** (2012) 30.

[3] G. Aad *et al.* [ATLAS Collaboration], Phys. Lett. B **726** (2013) 88; ATLAS-CONF-2013-034.

[4] G. Aad *et al.* [ATLAS Collaboration], Phys. Lett. B **726** (2013) 120; ATLAS-CONF-2013-040.

[5] ATLAS Collaboration, ATLAS-CONF-2013-013.

[6] ATLAS Collaboration, ATLAS-CONF-2013-029.

[7] ATLAS Collaboration, ATLAS-CONF-2013-031.

[8] S. Chatrchyan *et al.* [CMS Collaboration], Phys. Rev. Lett. **110** (2013) 081803.

[9] CMS Collaboration, CMS PAS HIG-13-002.

[10] S. Chatrchyan *et al.* [CMS Collaboration], arXiv:1312.1129 [hep-ex]; CMS PAS HIG-13-003.

[11] CMS Collaboration, CMS PAS HIG-13-005.

[12] CMS Collaboration, CMS PAS HIG-13-016.

[13] P. W. Higgs, Phys. Lett. **12**, 132 (1964), Phys. Rev. Lett. **13**, 508 (1964), Phys. Rev. **145**, 1156 (1966); F. Englert and R. Brout, Phys. Rev. Lett. **13**, 321 (1964); G. S. Guralnik, C. R. Hagen and T. W. B. Kibble, Phys. Rev. Lett. **13**, 585 (1964).

[14] D. Zeppenfeld, R. Kinnunen, A. Nikitenko and E. Richter-Was, Phys. Rev. D **62**, 013009 (2000); M. Dührssen, S. Heinemeyer, H. Logan, D. Rainwater, G. Weiglein and D. Zeppenfeld, Phys. Rev. D **70**, 113009 (2004) and hep-ph/0407190; V. Hankele, G. Klämke, D. Zeppenfeld and T. Figy, Phys. Rev. D **74** (2006) 095001; R. Lafaye, T. Plehn, M. Rauch, D. Zerwas and M. Dührssen, JHEP **0908**, 009 (2009); M. Rauch,

arXiv:1110.1196 [hep-ph]; F. Bonnet, M. B. Gavela, T. Ota and W. Winter, Phys. Rev. D **85**, 035016 (2012); D. Carmi, A. Falkowski, E. Kuflik and T. Volansky, JHEP **1207**, 136 (2012) and Frascati Phys. Ser. **57** (2013) 315; D. Carmi, A. Falkowski, E. Kuflik, T. Volansky and J. Zupan, JHEP **1210** (2012) 196; P. P. Giardino, K. Kannike, M. Raidal and A. Strumia, JHEP **1206**, 117 (2012) and Phys. Lett. B **718** (2012) 469; J. Ellis and T. You, JHEP **1206**, 140 (2012) and JHEP **1209**, 123 (2012); J. R. Espinosa, C. Grojean, M. Mühlleitner and M. Trott, JHEP **1205** (2012) 097, JHEP **1209**, 126 (2012) and JHEP **1212** (2012) 045; A. Azatov, R. Contino and J. Galloway, JHEP **1204**, 127 (2012); A. Azatov, R. Contino, D. Del Re, J. Galloway, M. Grassi and S. Rahatlou, JHEP **1206**, 134 (2012); M. Klute, R. Lafaye, T. Plehn, M. Rauch and D. Zerwas, Phys. Rev. Lett. **109**, 101801 (2012); T. Corbett, O. J. P. Eboli, J. Gonzalez-Fraile and M. C. Gonzalez-Garcia, Phys. Rev. D **86** (2012) 075013; R. S. Gupta, H. Rzehak and J. D. Wells, Phys. Rev. D **86**, 095001 (2012); S. Banerjee, S. Mukhopadhyay and B. Mukhopadhyaya, JHEP **1210** (2012) 062; F. Bonnet, T. Ota, M. Rauch and W. Winter, Phys. Rev. D **86** (2012) 093014; T. Plehn and M. Rauch, Europhys. Lett. **100** (2012) 11002; A. Djouadi, Eur. Phys. J. C **73** (2013) 2498; J. Ellis, V. n. Sanz and T. You, Eur. Phys. J. C **73** (2013) 2507; B. A. Dobrescu and J. D. Lykken, JHEP **1302** (2013) 073; E. Masso and V. Sanz, Phys. Rev. D **87** (2013) 3, 033001; R. Contino, M. Ghezzi, C. Grojean, M. Mühlleitner and M. Spira, JHEP **1307** (2013) 035.

[15] A. Djouadi, W. Kilian, M. Mühlleitner and P. M. Zerwas, Eur. Phys. J. C **10**, 27 (1999) and Eur. Phys. J. C **10**, 45 (1999); M. M. Mühlleitner, hep-ph/0008127; U. Baur, T. Plehn and D. L. Rainwater, Phys. Rev. Lett. **89**, 151801 (2002), Phys. Rev. D **67**, 033003 (2003); and Phys. Rev. D **69**, 053004 (2004); A. Dahlhoff, arXiv:hep-ex/0505022; T. Plehn and M. Rauch, Phys. Rev. D **72**, 053008 (2005); T. Binoth, S. Karg, N. Kauer and R. Rückl, Phys. Rev. D **74**, 113008 (2006); M. J. Dolan, C. Englert and M. Spannowsky, JHEP **1210** (2012) 112; A. Papaefstathiou, L. L. Yang and J. Zurita, Phys. Rev. D **87** (2013) 011301; J. Baglio, A. Djouadi, R. Gröber, M. M. Mühlleitner, J. Quevillon and M. Spira, JHEP **1304** (2013) 151; F. Goertz, A. Papaefstathiou, L. L. Yang and J. Zurita, arXiv:1301.3492 [hep-ph]; J. Grigo, J. Hoff, K. Melnikov and M. Steinhauser, Nucl. Phys. B **875** (2013) 1.

[16] T. Plehn, D. L. Rainwater and D. Zeppenfeld, Phys. Rev. Lett. **88**, 051801 (2002).

[17] S. Y. Choi, D. J. Miller, M. M. Mühlleitner and P. M. Zerwas, Phys. Lett. B **553** (2003) 61.

[18] K. Hagiwara, Q. Li and K. Mawatari, JHEP **0907**, 101 (2009).

[19] Y. Gao, A. V. Gritsan, Z. Guo, K. Melnikov, M. Schulze and N. V. Tran, Phys. Rev. D **81** (2010) 075022.

[20] S. Bolognesi, Y. Gao, A. V. Gritsan, K. Melnikov, M. Schulze, N. V. Tran and A. Whitbeck, Phys. Rev. D **86** (2012) 095031.

[21] J. Ellis and D. S. Hwang, JHEP **1209**, 071 (2012); J. Ellis, R. Fok, D. S. Hwang, V. Sanz and T. You, Eur. Phys. J. C **73** (2013) 2488.

[22] J. Ellis, V. Sanz and T. You, Phys. Lett. B **726** (2013) 244.

[23] S. Y. Choi, M. M. Mühlleitner and P. M. Zerwas, Phys. Lett. B **718** (2013) 1031.

[24] C. Englert, D. Goncalves-Netto, K. Mawatari and T. Plehn, JHEP **1301** (2013) 148.

[25] J. Frank, M. Rauch and D. Zeppenfeld, Phys. Rev. **D87**, 055020 (2013) [arXiv:1211.3658 [hep-ph]].

[26] J. Frank, M. Rauch and D. Zeppenfeld, arXiv:1305.1883 [hep-ph].

[27] D. J. Miller, 2, S. Y. Choi, B. Eberle, M. M. Mühlleitner and P. M. Zerwas, Phys. Lett. B **505** (2001) 149; K. Odagiri, JHEP **0303** (2003) 009; C. P. Buszello, I. Fleck, P. Marquard and J. J. van der Bij, Eur. Phys. J. C **32**, 209 (2004); C. P. Buszello and P. Marquard, hep-ph/0603209; V. Hankele, G. Klämke and D. Zeppenfeld, arXiv:hep-ph/0605117; G. Klämke and D. Zeppenfeld, JHEP **0704** (2007) 052 and arXiv:0705.2983 [hep-ph]; R. M. Godbole, D. J. Miller, 2 and M. M. Mühlleitner, JHEP **0712** (2007) 031; C. Ruwiedel, N. Wermes and M. Schumacher, Eur. Phys. J. C **51**, 385 (2007); S. Berge, W. Bernreuther and J. Ziethe, Phys. Rev. Lett. **100**, 171605 (2008); S. Berge and W. Bernreuther, Phys. Lett. B **671**, 470 (2009); N. D. Christensen, T. Han and Y. Li, Phys. Lett. B **693** (2010) 28; A. De Rujula, J. Lykken, M. Pierini, C. Rogan and M. Spiropulu, Phys. Rev. D **82** (2010) 013003; C. Englert, C. Hackstein and M. Spannowsky, Phys. Rev. D **82** (2010) 114024; S. Berge, W. Bernreuther, B. Niepelt, H. Spiesberger, Phys. Rev. D **84** (2011) 116003; F. Campanario, M. Kubocz and D. Zeppenfeld, Phys. Rev. D **84**, 095025 (2011); U. De Sanctis, M. Fabbrichesi and A. Tonero, Phys. Rev. D **84** (2011) 015013; C. Englert,

M. Spannowsky and M. Takeuchi, JHEP **1206**, 108 (2012); D. Stolarski and R. Vega-Morales, Phys. Rev. D **86** (2012) 117504; A. Alves, Phys. Rev. D **86** (2012) 113010; R. Boughezal, T. J. LeCompte and F. Petriello, arXiv:1208.4311 [hep-ph]; J. Ellis, D. S. Hwang, V. Sanz and T. You, JHEP **1211** (2012) 134; J. Kumar, A. Rajaraman and D. Yaylali, Phys. Rev. D **86** (2012) 115019; C. -Q. Geng, D. Huang, Y. Tang and Y. -L. Wu, Phys. Lett. B **719** (2013) 164; A. Freitas and P. Schwaller, Phys. Rev. D **87** (2013) 055014; D. Boer, W. J. d. Dunnen, C. Pisano and M. Schlegel, Phys. Rev. Lett. **111** (2013) 032002; S. Banerjee, J. Kalinowski, W. Kotlarski, T. Przedzinski and Z. Was, Eur. Phys. J. C **73** (2013) 2313; C. Englert, D. Goncalves, G. Nail and M. Spannowsky, Phys. Rev. D **88** (2013) 013016; A. Djouadi, R. M. Godbole, B. Mellado and K. Mohan, Phys. Lett. B **723** (2013) 307; P. Artoisenet, P. de Aquino, F. Demartin, R. Frederix, S. Frixione, F. Maltoni, M. K. Mandal and P. Mathews *et al.*, JHEP **1311** (2013) 043; T. Modak, D. Sahoo, R. Sinha and H. -Y. Cheng, arXiv:1301.5404 [hep-ph]; R. Godbole, D. J. Miller, K. Mohan and C. D. White, arXiv:1306.2573 [hep-ph].

[28] L. D. Landau, Dokl. Akad. Nawk., USSR 60, 207 (1948); C. N. Yang, Phys. Rev. **77**, 242 (1950).

[29] K. Arnold, J. Bellm, G. Bozzi, F. Campanario, C. Englert, B. Feigl, J. Frank and T. Figy *et al.*, arXiv:1207.4975 [hep-ph]; K. Arnold, J. Bellm, G. Bozzi, M. Brieg, F. Campanario, C. Englert, B. Feigl, J. Frank *et al.*, [arXiv:1107.4038 [hep-ph]]; K. Arnold, M. Bahr, G. Bozzi, F. Campanario, C. Englert, T. Figy, N. Greiner and C. Hackstein *et al.*, Comput. Phys. Commun. **180** (2009) 1661.

[30] C. Englert, B. Jager, D. Zeppenfeld, JHEP **0903** (2009) 060.

[31] C. H. Llewellyn Smith, Phys. Lett. B **46**, 233 (1973); D. A. Dicus and V. S. Mathur, Phys. Rev. D **7**, 3111 (1973); J. M. Cornwall, D. N. Levin and G. Tiktopoulos, Phys. Rev. Lett. **30**, 1268 (1973) [Erratum-ibid. **31**, 572 (1973)] and Phys. Rev. D **10**, 1145 (1974) [Erratum-ibid. D **11**, 972 (1975)].

[32] A. Djouadi, Phys. Rept. **457** (2008) 1.

[33] S. Dittmaier and M. Schumacher, Prog. Part. Nucl. Phys. **70** (2013) 1 [arXiv:1211.4828 [hep-ph]].

[34] A. Denner, Fortsch. Phys. **41** (1993) 307.

[35] S. Troitsky, Phys. Usp. **55** (2012) 72 [Usp. Fiz. Nauk **182** (2012) 77].

[36] M. Gomez-Bock, M. Mondragon, M. Mühlleitner, M. Spira and P. M. Zerwas, arXiv:0712.2419 [hep-ph].

[37] K. Lane, hep-ph/0202255.

[38] J. Wess and B. Zumino, Nucl. Phys. B **70** (1974) 39.

[39] K. Inonue, A. Kakuto, H. Komatsu and S. Takeshita, Prog. Theor. Phys. **67** (1982) 1889; R. Flores and M. Sher, Ann. Phys. **148** (1983) 95; H.P. Nilles and M. Nusbaumer, Phys. Lett. B **145** (1984) 73; P. Majumdar and P. Roy, Phys. Rev. D **30** (1984) 2432.

[40] P. Fayet, Nucl. Phys. B **90** (1975) 104; H.-P. Nilles, M. Srednicki and D. Wyler, Phys. Lett. B **120** (1983) 346; J.-P. Derendinger and C.A. Savoy, Nucl. Phys. B **237** (1984) 307; J.F. Gunion and H.E. Haber, Nucl. Phys. B **272** (1986) 1; J. Ellis, J.F. Gunion, H.E. Haber, L. Roszkowski and F. Zwirner, Phys. Rev. D **39** (1989) 844; U. Ellwanger, M. Rausch de Traubenberg and C.A. Savoy, Z. Phys. C **67** (1995) 665; S.F. King and P.L. White, Phys. Rev. D **52** (1995) 4183; H. Asatrian and K. Eguin, Mod. Phys. Lett. A **10** (1995) 2943; D.J. Miller, R. Nevzorov and P.M. Zerwas, Nucl. Phys. B **681** (2004) 3; S.Y. Choi, D.J. Miller and P.M. Zerwas, Nucl. Phys. B **711** (2005) 83.

[41] T. Kaluza, Sitzungsber. Preuss. Akad. Wiss. Berlin (Math. Phys.) 1921 (1921) 966972; O. Klein, Z. Phys. **37** (1926) 895906; L. Randall and R. Sundrum, Phys. Rev. Lett. **83** (1999) 3370; L. Randall and R. Sundrum, Phys. Rev. Lett. **83** (1999) 4690; N. Arkani-Hamed, S. Dimopoulos and G. R. Dvali, Phys. Lett. B **429** (1998) 263.

[42] C. Csaki, C. Grojean, H. Murayama, L. Pilo and J. Terning, Phys. Rev. D **69** (2004) 055006 [arXiv:hep-ph/0305237].

[43] N. Arkani-Hamed, A. G. Cohen and H. Georgi, Phys. Rev. Lett. **86**, 4757 (2001).

[44] J. J. van der Bij, Phys. Lett. B **636** (2006) 56 [hep-ph/0603082].

[45] H. Georgi, Phys. Rev. Lett. **98** (2007) 221601 [hep-ph/0703260].

[46] J. J. van der Bij and B. Pulice, Nucl. Phys. B **853** (2011) 49.

[47] J. J. van der Bij and S. Dilcher, Phys. Lett. B **655** (2007) 183.

[48] N. Arkani-Hamed, A. G. Cohen and H. Georgi, Phys. Lett. B **513** (2001) 232.

[49] K. Agashe, R. Contino and A. Pomarol, Nucl. Phys. B **719** (2005) 165.

[50] J. M. Maldacena, Adv. Theor. Math. Phys. **2** (1998) 231.

[51] G. Landsberg, arXiv:1310.0025 [hep-ex].

[52] S. Dawson, A. Gritsan, H. Logan, J. Qian, C. Tully, R. Van Kooten, A. Ajaib and A. Anastassov *et al.*, arXiv:1310.8361 [hep-ex].

[53] S. Heinemeyer *et al.* [LHC Higgs Cross Section Working Group Collaboration], arXiv:1307.1347 [hep-ph].

[54] LHC Higgs Cross Section Working Group, https://twiki.cern.ch/twiki/bin/view/LHCPhysics/CrossSectionsFigures.

[55] P. Skands, arXiv:1207.2389 [hep-ph].

[56] J. C. Collins and D. E. Soper, Nucl. Phys. B **194** (1982) 445.

[57] D. Zeppenfeld, hep-ph/9902307.

[58] M. E. Peskin and D. V. Schroeder, "An Introduction to Quantum Field Theory", Westview Press (1995).

[59] Y. L. Dokshitzer, Sov. Phys. JETP **46** (1977) 641 [Zh. Eksp. Teor. Fiz. **73** (1977) 1216]; V. N. Gribov and L. N. Lipatov, Sov. J. Nucl. Phys. **15** (1972) 438 [Yad. Fiz. **15** (1972) 781]; G. Altarelli and G. Parisi, Nucl. Phys. B **126** (1977) 298.

[60] S. Weinzierl, hep-ph/0006269.

[61] G. P. Lepage, J. Comp. Phys. **27** (1978) 192; G. P. Lepage, Cornell preprint (1980) CLNS-80/447.

[62] W. Siegel, Phys. Lett. B **84**, 193 (1979); W. Siegel, Phys. Lett. B **94**, 37 (1980).

[63] T. Kinoshita, J. Math. Phys. **3** (1962) 650; T. D. Lee and M. Nauenberg, Phys. Rev. **133** (1964) B1549.

[64] S. Catani and M. H. Seymour, Nucl. Phys. B **485** (1997) 291 [Erratum-ibid. B **510** (1998) 503].

[65] G. Velo and D. Zwanziger, Phys. Rev. **186** (1969) 1337, Phys. Rev. **188** (1969) 2218; G. Velo, Nucl. Phys. B **43** (1972) 389.

[66] M. Porrati, R. Rahman and A. Sagnotti, Nucl. Phys. B **846** (2011) 250.

[67] M. Porrati and R. Rahman, Nucl. Phys. B **801** (2008) 174.

[68] C. Burgess, G. Moore: "The Standard Model: A Primer"; W. Buchmller, D. Wyler, Nucl. Phys. B268 (1986) 621.

[69] J. Frank, "Spin-2 Resonances in Vector Boson Fusion Processes at the LHC", Diploma thesis (http://www.itp.kit.edu/diplomatheses.de.shtml).

[70] M. Fierz, Helv. Phys. Acta **12**, 3 (1939); M. Fierz and W. Pauli, Proc. Roy. Soc. Lond. A **173**, 211 (1939); H. van Dam and M. J. G. Veltman, Nucl. Phys. B **22**, 397 (1970).

[71] K. Hagiwara, J. Kanzaki, Q. Li and K. Mawatari, Eur. Phys. J. C **56**, 435 (2008).

[72] G. F. Giudice, R. Rattazzi and J. D. Wells, Nucl. Phys. B **544**, 3 (1999).

[73] T. Figy and D. Zeppenfeld, Phys. Lett. B **591** (2004) 297.

[74] B. Jager, C. Oleari, D. Zeppenfeld, JHEP **0607** (2006) 015.

[75] B. Jager, C. Oleari, D. Zeppenfeld, Phys. Rev. D **73** (2006) 113006.

[76] G. Bozzi, B. Jager, C. Oleari, D. Zeppenfeld, Phys. Rev. D **75** (2007) 073004.

[77] H. Murayama and I. Watanabe and K. Hagiwara, KEK-91-11.

[78] T. Figy, C. Oleari, D. Zeppenfeld, Phys. Rev. D **68** (2003) 073005.

[79] A. Denner and S. Dittmaier, Nucl. Phys. B **734**, 62 (2006).

[80] G. Passarino, M. J. Veltman, Nucl. Phys. B **160**, 151 (1979).

[81] J. Alwall, P. Demin, S. de Visscher, R. Frederix, M. Herquet, F. Maltoni, T. Plehn, D. L. Rainwater *et al.*, JHEP **0709** (2007) 028.

[82] C. Oleari, D. Zeppenfeld, Phys. Rev. D **69** (2004) 093004.

[83] A. Denner, S. Dittmaier, M. Roth, D. Wackeroth, Nucl. Phys. B **560** (1999) 33.

[84] E. W. N. Glover and J. J. van der Bij, Phys. Lett. B **219** (1989) 488; C. Kao and D. A. Dicus, Phys. Rev. D **43** (1991) 1555; T. Binoth, M. Ciccolini, N. Kauer and M. Kramer, JHEP **0503** (2005) 065; T. Binoth, M. Ciccolini, N. Kauer and M. Kramer, JHEP **0612** (2006) 046; E. W. N. Glover and J. J. van der Bij, Nucl. Phys. B **321** (1989) 561; T. Binoth, N. Kauer and P. Mertsch, arXiv:0807.0024 [hep-ph]; T. Binoth, J. P. Guillet, E. Pilon and M. Werlen, Eur. Phys. J. C **16** (2000) 311.

[85] J. Kublbeck, M. Bohm, A. Denner, Comput. Phys. Commun. **60** (1990) 165.

[86] T. Hahn and M. Perez-Victoria, Comput. Phys. Commun. **118** (1999) 153.

[87] S. Dawson, Nucl. Phys. B **359** (1991) 283; D. Graudenz, M. Spira, and P. Zerwas, Phys. Rev. Lett. **70** (1993) 1372; R. V. Harlander, Phys. Lett. B **492** (2000) 74; S. Catani, D. de Florian, and M. Grazzini, JHEP **05** (2001) 025; R. V. Harlander and W. B. Kilgore, Phys. Rev. D **64** (2001) 013015; R. V. Harlander and W. B. Kilgore, Phys. Rev. Lett. **88** (2002) 201801; C. Anastasiou and K. Melnikov, Nucl. Phys. B **646** (2002) 220; V. Ravindran, J. Smith, and W. L. van Neerven, Nucl. Phys. B **665** (2003) 325; S. Catani, D. de Florian, M. Grazzini, and P. Nason, JHEP **07** (2003) 028; J. Blümlein and V. Ravindran, Nucl. Phys. B **716** (2005) 128; S. Marzani, R. D. Ball, V. Del Duca, S. Forte, and A. Vicini, Nucl. Phys. B **800** (2008) 127; R. V. Harlander and K. J. Ozeren, Phys. Lett. B **679** (2009) 467; A. Pak, M. Rogal, and M. Steinhauser, Phys. Lett. B **679** (2009) 473; C. Anastasiou, R. Boughezal, and F. Petriello, JHEP **04** (2009) 003; R. V. Harlander and K. J. Ozeren, JHEP **11** (2009) 088; R. V. Harlander, H. Mantler, S. Marzani, and K. J. Ozeren, Eur. Phys. J. C **66** (2010) 359; A. Pak, M. Rogal, and M. Steinhauser, JHEP **02** (2010) 025.

[88] D. de Florian and M. Grazzini, Phys. Lett. B **674** (2009) 291.

[89] LHC Higgs Cross Section Working Group, SM Higgs production cross section in gluon fusion at 8 TeV based on [88], 2012 update, used until summer 2013: https://twiki.cern.ch/twiki/bin/view/LHCPhysics/CERNYellowReportPageAt8TeV2012update. For a slightly updated version including the charm quark in the loop see https://twiki.cern.ch/twiki/bin/view/LHCPhysics/CERNYellowReportPageAt8TeV and [53].

[90] S. Actis, G. Passarino, C. Sturm and S. Uccirati, Phys. Lett. B **670** (2008) 12.

[91] T. Inami, T. Kubota and Y. Okada, Z. Phys. C **18**, 69 (1983); A. Djouadi, M. Spira and P. M. Zerwas, Phys. Lett. B **264**, 440 (1991); M. Spira, A. Djouadi, D. Graudenz and P. M. Zerwas, Nucl. Phys. B **453**, 17 (1995).

[92] K. Nakamura et al. (Particle Data Group), J. Phys. G **37**, 075021 (2010).

[93] J. Pumplin, D. R. Stump, J. Huston, H. L. Lai, P. M. Nadolsky, W. K. Tung, JHEP **0207** (2002) 012.

[94] H. -L. Lai, M. Guzzi, J. Huston, Z. Li, P. M. Nadolsky, J. Pumplin, C. -P. Yuan, Phys. Rev. D **82** (2010) 074024.

[95] M. H. Seymour, Nucl. Phys. B **513** (1998) 269.

[96] S. Frixione, Phys. Lett. B **429** (1998) 369.

[97] A. Heister, O. Kodolova, V. Konoplyanikov, S. Petrushanko, J. Rohlf, C. Tully, A. Ulyanov, CERN-CMS-NOTE-2006-036.

[98] M. Dittmar and H. K. Dreiner, Phys. Rev. D **55** (1997) 167.

[99] C. Englert, B. Jager, M. Worek and D. Zeppenfeld, Phys. Rev. D **80** (2009) 035027.

[100] J. C. Collins and D. E. Soper, Phys. Rev. D **16** (1977) 2219.

[101] S. Chatrchyan *et al.* [CMS Collaboration], Phys. Lett. B **726** (2013) 587.

[102] ATLAS Collaboration, ATLAS-CONF-2013-009.

[103] N. Cabibbo and A. Maksymowicz, Phys. Rev. **137**, B438 (1965) [Erratum-ibid. **168**, 1926 (1968)]; J. R. Dell'Aquila and C. A. Nelson, Phys. Rev. D **33**, 80 (1986); J. R. Dell'Aquila and C. A. Nelson, Phys. Rev. D **33**, 93 (1986); C. A. Nelson, Phys. Rev. D **37**, 1220 (1988).

[104] B. W. Lee, C. Quigg, H. B. Thacker, Phys. Rev. D **16** (1977) 1519;
B. W. Lee, C. Quigg, H. B. Thacker, Phys. Rev. Lett. **38** (1977) 883.

[105] P. Langacker, Rev. Mod. Phys. **81** (2009) 1199 [arXiv:0801.1345 [hep-ph]].

[106] J. L. Hewett and T. G. Rizzo, Phys. Rept. **183** (1989) 193.

[107] E. Witten, hep-ph/0201018.

[108] F. Schissler, "Signaturen für Modelle mit Kaluza-Klein-artigen Vektorresonanzen am LHC", Diploma thesis (http://www.itp.kit.edu/diplomatheses.de.shtml).

[109] R. S. Chivukula, D. A. Dicus and H. -J. He, Phys. Lett. B **525** (2002) 175; R. S. Chivukula and H. -J. He, Phys. Lett. B **532** (2002) 121; Y. Abe, N. Haba, Y. Higashide, K. Kobayashi and M. Matsunaga, Prog. Theor. Phys. **109** (2003) 831; R. Foadi, S. Gopalakrishna and C. Schmidt, JHEP **0403** (2004) 042; C. Csaki, C. Grojean, L. Pilo and J. Terning, Phys. Rev. Lett. **92** (2004) 101802; H. -J. He, Int. J. Mod. Phys. A **20** (2005) 3362; E. H. Simmons, R. S. Chivukula, H. J. He, M. Kurachi and M. Tanabashi, AIP Conf. Proc. **857**, 34 (2006); G. Cacciapaglia, C. Csaki, G. Marandella and J. Terning, Phys. Rev. D **75** (2007) 015003.

[110] G. Aad *et al.* [ATLAS Collaboration], Eur. Phys. J. C **72** (2012) 2241; S. Chatrchyan *et al.* [CMS Collaboration], Phys. Rev. D **87** (2013) 072005; CMS Collaboration, CMS PAS EXO-12-060.

[111] S. Chatrchyan *et al.* [CMS Collaboration], Phys. Lett. B **718** (2013) 1229; ATLAS Collaboration, ATLAS-CONF-2013-050.

[112] G. Aad *et al.* [ATLAS Collaboration], JHEP **1301** (2013) 029; S. Chatrchyan *et al.* [CMS Collaboration], arXiv:1302.4794 [hep-ex]; CMS Collaboration, CMS PAS EXO-12-059.

[113] G. Aad *et al.* [ATLAS Collaboration], JHEP **1211** (2012) 138; ATLAS Collaboration, ATLAS-CONF-2013-017; S. Chatrchyan *et al.* [CMS Collaboration], Phys. Lett. B **720** (2013) 63; CMS Collaboration, CMS PAS EXO-12-061.

[114] G. Aad *et al.* [ATLAS Collaboration], Phys. Lett. B **719** (2013) 242; ATLAS Collaboration, ATLAS-CONF-2013-066; S. Chatrchyan *et al.* [CMS Collaboration], Phys. Lett. B **716** (2012) 82.

[115] G. Aad *et al.* [ATLAS Collaboration], JHEP **1301** (2013) 116.

[116] CMS Collaboration, CMS PAS EXO-12-023.

[117] E. Accomando, D. Becciolini, L. Fedeli, D. Dominici and S. De Curtis, Phys. Rev. D **83**, 115021 (2011).

[118] R. S. Chivukula, B. Coleppa, S. Di Chiara, E. H. Simmons, H. J. He, M. Kurachi and M. Tanabashi, Phys. Rev. D **74**, 075011 (2006).

[119] A. S. Belyaev, R. Sekhar Chivukula, N. D. Christensen, H. J. He, M. Kurachi, E. H. Simmons and M. Tanabashi, Phys. Rev. D **80**, 055022 (2009).

[120] K. Hagiwara, R. D. Peccei, D. Zeppenfeld and K. Hikasa, Nucl. Phys. B **282**, 253 (1987).

[121] J. Alcaraz *et al.* [The LEP Collaborations], arXiv:hep-ex/0612034.

[122] M. E. Peskin and T. Takeuchi, Phys. Rev. D **46**, 381 (1992).

[123] R. S. Chivukula, E. H. Simmons, H. J. He, M. Kurachi and M. Tanabashi, Phys. Rev. D **71**, 115001 (2005).

[124] T. Abe, S. Matsuzaki and M. Tanabashi, Phys. Rev. D **78**, 055020 (2008).

[125] R. Casalbuoni, S. De Curtis, D. Dolce and D. Dominici, Phys. Rev. D **71**, 075015 (2005).

[126] A. Birkedal, K. Matchev and M. Perelstein, Phys. Rev. Lett. **94**, 191803 (2005).

[127] R. S. Chivukula, H. J. He, M. Kurachi, E. H. Simmons and M. Tanabashi, Phys. Rev. D **78**, 095003 (2008).

[128] M. Jacob and G. C. Wick, Annals Phys. **7**, 404 (1959) [Annals Phys. **281**, 774 (2000)].

[129] C. Englert, "Spin 1 Resonances in Vector Boson Fusion in Warped Higgsless Models", Diploma thesis (http://www.itp.kit.edu/diplomatheses.de.shtml).

[130] K.S. Koelbig, Cernlib program D103, adapted for HadCalc by M. Rauch.

[131] See e.g. H. Spiesberger, M. Spira and P. M. Zerwas, In *Pike, R. (ed.) et al.: Scattering, vol. 2* 1505 [arXiv:hep-ph/0011255].

[132] S. De Curtis, D. Dominici and J. R. Pelaez, Phys. Rev. D **67**, 076010 (2003).

[133] E. Anderson et. al., Proceedings of the 1990 ACM/IEEE conference on Supercomputing.

[134] A. Lahiri and D. Mukhopadhyay, arXiv:1107.1501 [hep-ph].

[135] J. M. Cornwall, D. N. Levin and G. Tiktopoulos, Phys. Rev. Lett. **30** (1973) 1268 [Erratum-ibid. **31** (1973) 572].

Acknowledgments

First of all, I want to thank Prof. Dr. Dieter Zeppenfeld for supervising this work, for useful advice and discussion and for having accepted me as an external diploma student few years ago, which opened the way towards research in the field of elementary particle physics for me.

I thank Prof. Dr. Margarete Mühlleitner for agreeing to be the second referee of this thesis.

My dissertation was supported financially by the Landesgraduiertenförderung of Baden-Württemberg, which I appreciate very much.

During my studies in Karlsruhe, I have enjoyed the friendly atmosphere, for which I want to thank the members of the institutes ITP and TTP.

Special thanks goes to Michael Rauch and Franziska Schissler for fruitful collaboration and to Franziska Schissler and Tobias Kasprzik for carefully reading parts of the manuscript.

Moreover, I am deeply grateful to Tobias Kasprzik for sharing his live with me, for his love and personal support, but also for many inspiring discussions about physics.

Finally, I want to thank my parents for their enduring love and support.